MAX PLANCK INSTITUTE
FOR DYNAMICS OF COMPLEX
TECHNICAL SYSTEMS
MAGDEBURG

Catalyst and Solvent Selection for Complex Homogeneous Metal-Catalyzed Reactions

Dissertation

zur Erlangung des akademischen Grades

Doktoringenieur
Dr.-Ing.

von M.Sc. Froze Jameel
geb. am 06. August 1989 in Sialkot

genehmigt durch die Fakultät für Verfahrens- und Systemtechnik der
Otto-von-Guericke-Universität Magdeburg

Promotionskommission: Hon. Prof. Dr. Matthias Stein (Gutachter)
Prof. Dr. rer. nat. Dieter Vogt (Gutachter)
Prof. Dr.-Ing. habil. Christof Hamel (Gutachter)
apl. Prof. Dr. rer. nat. Heike Lorenz (Vorsitz)

Eingereicht am: 06. Oktober 2023

Promotionskolloquium am: 23. Januar 2024

Declaration

I hereby declare that I prepared the work submitted without inadmissible assistance and without the use of any aids others than those indicated. Fact or ideas taken from other sources, either directly or indirectly have been marked as such. Further I have not made payments to third parties either directly or indirectly for any work connected with the contents of the submitted thesis. All sources of information are clearly marked, including my own publications.

In particular, I have not consciously:

- Fabricated data or rejected undesired results
- Misused statistical methods with the aim of drawing other conclusions than those warranted by the available data
- Plagiarized data or publications
- Presented the results of other researchers in a distorted way

I do know that violations of copyright may lead to injunction and damage claims of the author and also to prosecution by the law enforcement authorities.

I hereby agree that the thesis may need to be reviewed with an electronic data processing for plagiarism.

The work has not so far submitted either in Germany or abroad in same or similar form and has also not yet been published as a whole.

Magdeburg, October 6, 2023

Froze Jameel

Abstract

In response to the increasing concerns about climate change, there is a need for transition from petrochemicals to renewable, sustainable feedstocks. However, this transition requires careful evaluation of kinetic and thermodynamic data, reaction mechanisms, the development of efficient catalysts and environmentally friendly solvents. This study focuses on investigating the reaction mechanisms of rhodium-catalyzed hydroformylation, reductive amination, and hydroaminomethylation using renewable substrates. The effect of the catalyst and the influence of the solvent on the reaction performance are particularly emphasized.

Solvents play various roles in chemical processes, either by directly participating in the reaction or by affecting the solubility of the reaction species. They have a significant impact on the rate and selectivity of chemical reactions in homogeneous reaction media. Understanding the molecular-level interactions between catalysts, solvents, and substrates is crucial in finding catalysts and solvents that increase reaction rates. Quantum chemical methods, such as density functional theory, are used to calculate these interactions along a reaction pathway.

In hydroformylation, the activation of the catalyst by CO dissociation is independent of the solvent composition. The rate and selectivity of the desired linear reaction are determined early in the catalytic cycle. The difference in activation energies for the formation of C-H bonds as a result of a migratory hydride insertion leads to a selectivity of 98:2 between linear and branched aldehydes. Impurities in the form of hydroperoxides can deactivate the catalyst. The influence of the solvent composition on the rate-limiting transition state is minimal. An optimal solvent for hydroformylation can be selected based on the solubility of the catalyst in the solvent. A kinetic model that considers impurities was proposed in collaboration with the group of Prof. Christof Hamel (Martin Gerlach, Otto von Guericke University (OVGU) Magdeburg) to model the kinetics of hydroformylation.

During reductive amination, solvent molecules that donate hydrogen bonds promote enamine formation. The catalyst containing a bidentate phosphine ligand coordinated to the rhodium metal controls the selectivity of the reaction through ligand-substrate interactions. A solvent screening workflow was developed in collaboration with the groups of Prof. Gabriele Sadowski (Fabian Huxoll, TU Dortmund) and Prof. Dieter Vogt (Jonas Bianga, TU Dortmund) to find suitable solvents for high reaction rates. In collaboration with the group of Prof. Christof Hamel (Sabine

Kirschtowski, OVGU Magdeburg) a kinetic model combining quantum chemical calculations and kinetic experiments for rhodium-catalyzed reductive amination was then developed.

For hydroaminomethylation, a water-tolerant catalysts is required to ensure high product yield and minimal loss of catalyst due to phase separation. The choice of catalyst and the composition of the synthesis gas have a significant impact on the kinetics of the reaction.

The methods and tools developed in this study can be used to derive kinetic models for homogeneously catalyzed multiphase reactions, considering the effects of catalyst, and solvent. The computational solvent screening workflow enables the selection of environmentally friendly solvents as substitutes for harmful industrial solvents. Overall, this research contributes to the development and selection of efficient catalysts and green solvents in the transition from petrochemicals to sustainable feedstocks.

Kurzfassung

Angesichts der wachsenden Besorgnis über den Klimawandel, besteht die Notwendigkeit, von petrochemischen auf erneuerbare und nachhaltige Rohstoffe umzusteigen. Dieser Übergang erfordert jedoch eine sorgfältige Analyse der kinetischen und thermodynamischen Daten, der Reaktionsmechanismen sowie die Entwicklung effizienter Katalysatoren und umweltfreundlicher Lösungsmittel. Diese Studie konzentriert sich auf die Untersuchung der Reaktionsmechanismen der rhodiumkatalysierten Hydroformylierung, reduktiven Aminierung und Hydroaminomethylierung unter Verwendung nachwachsender Substrate. Der Effekt des Katalysators und der Einfluss des Lösungsmittels auf die Reaktionsleistung werden besonders hervorgehoben.

Lösungsmittel spielen in chemischen Prozessen verschiedene Rollen, indem sie entweder direkt an der Reaktion teilnehmen oder die Löslichkeit der Reaktionsspezies beeinflussen. Sie haben einen erheblichen Einfluss auf die Geschwindigkeit und Selektivität chemischer Reaktionen in homogenen Reaktionsmedien. Das Verständnis der Wechselwirkungen auf molekularer Ebene zwischen Katalysatoren, Lösungsmitteln und Substraten ist entscheidend für die Suche nach Katalysatoren und Lösungsmitteln, die die Reaktionsgeschwindigkeit erhöhen. Quantenchemische Methoden wie die Dichtefunktionaltheorie werden eingesetzt, um diese Wechselwirkungen entlang eines Reaktionsweges zu berechnen.

Bei der Hydroformylierung ist die Aktivierung des Katalysators durch die Dissoziation von CO unabhängig von der Zusammensetzung des Lösungsmittels. Die Geschwindigkeit und Selektivität der Reaktion zum gewünschten linearen Aldehyd wird früh im katalytischen Zyklus bestimmt. Der Unterschied in den Aktivierungsenergien für die Bildung von C-H-Bindungen als Folge einer migratorische Hydridinsertion führt zu einer Selektivität von 98:2 zwischen linearen und verzweigten Aldehyden. Der Einfluss der Lösungsmittelzusammensetzung auf den geschwindigkeitsbestimmenden Schritt ist minimal. Verunreinigungen in Form von Hydroperoxiden können den Katalysator deaktivieren. In Zusammenarbeit mit der Gruppe von Prof. Christof Hamel (Martin Gerlach, OVGU Magdeburg) wurde ein kinetisches Modell vorgeschlagen, das Verunreinigungen berücksichtigt, um die Kinetik der Hydroformylierung zu modellieren.

Bei der reduktiven Aminierung fördern protische Lösungsmittel, die Enaminbildung. Ein zweizähniger Phosphinkatalysator steuert die Selektivität der Reaktion durch Ligand-Substrat-Wechselwirkungen. In Zusammenarbeit mit den Gruppen von Prof. Gabriele Sadowski (Fabian Huxoll, TU Dortmund) und Prof. Dieter Vogt (Jonas Bianga, TU Dortmund) wurde ein Lösungsmittel-Screening entwickelt, um geeignete Lösungsmittel für hohe Reaktionsgeschwindigkeiten zu finden. In

Zusammenarbeit mit der Gruppe von Prof. Christof Hamel (Sabine Kirschtowski, OVGU Magdeburg) wurde ein kinetisches Modell entwickelt, das quantenchemische Berechnungen und kinetische Experimente für die rhodiumkatalysierte reduktive Aminierung kombiniert.

Für die Hydroaminomethylierung wird ein wassertoleranter Katalysator benötigt, um eine hohe Produktausbeute und einen minimalen Katalysatorverlust durch Phasentrennung zu gewährleisten. Die Wahl des Katalysators und die Zusammensetzung des Synthesegases haben einen großen Einfluss auf die Reaktionskinetik.

Die in dieser Studie entwickelten Methoden und Werkzeuge können zur Entwicklung kinetischer Modelle für homogen katalysierte Reaktionen unter Berücksichtigung der Auswirkungen von Katalysator und Lösungsmittel verwendet werden. Der Arbeitsablauf des computergestützten Lösungsmittel-Screenings ermöglicht die Auswahl umweltfreundlicher Lösungsmittel als Ersatz für schädliche industrielle Lösungsmittel. Insgesamt trägt diese Forschung zur Entwicklung und Auswahl effizienter Katalysatoren und umweltfreundlicher Lösungsmittel für den Übergang von der Petrochemie zur Chemie nachhaltiger Rohstoffen bei.

Declaration of Collaborative Research

This doctoral thesis was embedded in a large interdisciplinary DFG project Transregio 63 (SFB/TR63) “Integrated Chemical Processes in Liquid Multiphase Systems”. The kinetic model development and kinetic experiments were performed at the Institute of Process Engineering, Otto von Guericke University (OVGU) Magdeburg, in collaboration with the group of Prof. Andreas Seidel-Morgenstern and Prof. Christof Hamel. The kinetic experiments for hydroformylation of 1-decene were performed by Martin Gerlach. The kinetic experiments for reductive amination and hydroaminomethylation were carried out by Sabine Kirschtowski and Wieland Kortuz. The kinetic model for the reductive amination of 1-undecanal was developed in collaboration with Sabine Kirschtowski. The degradation of hydroformylation catalyst was investigated in a joint work with Martin Gerlach at the same group.

Activity coefficients of the reaction substrates were estimated by Fabian Huxoll in the group of Prof. Gabriele Sadowski (Chair of Thermodynamics, Technical University of Dortmund (TUD)) using PC-SAFT (Perturbed Chain Statistical Associating Fluid Theory) method and is not the work of the author of this thesis.

Reductive amination batch experiments in different solvents were carried out by Jonas Bianga and Thomas Seidensticker in the group of Prof. Dieter Vogt (Chair of Technical Chemistry, Technical University of Dortmund (TUD)).

The results obtained by the above-mentioned cooperation partners has been indicated at the relevant places in this doctoral thesis.

Glossary

Abbreviations

10-UME	methyl 10-undecenoate
acac	acetylacetone
AM1	Austin Model 1
BSIE	basis set incompleteness error
BSSE	basis set superposition error
BP86	Becke exchange functional and the Perdew correlation density functional
BYLP	Becke, Lee-Yang-Parr exchange-correlation hybrid density functional
B3LYP	Becke, 3-parameter, Lee-Yang-Parr exchange-correlation density functional
BPP	BiPhePhos (6,6′-[(3,3′-Di-tert-butyl-5,5′-dimethoxy-[1,1′-biphenyl]-2,2′-diyl)bis(oxy)]bis(6H-dibenzo[d,f][1,3,2]dioxaphosphepine))
CO	carbonyl
CO_2	carbon-dioxide
COSMO	conductor like solvent screening mode
COSMO-RS	conductor like solvent screening mode for real solvents
COD	1,5-cyclooctadiene
CC	coupled cluster method
DMF	dimethylformamide
DMA	dimethyamine
DEA	diethylamine
def2-TZVP	valence triple-zeta polarization basis set
DFT	density functional theory
DTBPMB	1,2-bis(di-tert-butylphosphino-methyl)benzene
DME	dimethyl dodecanedioate ester
enamine	(E)-N,N-diethylundec-1-en-1-amine
FTIR	Fourier-Transform infrared spectroscopy
FCI	full configuration interaction method
GFN-xTB	geometry, frequency, non-covalent, extended tight binding method
GGA	generalized gradient approximation
HF	Hartree-Fock
HSE	health, safety, environment

Iphos	2,2′-bisbis[3,5-bis(trifluoromethyl)phenyl]-phosphanylmethyl-1,1′-binaphthyl
IR	infrared spectroscopy
l:b	linear:branched
LDA	local Density Approximation
LSDA	local spin-density approximation
MSA	methanesulfonic acid
MeOH	methanol
MP	Møller-Plesset perturbation method
ML	machine learning
Naphos	2,2′-bis(diphenylphosphinomethyl)-l,l′-binaphthyl
NMR	nuclear magnetic resonance spectroscopy
PCM	polarizable continuum model
PES	potential energy surface
PPh_3	Triphenylphosphine)
PBE0	Perdew, Burke and Enzerhof exchange density functional
PC-SAFT	Perturbed-Chain Statistical Associating Fluid Theory
QM/MM	quantum mechanics/molecular dynamics
QM	quantum mechanics
r^2SCAN	strongly constrained and appropriately normed composite density functional
RDS	rate determining step
SE	semi-empirical
SDGs	sustainable development goals
SFB	Sonderforschungsbereich (Collaborative Research Centre)
SASA	solvent-accessible surface area
syngas	synthesis gas
SX	SulfoXantPhos (4,5-Bis(diphenylphosphino)-9,9-dimethyl-2,7-disulfoxanthene disodium salt; 4,5-Bis(diphenylphosphino)-9,9-dimethylxanthene-2,7-disulfonic acid disodium)
TMS	thermomorphic solvent system
TST	transition-state theory
TPSS	Tao-Perdew-Staroverov-Scuseria meta GGA density functional
TPPTS	trisodium salt of 3,3′,3′′phosphinidyne tris(benzenesulfonic acid
TBPP	(tris(2-t-butylphenyl)phosphite)
tBuOOH	tert-Butyl hydroperoxide
THF	tetrahydrofuran
TPP	tetraphenylporphyrin
TPPTS	3,3′,3′′-Phosphanetriyltris(benzenesulfonic acid) trisodium salt

UV/Vis	ultraviolet/visual spectroscopy
UNIFAC	universal quasichemical functional-group activity coefficient
vdW	van der Waals
Xyliphos	2-(Diphenylphosphino)ferrocenyl]ethyldi-3,5-xylylphosphine
XantPhos	(9,9-Dimethyl-9H-xanthene-4,5-diyl)bis(diphenylphosphane)

Latin Letters

a_i	thermodynamic activity of component *i*	-
c_p	heat capacity	J/K
E_A	activation energy	J/mol
E	electronic energy	J/mol
E_{tot}	total electronic energy	J/mol
$\tilde{E}_{XC}$	exchange-correlation energy	J/mol
$\bar{f}$	cutoff parameter	
G	Gibbs free energy	J/mol
$-\Delta\Delta G^{\ddagger}$	Reduction in the Gibbs energy of the transition state at infinite dilution in the solvent relative to those in the gas phase in the absence of any solvent	J/mol
H	Hessian matrix	-
$\hat{H}$	Hamiltonian operator	-
k	rate constant	s^{-1}
Mt	million tons	kg
N	total number of electrons in a molecular system	-
P	pressure	bar, atm
Q	partition function	-
S	catalytic selectivity	%
S	entropy	J/K
$\hat{T}$	kinetic energy operator	J/mol
T	temperature	K, $^{\circ}C$
TOF	Turnover frequency	h^{-1}
$\hat{U}$	electron-electron interaction energy operator	J/mol
$\hat{V}$	potential energy operator	J/mol
$\hat{V}_{ext.}$	external potential	-
β_n	natural bite angle	$^{\circ}$
χ	Tolmans′ electronic parameter	-
Ψ	wavefunction	-
ρ	electron density	$e/Å^{-3}$
η	viscosity	Ns/m^2

σ	charge density	e/Å^2

Indices, sub- and superscripts

c	correlation
elec	electronic
gas	gas phase
nuc	nuclear
r	reaction
solv	solvation
solu	solution
tot	total
x	exchange

Mathematic symbols and operators

$\Delta(\cdot)$	relative change
$\nabla(\cdot)$	gradient
$\hat{\cdot}$	operator

Constants

R	gas constant	8.3145 J/mol K
k_B	Boltzmann's constant	1.3806x10^{-23} J/K
h	Planck's constant	6.6261x10^{-34} J s
ϵ	dielectric constant	-

Contents

1 Introduction

Today's global chemical industry is highly dependent on non-renewable fossil fuels with oil being the most important feedstock. The scenario of depleting oil reserves and global conflicts therefore threatens the basis of chemical industry and has a potentially huge impact on our day-to-day life. Chemical industry consumes 14% of globally produced crude oil and 8% of natural gas. As a result, it is responsible for over 1.5 Gigatons of CO_2 emissions, making it the third-largest contributor to global carbon emissions [1], thereby, posing significant existential challenges for humanity, such as climate change. To circumvent this environmental calamity, in 2015, United Nations (UN) adopted 17 sustainable development goals (SDGs) (Figure 1.1). In the same year, the Paris Agreement was signed by all 196 member states to reduce the green house emissions.

Fig. 1.1.: Sustainable development goals (SDGs) adopted by United Nations member states in 2015 to build strategies that improve health, education, reduce inequality, and spur economic growth [2].

Among the 17 SDGs, Goal 9, “Industry, innovation and infrastructure”, Goal 12, “Responsible consumption and production” and Goal 13, “Climate action”, directly address the chemical industry to implement the usage of sustainable raw materials from renewable resources rather than fossil fuels to produce sustainable chemicals with minimal waste and reduce their release in air, water and soil in order to minimize adverse effects on human health and the environment [2].

To reduce the carbon footprint, climate protection law passed by the German parliament on June 24, 2021, calls for climate neutral Germany by 2045 [3]. Climate neutrality, here, means greenhouse gases emitted from fossil fuel consumption should be absorbed again by nature.

To achieve these sustainable development goals (SDGs), the famous “12 principles of green chemistry” proposed by Paul Anastas and John Warner in 1998 are a key factor, as they provide a framework for designing sustainable chemical processes and products using renewable substrates (Figure 1.2) [4].

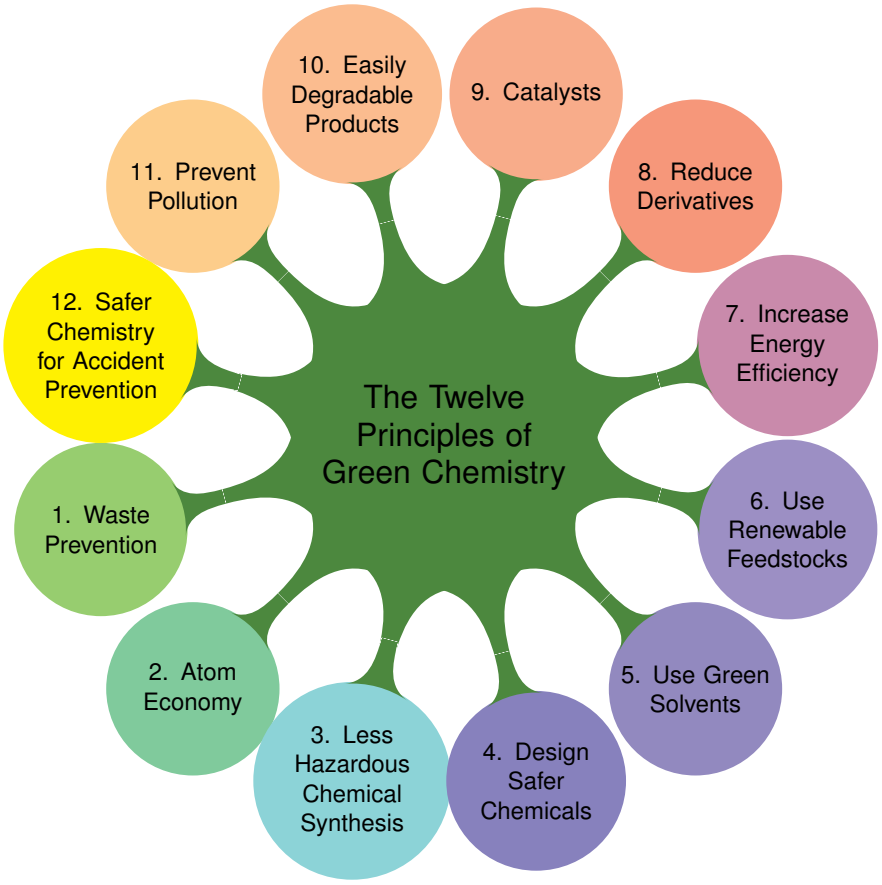

Fig. 1.2.: Twelve principles of green chemistry proposed by Anastas and Warner. Adopted from [4].

The principles of green chemistry call for minimization of waste generated as a result of chemical production processes and promote the usage of renewable feedstock. The chemical production processes must be atomic and energy efficient and thereby have low production costs and carbon footprint. They should be designed to minimize the generation of byproducts. Catalysts and green solvents (environment friendly) should be used to enhance the productivity and yield of the production process. The catalyst should be easily recoverable after each production cycle so that it does not contaminate the product and the environment. Unnecessary side processes must be avoided, and the products should be easily degradable at the end of their functional life and not remain in the ecosystem for a long period of time. The substrates and generated products should not be toxic, and production processes should be safe thus preventing potential chemical accidents.

These are the main driving factors for the development of more sustainable chemical processes and the replacement of fossil fuels with renewable feedstocks in chemical industry. Medium to long chain (C_6 to C_{20}) oils and fats originating from plants and animals are currently the most important renewable feedstock for the chemical industry. In 2018, 2.6 million metric tons (Mt) of these renewable feedstocks were used by the chemical industry in Germany [5]. These renewable oils can be used as starting material for different chemical reactions such as olefin carbonylation and amination. Thus, to optimize the functionalization of long chain unsaturated oleo-compounds in homogeneously catalyzed systems, the *Sonderforschungsbereich Transregio 63* (SFB TR-63), a joint research effort between the universities TU Berlin, TU Dortmund, and OVGU Magdeburg was initialized in 2010. The overall objectives of this project were the design and optimization of catalyst systems to achieve high activity, selectivity by using renewable feedstocks instead of fossil fuels and post-reaction catalyst recovery. Complex multistep noble metal catalytic systems such as hydroformylation, reductive amination, hydroaminomethylation and hydroesterification were investigated from a molecular level (kinetic modeling, inter-molecular solvent effects) to a mini-plant level using oleo-chemicals as renewable feedstock.

Due to the importance of reaction kinetics for reactor design and optimization, the first step in chemical process development is detailed insight into reaction mechanism. By knowing the mechanism, we can optimize the process conditions to reduce waste (principle **1**), minimize energy consumption (principle **7**), design suitable catalysts (principle **9**), find optimal solvents (principle **5**) and improve products yields. From the reaction mechanism, the Gibbs energy required to generate all the intermediates and products is then calculated that allows the estimations of

the kinetic rate and thermodynamic constants associated to all elementary reaction steps.

Once the energetic profile of the reaction is known, it provides an insight into the rate and selectivity limiting steps. With this knowledge, reaction rates and yields are calculated. Along the reaction pathway several valuable intermediates are formed that can be detected experimentally by using: ultraviolet (UV/Vis) and infrared (IR) spectroscopy, cyclic voltammetry and nuclear magnetic resonance (NMR) spectroscopy [6, 7]. Hence, by understanding the most relevant features of a given reaction, new strategies to achieve high rates, yields and/or selectivities can be developed.

The main drawback for the experimental methods (spectroscopic and electrochemical) for mechanistic elucidations is the short life-span of the intermediates and transition states formed during the reaction. As a consequence, those intermediates are difficult or, in some cases, impossible to detect. Computational methods, in combination with the experiments, can provide a theoretical framework for understanding a reaction mechanism [8]. Computational methods are also used to predict the properties of intermediates and transition states such as enthalpy, entropy and free energy of solvation that may be difficult to estimate experimentally. The goal of the mechanism resolution is to find possible intermediates and transition states that convert the reactants into the products. The activation energies of these transition states can later be used to develop rate equations that describe the kinetic behavior of the chemical system i.e. kinetic models. For complex multistep reaction, it can be very complicated, or sometimes even impossible, to estimate the kinetic rate constants by mechanistic rate approaches such as Christiansen's method [9], due to the large number of elementary reactions involved. In practice, reduced kinetic models are generated by simplification of reaction mechanisms, which results in kinetic parameter estimation. The design of reduced kinetic models and simplification of reaction mechanisms is beyond the scope of this work and discussed in detail elsewhere [10, 11]. A possible alternative approach to predicted kinetic behavior of multistep chemical reaction is to use computational methods such as Density Functional Theory (DFT). Once the reaction pathway is resolved, the change in Gibbs free energy along the reaction cycle (PES, see Section 3.2) is obtained. The kinetic rate constants are calculated from activation energies of transition states along the reaction cycle which then can be used in combination with the experiments to generate kinetic models for complex chemical cycles [12, 13].

A catalyst plays a significant role in controlling the rate of a chemical reaction. Catalysts are applied in more than 85% of all chemical processes [14]. A reaction

can be catalyzed either in a homogeneous or a heterogeneous manner. Especially, in view of sustainable process development, homogeneously catalyzed systems provide some pivotal advantages compared to its heterogeneous counterpart such as high selectivity towards the desired products and milder reaction conditions. This helps to safe energy as well to prevent waste production. Finally, in a homogeneously catalyzed reaction system, a solvent being present in the largest amount (in terms of volume) has a significant effect on the reaction rate and productivity. Chipperfield summarized four major applications of solvents in the chemical process, i.e., as reactant, reaction media, separation agent and transportation agent [15]. Therefore, an understanding of physical solvent properties such as solvent polarity and its hydrogen-bond donating/accepting abilities can play a significant role in catalyst design. Exchanging the conventional industrial solvent with environment friendly substitutes will be another monumental step towards the development of sustainable chemical production processes. In addition, post-reaction recovery of valuable catalyst in homogeneously catalyzed reactions, is beneficial from both an economic and an ecological prospective. Thereby, it must be considered during the process design and/or optimization. Since in homogeneous reactions, substrate, product and catalyst are dissolved in the solvent, they can only be separated from each other with a certain amount of effort when the reaction is completed. Distillation/rectification can be a possible separation process. However, due to the high thermal costs and possible catalyst degradation, it can significantly increase the operating costs of large-scale industrial applications. Temperature controlled multiphase separation systems such as thermomorphic solvent system (TMS) is another possible catalyst recovery/recycling approach where, the product and catalyst are separated in two different liquid phases. The product either separates spontaneously from the catalyst-rich phase during the reaction through a favorable solvent selection or through another solvent added into the mixture, which leads to the phase separation [7]. The choice of an optimal catalyst and solvent does not only accelerate the reaction but can also assist easy catalyst recovery once the reaction is completed. Advances in computational chemistry have certainly found its application in catalyst and solvent design/selection, thereby resulting in catalysts ensuring high activity and selectivity in solutions [16–19]. Computer-aided solvent selection using quantum chemical methods is a valuable tool to minimize the experimental effort, and shorten the process development time.

1.1 Computer-Aided Catalyst and Solvent Selection

An optimal catalyst for a homogeneously catalyzed reaction mixture should be: readily available in the catalyst mixture, highly active, selective towards the desired products and easily recoverable after the reaction. Industrial catalyst design, in the past, is usually based on the pre-existing expert knowledge or by screening via trial and error [20]. However, the design of new catalysts supported by quantum chemical calculations of reaction mechanisms and kinetic modeling of corresponding reaction rates is the new standard [21]. In fact, first examples of catalyst design in heterogeneous systems by means of computational screening have recently emerged [22–24]. Catalyst screening for homogeneously catalyzed mixtures is more complicated than heterogeneous systems [20], due to the conformational complexity of large ligands involved. The complexity further increases when solvent effects are additionally taken into account, thus leading to difficulties in determining the active conformational space and corresponding enthalpy and particularly entropy contributions to the free energy [25]. In addition, a balanced description of inter- and intramolecular interactions during solvation is similarly challenging [26].

Computational methods have proven to be a powerful tool to complement traditional experimental molecular catalyst design by providing useful predictions of catalyst performance and reducing the time required for catalyst screening. There are several computational approaches to catalyst design and selection, such as the reaction mechanism-based approach, which uses computational methods to calculate elementary reaction steps and resolve the complete reaction mechanisms. Here, the calculations provide the critical reaction steps, such as the rate-limiting step, and inform which future experiments should be performed based on the quantitative screening of candidate catalysts. The second approach is the descriptor-based approach, where physical or chemical considerations are used to identify catalyst's properties that are directly related to catalyst performance, such as thermodynamic activity. Then based on these properties, a set of candidate catalysts tested to design and select optimal catalysts. Finally, there is the data-driven approach, where predictive models are built using statistical data analysis or machine learning algorithms (ML) to find correlations between available data and catalyst performance. A detailed review of these approaches was recently published by Soyemi and Szilási [16].

Despite the high computational cost, the reaction mechanism-based approach is generally preferred over descriptor-based approaches due to less prediction accuracy of the latter [27] and machine learning approaches due to the lack of reliable training

data [21]. The reaction mechanism-based approach helps to rationalize catalyst performance by elucidating all relevant elementary steps, locating the rate- and selectivity-determining steps, and finally making predictions made by fine-tuning the atomic-level interactions that determine catalyst performance. Comparisons between calculations and experiments can be made based on measurements of reaction rates, spectroscopic features such as IR [28, 29] and NMR [30]. Comparison with experimental measurements increases the reliability of computational predictions and improves the chances of successful catalyst design in the laboratory [31].

Investigating all elementary steps using a reaction mechanism-based approach has several advantages. Calculations and experiments can be directly compared using the free energy of the reaction (thermodynamics) and the activation energies of the transition states (kinetics) leading to the desired product [32]. This approach can also be used to determine the rate-limiting step, calculate the activity and/or selectivity of the catalyst, and obtain structural information and the energetics of all elementary steps. Once the most favorable reaction pathway is identified, kinetic models can be built and compared with experimental results to make predictions for fine-tuning the catalytic reaction under study (e.g., solvent, ligand) [33, 34]. By analyzing the complex reaction networks promoted by different catalysts, new mechanistic insights can be uncovered that may not be predicted by other qualitative, descriptor-based, and data-driven approaches.

In homogeneously catalyzed reactions, the solvent represents the reaction environment and can significantly affect reaction rates, yields, selectivity, and phase behavior of a complex reaction medium [35, 36]. Selecting an optimal solvent to carry out a reaction is critical to reaction performance and a mandatory step in optimizing reaction conditions. When selecting the solvent, it should be ensured that the solvent does not react with the reactants or products, which could lead to the formation of byproducts. In addition, the solvent must be stable under the reaction conditions (it must not decompose), completely separable after the reaction cycle, safe to use, environment friendly and widely available and should not be expensive to ensure the economic viability of the process.

At the macroscopic level, the solvent influences the solubility of the species present along the reaction pathway. At the molecular level, solvent molecules interact directly with substrates, products and catalyst molecules, as well as intermediates and transition states. During solvent selection for homogeneous phase reactions, either these interactions are often not completely taken into account or solvent effects are estimated using simple implicit models, thus hindering the selection of optimal solvents for a reaction [37]. In computational chemistry, there are three

approaches: implicit (continuum), cluster/continuum (hybrid implicit/explicit) and full explicit solvent treatment, to investigate the complex solvent effects in industrial catalysis [38–40]. The theoretical background of those approaches is discussed in detail in the following chapter (See section 3.2.3). In addition, a recent review by Norjmaa et al. provides a comprehensive overview of those approaches [37].

One example of such an approach is Pd(II)-catalyzed hydroesterification (Hyes), where methyl 10-undecenoate (10-UME) obtained from Castor oil was converted into dimethyl dodecanedioate (DME) in methanol:dodecane solution. Methanol as polar hydrogen bond donating solvent plays three different roles in the catalytic process. First, it takes part in the reaction as a reagent to form methoxy esters (DME), second it is required to form the active catalyst species, and third, it coordinates to the Pd(II)-hydride complex by occupying the vacant coordination site [41]. The hydroesterification of 10-UME using a palladium catalyst showed that the nature of the solvent has a pronounced effect on the catalyst activation, post-reaction products separation and catalyst recovery. The inter-molecular catalyst-solvent interactions makes the methanol coordination to the acyl-complex energetically feasible. Methanolysis of the acyl complex is the rate-determining step for Hyes. The excess amount of dissolved CO in the catalyst mixture causes catalyst inhibition [12]. The DFT calculated activation energy of 80 kJ/mol was found to be in a good agreement with the experiment using same catalyst, substrate and solvent system [42].

As per the green chemistry principles, the incorporation of HSE (Health, Safety, Environment) solvent parameters in solvent selection have been discussed for more than a decade [43–45] but not fully addressed [46]. These parameters when combined with the physical solvent properties such as solvent polarity, catalyst-solvent and substrate-solvent interactions can potentially result in optimal solvent selection which further will result in high reaction activity and lesser ecological impact.

1.2 Aim of This Work

This work aims to resolve detailed reaction mechanisms and estimate various effects of solvent on the reaction kinetics and thermodynamics to generate in-depth process knowledge and reduce the experimental effort for the selection of optimal catalysts and solvents. To achieve this goal, this thesis is divided into the following chapters:

For the development of novel sustainable processes or the optimization of previous production processes, the model reactions rhodium-catalyzed hydroformylation, reductive amination and hydroaminomethylation of renewable substrates, chosen for this work as examples, are introduced in chapter 2. Chapter 3 gives a systematic introduction into various computational chemistry methods to solve the electronic Schrödinger equation and describes how critical reaction performance parameters such as reaction kinetics, thermodynamics and solvent effects can be calculated using computational chemistry.

Chapter 4 discusses the solvent effects in hydroformylation of 1-decene where a possible green solvent alternative is needed for toxic DMF (Dimethylformamide) solvent. The reaction occurs in presence of a rhodium catalyst that is activated by ligand dissociation. At first, catalyst activation is investigated based on the strength/weakness of catalyst-ligand interactions. Followed by the complete reaction mechanism elucidation leading to desired linear aldehydes at first, in the absence of solvent. Later, reaction pathways leading to side products are investigated, which allow the resolution of the catalyst's selectivity towards the desired product. Finally, the solvent effects on the complete reaction mechanism are calculated followed by the estimation of the effect of multiple solvent candidates on the rate of the reaction to find a possible alternative for DMF solvent. In addition, the effect on the substrate impurities on the catalyst activity and selectivity are also discussed for the hydroformylation.

Chapter 5 investigates the different roles of solvent that may affect the reaction performance by considering inter-molecular catalyst-solvent and catalyst-substrate interactions. Effect of solvent is resolved during the first half of reductive amination (RA) of 1-undecanal (amination) using a micro-solvation approach. In addition, a computational solvent selection workflow is then introduced to find an optimal solvent for RA. Quantum chemical calculations and a thermodynamic activity model are combined for a fast solvent screening of multiple solvent candidates. Later, the number of solvent candidates are further refined based on explicit catalyst-solvent interactions. Finally, the results are evaluated by batch experiments in selected solvents.

As previously mentioned, catalyst selection is a critical reaction performance parameter which normally is selected based on empirical data acquired as a result of extensive experimental efforts. In chapter 6, the insights obtained in the previous chapters are combined to address the effects of catalyst and reactant gas composition on the kinetics of hydroaminomethylation (HAM) of long chain olefins in solution. At first, the complete reaction pathway for hydroformylation using an

electron with-drawing BiPhePhos (BPP) ligand and an electron-donating bidentate SulfoXantPhos (SX) ligand is compared to resolve the effect of ligands for optimal catalyst selection/design. Later, the effect of syngas composition on the catalytic hydrogenation of enamine generated after the amination is addressed. Quantum chemical calculations enable the estimation of activation energies of rate limiting elementary steps, that can be used for the improvement/simplification of the kinetic model.

The approaches developed in the course of this thesis provide in-depth insights into complex reaction mechanisms. These approaches not only allow the selection and design of novel efficient catalysts to fine-tune the rate and selectivity of a reaction, but also allow green solvent selection to reduce the environmental impact of a chemical process. Finally, chapter 7 gives the overall conclusions and an outlook important for the future work.

2 Complex Homogeneous Transition-Metal-Catalyzed Reactions

Within InPROMPT, long chain unsaturated compounds obtained from renewable raw materials rather than petrochemicals were chosen as substrates. 1-decene and 1-dodecene, two linear olefins with a terminal double bond and two bio-based unsaturated oleo-compounds (methyl 10-undecenoate and methyl oleate) were used as renewable substrate representatives. Formation of C-C, C-O and C-N bonds via hydroformylation (Hyfo), hydroesterification (Hyes), reductive amination (RA) and hydroaminomethylation (HAM) were investigated in homogeneous phase (see below). These newly introduced functional groups into the renewable substrates in the presence of transition metal catalysts resulted in valuable products (aldehydes, esters and amines) with wide industrial applications.

The design and selection of efficient catalysts (transition metal-coordinated with sophisticated ligands) was desired to ensure high catalytic activity, selectivity and, and fast product conversion with the least environmental impact. Homogeneous catalysts due to their tuneable properties by the incorporation of coordinating ligands, are known for high catalytic selectivity compared to heterogeneous catalysts, however, post-reaction catalyst recovery is a common limitation for homogeneously catalyzed reactions. The versatility of homogeneous catalysts is governed by the activity of the central transition metal, molecular architecture and electronic properties of the coordinated ligands. The ligand-modified catalysts show higher activity and selectivity for the desired products due to the modifications of electron density at the metal centers and steric control of the ligand binding [47]. For all the above-mentioned reactions investigated, rhodium was chosen as active transition metal for Hyfo, RA and HAM, and palladium was used for hydroesterification. In the following subchapters, all of these aforementioned reactions are introduced, and different catalyst systems are discussed.

2.1 Hydroformylation

Also known as oxo-reaction, hydroformylation was first discovered by Otto Roelen in 1938 [48]. Hydroformylation is a transition metal-mediated insertion of carbon monoxide (CO) and hydrogen (H_2) to olefins thus generating corresponding aldehydes [49] (See Figure 2.1). With an annual production exceeding over 10 million tons, the resulting aldehydes, then used in a variety of products such as detergents, surfactants, cosmetics, pharmaceutics and polymers, underlining their importance in industrial chemistry [6].

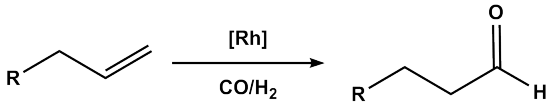

Fig. 2.1.: Rhodium-catalyzed hydroformylation of olefins in the presence of synthesis gas CO/H_2 generating aldehydes.

From its discovery to up until 1970s, cobalt as the transition metal catalyst dominated the hydroformylation production [49–51]. However, harsh conditions (200 °C and 300 atm) were needed to carry out the reaction [52]. Since 1970, rhodium catalysts were introduced showing considerably improved activities. In addition to cobalt and rhodium, other catalysts with transition metals such as platinum [53], ruthenium [54, 55] and iridium [56] have also been reported. Despite the high costs, rhodium-based catalysts are extensively used for hydroformylation of terminal and internal olefins, as they tend to provide high selectivity towards the linear aldehydes. Both cobalt and rhodium-based catalysts are used for hydroformylation in industry today. However, post reaction catalyst recovery, especially with expensive rhodium catalysts is very important in designing a cost-efficient and environment friendly hydroformylation process.

Formation of the branched aldehydes is the most dominant side reaction in hydroformylation. Among linear and branched aldehydes, linear aldehydes are desired due to the better biodegradability of the linear carbon chains [57]. Transition metal catalysts with ligands attached to the metal center have a large influence on the activity and selectivity and thereby can suppress the formation of undesired branched aldehydes. A large variety of mono- and bidentate phosphine [58–60], phsophonites [61, 62] and phosphite [63–66] ligands have been proposed and employed to carry out rhodium-catalyzed hydroformylation.

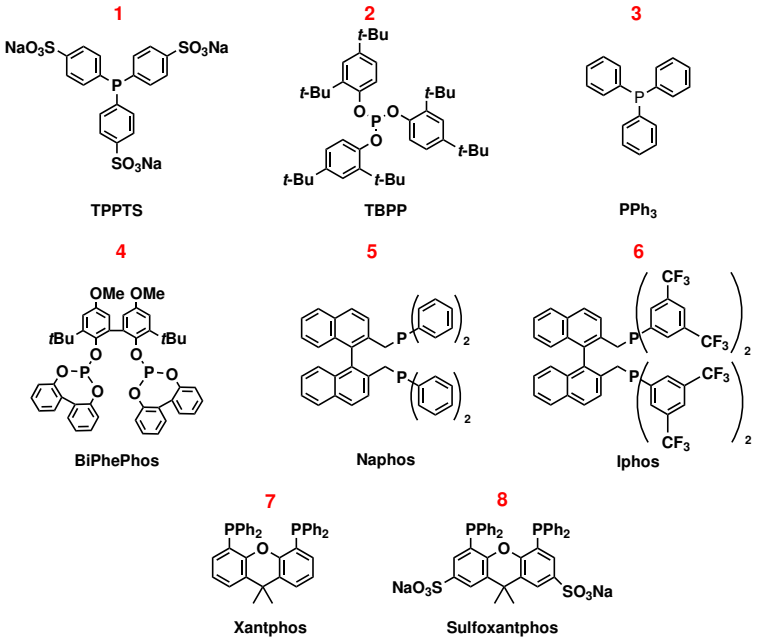

Fig. 2.2.: Bulky mono- (1-3) and bidentate (4-8) ligands for transition metal catalyzed hydroformylation of alkenes. Adapted from [67].

Phosphites have demonstrated superior performance in terms of catalytic selectivity when compared to the phosphine and phosphonite based ligands due to their high π-accepting ability [51]. Monophosphite ligands such as TPPTS (trisodium 3,3′,3″-phosphinidyne tris(benzenesulfonic acid), TBPP (tris(2-t-butylphenyl)phosphite) and PPh_3 (triphenylphosphine) showed high reaction rates for hydroformylation but suffer from low selectivity (Figure 2.2) [68].

For high product selectivity, bidentate ligands are preferred due to their increased steric hindrance around the catalytic metal center. The natural bite angle (β_n), introduced by Casey and Whiteker [69], is the angle between the phosphorous atoms and metal center in the catalytic complex (left; Figure 2.3). The effects of bite angle on the selectivity of oxo reaction were investigated by Ahmed et al. [70], and it has been concluded that larger bite angles results in high selectivity towards the desired linear aldehydes (right; Figure 2.3).

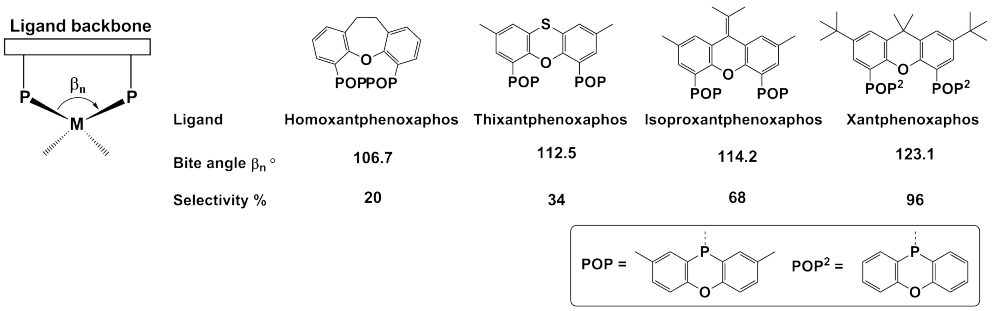

Fig. 2.3.: Illustration of the bite angle in a transition metal complex (left) and its effect on the selectivity of rhodium-catalyzed hydroformylation of alkenes (right). Adapted from [71].

In addition to the steric properties of a ligand, its electronic properties also play an important role in determining the activity and selectivity of the catalytic complex. In general, phosphites are better π-acceptors than phosphines, which is often indicated by the electronic parameter χ, first introduced by Tolman in 1970 [72]. This electronic parameter is determined by measuring the Ni-CO stretch vibration of nickel-carbonyl complexes containing a particular ligand. The tris(*tert*-butyl)phosphine has a χ-value of zero per definition. The difference in the frequency of the Ni-CO stretch compared to the Ni-CO stretch frequency of tris(*tert*-butyl)phosphine gives the χ-value of a ligand. The higher the value of χ, the better the π-acceptor ligand. Phosphites with high π-acceptor ability are found in the range of 20 to 40 in χ-value thus making them a better choice for oxo-reaction when high selectivity is desired [73].

When coordinated to a transition metal, phosphite ligands will compete with the coordinated CO ligands for the back-donation of electron density from the metal to the ligand. This results in a weaker metal-carbonyl bonding, thus facilitating CO dissociation from the central metal atom, which is vital for the oxo catalyst activation. A widely used phosphite ligand for high selectivity towards the linear aldehydes is (6,6′-[(3,3′-Di-tert-butyl-5,5′-dimethoxy-[1,1′-biphenyl]-2,2′-diyl)bis(oxy)]bis(6H-dibenzo[d,f][1,3,2]dioxaphosphepine)) also known as BiPhePhos (Figure 2.2) [74]. In addition to BiPhePhos, Naphos (2,2′-bis(diphenylphosphinomethyl)-l,l′-binaphthy), Iphos (2,2′-bisbis[3,5-bis(trifluoromethyl)phenyl]-phosphanylmethyl-1,1′-binaphthyl), Xantphos and water-soluble sulfonated SulfoXantphos (Figure 2.2) have also showed remarkable selectivity towards the linear aldehydes.

In addition to the experimental studies, a number of quantum mechanical investigations were performed on hydroformylation, see the review by Kégl [75].

Carbó et al. have investigated the steric effect of ligands on the regioselectivity using a QM/MM approach and reported a notable reduction in selectivity towards the linear products upon removing the phenyl rings of the bulky XantPhos ligand [76]. Despite all the computational studies, there is, however, still a controversy about the rate-determining step in the reaction. For example, the H_2 oxidative addition was reported to have the highest activation barrier when using $(PH_3)_2RhH(CO)_2$ as a catalyst [77, 78]. Later, NMR experiments by van Rooy et al. [79] and FTIR by Jörke et al. [80] suggested an early rate-determining step (the olefin insertion) when using a bulky electron withdrawing diphosphite ligand (BiPhePhos). In addition, CCSD(T) calculations suggested that olefin coordination/insertion is the rate-determining step [81, 82].

Often, hydroformylation quantum chemical studies are conducted on simplified systems by reducing the complexity of the ligand or by using truncated substrate models for reasons of computational efficiency [78, 82–84]. These simplified, truncated catalytic models are unable to fully account for ligand effects, as the geometric and electronic properties of the ligand significantly influence the catalyst's selectivity and rate of reaction. By utilizing the complete BiPhePhos ligand structure, the experimental product selectivity can be elucidated (See Chapter 4).

2.2 Reductive amination

Aliphatic amines are critical intermediates for the production of many high value products such as agrochemicals, solvents, lubricating oils, waterproofing agents in textiles, detergents, dyes, building blocks for polymers and pharmaceuticals [85], with a production on a million ton scale annually [86]. There are various reactions known for the synthesis of amines, such as hydrocyanation of alkenes followed by reduction, nucleophilic substitution of alkyl halides, reductive amination, hydroamination, etc. However, amine preparation often suffers from low selectivity, expensive starting materials, side reactions and the requirement for protecting groups [87].

The reductive amination of the aldehydes in itself is a two-step reaction consisting of amination of an aldehyde, followed by the reduction of the enamine complex produced (See Figure 2.4). The reduction of enamine can be carried out either via hydrogenation, where hydrogen as reducing agent must be activated using a transition-metal catalyst or by reducing agents such as sodium borohydride [88]. The use of hydrogen as the reducing agent is preferred for large- or larger-scale alkyl

amine formation since it is inexpensive and can be generated sustainably (see Figure 1.2) [89].

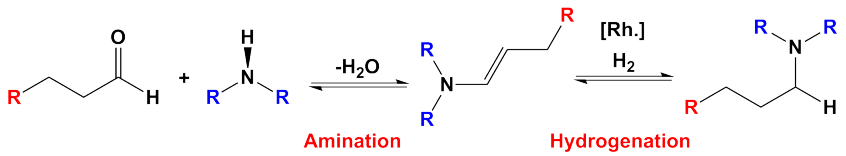

Fig. 2.4.: Formation of tertiary amines from aldehydes via reductive amination.

Reductive amination using transition metal catalyst in homogeneous phase was first described by Markó and Bakos in 1974 using rhodium- and cobalt-based carbonyl catalysts under rather harsh reaction conditions (200°C and 300 bar) [90]. Then, until 1990s, no further investigations of homogeneously catalyzed reductive amination were carried out. In 1999, Blaser and co-workers reported reductive amination using an iridium-based catalyst with a ferrocene-based ligand Xyliphos under relatively milder reaction conditions (50°C and 80 bar) [91]. In early 2000s, Beller and co-workers showed formation of primary amines using benzaldehyde and ammonia with a good yield (86%) and selectivity (97%), using a water-soluble TPPTS monophosphine (Figure 2.2) ligand with rhodium and iridium as active metals [92].

In addition to these, catalysts with transition metals such as nickel, ruthenium, molybdenum, iron, manganese and tin have also been reported for reductive amination (details can be found in reference [89]). Although, catalysts with several transition metals are reported, the catalysts with rhodium still dominate the field. Catalytic selectivity during the reductive amination of aldehydes is an important issue as the hydrogenation of the starting aldehydes producing corresponding alcohols is the dominant side reaction and, thereby, must be suppressed by using a highly selective catalyst.

2.3 Hydroaminomethylation

Hydroaminomethylation (HAM) converts olefins to amines in the presence of syngas (CO/H_2) with high atomic efficiency. With only water as side product, HAM was first discovered in 1949 by Walter Reppe at BASF (Figure 2.5) [93]. The HAM reaction involves the succession of two steps: hydroformylation and reductive amination. In the first step, the alkenes are converted into the linear or branched aldehydes, which then react with the primary or secondary amines present in the reaction medium

to give the enamines or imines. Finally, hydrogenation of the enamine or imine intermediates gives the final amine product.

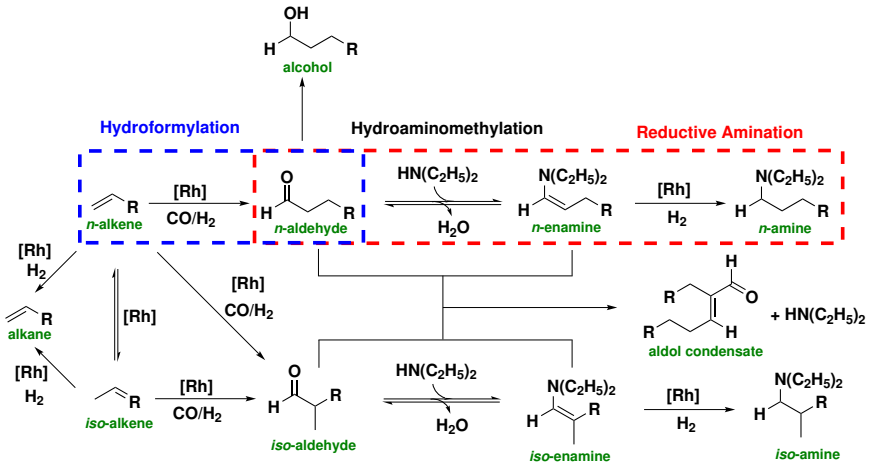

Fig. 2.5.: Rhodium-catalyzed hydroaminomethylation (HAM) of long chain olefins (here 1-decene) and diethylamine and possible side reactions.

Although hydroaminomethylation of long chain olefins obtained from renewable resources is an efficient way for the preparation of amines, certain challenges exist. The main difficulty is to ensure high selectivity to suppress the formation of the side products. As a matter of fact, side reactions are often observed which can occur after the formation of certain reaction intermediates. For example, the aldehyde formed in hydroformylation can undergo aldol condensation and long chain olefins are susceptible to isomerization thus generating internal olefins and aldehydes. Furthermore, byproducts like alkanes and alcohols can also be observed due to the hydrogenation of the alkene substrates and the aldehyde intermediates.

Despite being discovered in the late 1940s, the majority of report concerning HAM have surfaced since 1990s. The first $Fe(CO)_5$ catalyst used by Reppe et al. required the heating of the substrates involved upto 300°C, the pressure of 150 bar and large amounts of the catalyst [93]. Due to the low efficiency of the iron catalyst, efforts have been made to develop new more reactive cobalt based catalysts. Using the cobalt based catalysts the temperature and pressure required for HAM were significantly reduced (170-262°C and 40-75 bar) for ethylene and ammonia as substrates [94], however the catalytic activity was low. Since then, various other transition metal catalysts with rhodium [95, 96], ruthenium [97], cobalt [98] and iridium [99] have been developed and tested showing enhanced catalytic activity and selectivity. In addition, catalysts employing nickel and manganese were also reported [100], however the reaction could only be performed under

harsh reaction conditions (> 50 bar and > 200°C). Among the metals used for hydroaminomethylation, rhodium was found to be the most active and selective in catalyzing both the hydroformylation and the hydrogenation steps and HAM could be carried out under milder conditions (100 °C and 30 bar) [101]. The first rhodium-catalyzed HAM was reported by Iqbal in 1971 using a simple Rh_2O_3 catalyst without the presence of an organic ligand [102]. In addition to rhodium, cobalt-based catalysts are still used to this date. Although, Bouwman, Bickelhaupt and co-worker stated very recently: "The use of cobalt-based catalysts in the HAM reaction (...) seems therefore not feasible" [103], several studies have reported cobalt-based catalysts for HAM [98].

The high activity and selectivity is one of the main reasons for the success of Rh-based hydroaminomethylation process. Considering the scarcity of the precious noble metals, economical viability of chemical processes, the amount of precious metal catalyst must be optimized and efficient methods for separation and recovery must be developed. The development of hydroaminomethylation has already been summarized in several review articles [96, 100, 104]. In addition, the search for alternative transition metals (besides Rh) and ligand modifications are extremely important in catalyst design.

Phosphine (strong σ-donors, weak π-acceptors) ligands are known to increase the electron density at the metal center, thereby reducing π-acceptor back-bonding to the alkene group. Phosphites (weak σ-donors, strong π-acceptors), on the other hand lower the electron density at the metal center and facilitate catalyst activation [105]. The steric hindrances offered by these ligands determines the selectivity of the reaction thereby increasing the amount of desired product in the catalytic mixture with the least amount of side products. A rigid, bulky bidentate ligand improves the coordination of alkenes to the catalyst and the post-reaction products dissociation during HAM [105].

Zimmermann et al. have reported the hydroaminomethylation of olefins with ammonia to form primary and secondary aliphatic amines using a monophosphorus (3,3′,3″-Phosphanetriyltris(benzenesulfonic acid) trisodium) TPPTS ligand due to its high solubility in water [106]. Later, Whiteker et al. have reported a monophosphite (TBPP) ligand for HAM using 1-pentene as substrate (See Figure 2.6) [107]. Both of those ligands showed high activity compared to the classic PPh_3, however, like many other mono phosphorous ligands, they also suffer from low selectivity [108]. Clark et al. have investigated the electronic effects of monophosphine ligands on HAM and showed that electron withdrawing ligands are more active than the electron

donating monophosphorus ligand, which is in contrast with the widely held view that activity of olefin hydrogenation increases with the ligand donor strength [109].

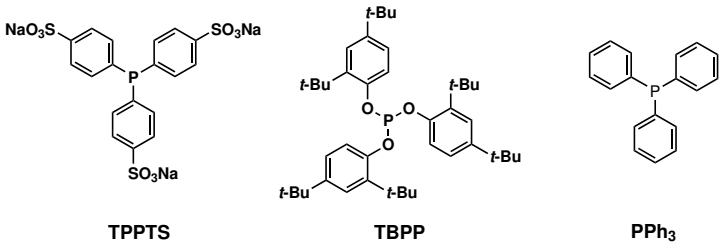

Fig. 2.6.: Monophosphorus ligands for hydroaminomethylation of olefins. Adapted from [67].

As mentioned previously, whenever high selectivity is required, diphosphorous ligands are preferred over the monophophorus ligated transition metal catalysts. In 2002, Seayad et al. reported the selective synthesis of linear amines from terminal and internal olefins using cationic rhodium precursor $[Rh(COD)_2BF_4]$ (COD = 1,5-cyclooctadiene) with bulky diphosphine ligands in a single pot hydroaminomethylation for the first time [110]. Among all the ligands tested, it was found that Iphos gave the best results showing excellent chemo- and regio-selectivity for the isomerization-hydroaminomethylation of 2-butene. In the next year, the same group investigated hydroaminomethylation using Xanphos as the bidentate ligand at 40 bar CO/H_2 and showed its remarkable activity and selectivity for HAM at 125 °C [111]. It was also found that the selectivity for the linear product follows a similar trend to that observed in the hydroformylation of internal alkenes with the use of XantPhos ligands. Furthermore, each of the individual steps in hydroaminomethylation was monitored by high-pressure infrared spectroscopy. The results have suggested that hydroaminomethylation takes place by a sequential isomerization/hydroformylation/amination/hydrogenation pathway [70].

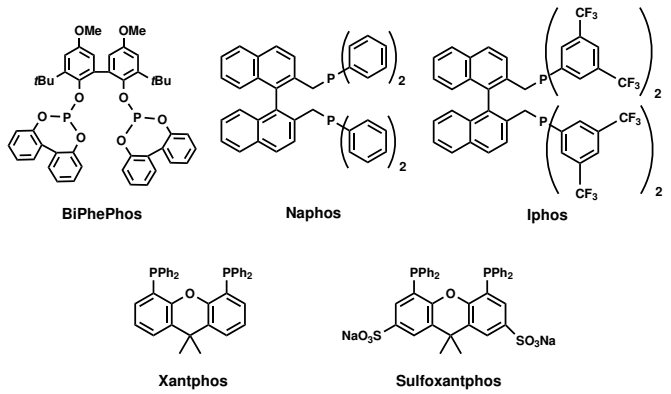

Fig. 2.7.: Bisphosphine ligands for hydroaminomethylation. Adapted from [67].

Rh/Xantphos catalytic system for the hydroaminomethylation of terminal olefins in low-viscous ionic liquid with a particular interest in catalyst recovery was also investigated by Vogt et al.[112]

In addition, of particular interest are diphosphine ligands that can convert long chain aliphatic olefins into linear amines with high linear to branched selectivity reaching to 99:01. Examples are Naphos, Iphos, di-*t*-Bu-Xantphenoxaphos and Xantphos that show bite angles ranging from 111 to 123° (see Figure 2.7). Several review articles give a comprehensive overview of catalyst-ligand systems for hydroaminomethylation [96, 104, 113, 114].

An efficient one-pot procedure to prepare a diamine via bis- hydroaminomethylation of 1-octene with piperazine was developed by Vorholt group at TU Dortmund [115]. By using the [Rh(acac)$(CO)_2$]/BiPhePhos, at 120°C and 40 bar CO/H_2 (17:23), 1,4-dinonylpiperazine was obtained with an 80% yield and a *l/b* ratio of 77:23. Other linear and branched 1-alkenes were also investigated. Notably, 3,3-dimethylbut-1-ene afforded the corresponding dialkylpiperazine with 87% yield and a *l/b* ratio of 99:1. Despite its high reactivity and selectivity rhodium catalyst with BiPhePhos ligand is prone to catalyst leaching in the presence of water as product of amination reported by Vorholt et al. [116]

The use of the water-soluble SulfoXantphos ligand enables high yields and selectivities, but require long time for catalyst formation. This can be overcome by preforming the catalyst preparation in the absence of the olefin at reaction temperature [117]. More recently, Vogt et al. investigated the Rh-catalyzed aqueous biphasic hydroaminomethylation of 1-decene with diethylamine for a potential continuous process application using the [Rh(acac)$(CO)_2$]/SulfoXantphos (acac = acetylacetonato) system [118].

3 Theoretical Background

In the following chapter, the basics of computational methods to calculate the electronic and Gibbs free energies of molecular species in gas and solvent will be discussed. Fundamental concepts and approximations for quantum mechanics (QM) and Density Functional Theory (DFT) will be introduced. The improvement in the accuracy of method will be discussed in the light of increasing sophistication of the functionals available and diverse basis sets.

In addition, the calculations of free energy solvation for reaction complexes (intermediates and transition states) and the basics of different solvation models will be discussed.

3.1 Solving the Electronic Schrödinger Equation

Schrödinger equation (3.1) describes the energy of a single particle in space and time based on its wavefunction (Ψ). The wavefunction relates to the positions of the electrons and nuclei in a given atom or molecule and can be used to calculate the probability of finding the particle in a particular region. The Hamiltonian operator, $\hat{H}$, contains a set of terms relating to kinetic and potential energy that, when acting on the wavefunction, describes the energy of the particle is represented as E.

$$\hat{H}\Psi_{(r,\,t)} = E\Psi_{(r,\,t)} \tag{3.1}$$

To solve the Schrödinger equation it is necessary to find values of Ψ such that, when the wavefunction operated upon by the Hamiltonian, it returns the wavefunction multiplied by the energy [119]. However, the solution of the Schrödinger equation of multi-electron system is not possible. Thereby, two approximation are made to make the solution possible. First, it is assumed that the potential energy of the system does not depend explicitly on time, thus, resulting in the time-independent Schrödinger equation.

Second, is known as the Born-Oppenheimer approximation [120], where the motion of atomic nuclei and electrons can be separated and considered independently (Eq. 3.2). This is possible due to the significant difference in the mass between electrons

and nuclei, for example, in a H_2^+ molecule the proton is 1836 times heavier than the electron.

$$\Psi_{tot(nuclei,electrons)} = \Psi_{(electrons)}\Psi_{(nuclei)} \tag{3.2}$$

The Born-Oppenheimer approximation involves the following assumptions:

- Due to the significant mass difference nuclei moves much slower than electrons. Therefore the electronic wavefunction only depends on the positions of the nuclei, not on their velocities. Thus, their motion can be considered independent of the electronic motion.

- Nuclear motion sees an average potential from the electrons.

Under this approximation, the kinetic energy of the nuclei is neglected and potential energy due to nucleus-nucleus repulsion only depends on the positions, therefore the Hamiltonian can now be converted into the electronic Hamiltonian and total energy (E_{tot}) of any system can be calculated using eq 3.4, where E_{nuc} is the nuclear repulsion energy.

$$\hat{H}_{elec}\Psi_{elec} = E_{elec}\Psi_{elec} \tag{3.3}$$

$$E_{tot} = E_{elec} + E_{nuc} \tag{3.4}$$

Equation (3.3) always has multiple solutions with different wavefunctions and different energies. However, the solution with lowest energy is called the ground state energy. From here on, the total electronic energy (E_{elec}) will be referred to as ground state energy. The electronic Hamiltonian $\hat{H}_{elec}$ is composed of the kinetic ($\hat{T}$) and potential operators ($\hat{V}$) of nuclei, and ($\hat{U}$) is the electron-electron interaction energy.

$$\hat{H}_{elec} = \hat{T} + \hat{V} + \hat{U} = \sum_{i=1}^{N}\left(-\frac{\hbar^2}{2m_i}\nabla_i^2\right) + \sum_{i=1}^{N}V(\mathbf{r}_i) + \sum_{i<j}^{N}U(\mathbf{r}_i,\mathbf{r}_j) \tag{3.5}$$

There are multiple quantum chemical approaches available with the ability to solve electronic Schrödinger equation in the Born-Oppenheimer approximation (Figure 3.1). Following is a small introduction of the approaches available for the solution of Schrödinger equation, more details can be found in the subsequent sections.

One of the most commonly known is the Hartree-Fock (HF) method [121–123]. The approximation in the Hartree-Fock theory is the assumption that, in a molecular system, the movement of electrons is independent of one another. The benefit of this approximation is: for a many-electron system, the wavefunction (Ψ) for all

electrons can be written as a product of wavefunctions for individual electrons, called molecular orbitals.

$$\Psi(r_1, r_2, ..., r_n) \cong \Psi_1(r_1) \times \Psi_2(r_1) \times ... \times \Psi_1(r_n) \tag{3.6}$$

This equation does not include the electronic spin and thus it must be taken into account by introducing an additional spin term in the wavefunction.

After including the electronic spin, the Hartree-Fock approximation enable the solution of Schrödinger equation. However, this solution is not exact since, the true wavefunction of a many-electron system is not a Hartree-Fock wavefunction. Since it is impossible to calculate an exact solution of Schrödinger equation for a many-electron system, only an approximate wavefunction and the ground state energy, can be estimated using variational principle. The variational principle states that the energy calculated from an approximation to the true wavefunction will always be greater than the true ground state energy. The Hartree-Fock wavefunction composed of the set of molecular orbitals and electronic spin gives the lowest possible energy of a many-electron system. Thus by varying the Hartree-Fock wavefunction, the expectation value of electronic Hamiltonian is minimized and, as a result, approximate wavefunction and ground state energy can be obtained. Although, this energy will be larger than the true ground-state energy, it will be the closest one to the exact ground state energy that can be estimated by solving the Schrödinger equation.

The difference between the exact ground state energy and energy obtained from Hartree-Fock method is called correlation energy. The physical reason for this deference is that electron position are correlated: this means that the probability that a given electron will be in one place at a certain time is dependent on where another electron is placed at the same instant.

In the context of traditional wavefucntion-based methods, multiple schemes are available to treat the electron correlation problem. The first is configuration interaction (CI) method as it considers more than one electronic configurations and, thus, can include electron correlation effects by allowing excited configurations. Theses excited configurations are generated by moving the electrons from fully occupied to vacant atomic orbitals. Therefore, for an n electron system, it is possible to have up to n-tuple excitations. If all possible excitations are taken into account, then the method is called full configuration interaction (FCI). Using FCI, it is then possible to calculate ground state energy exactly. However FCI is computationally very expensive and is limited to very small systems.

The second technique to account for the electron correction in many-electron system is the Møller-Plesset (MP) theory. MP theory is a perturbative approach, in which the 'true' Hamiltonian operator $\hat{H}$ is expressed as the sum of a 'zeroth-order' Hamiltonian $\hat{H}_0$: resulted from Hartree-Fock method and a perturbation. The eigenfunctions of the true Hamiltonian give the wavefunction Ψ with corresponding ground state energy. The correlation energy is then calculated as a series of corrections to the HF energy, where each term corresponds to a different order in the perturbation expansion. The first-order correction, known as MP1, includes the effects of electron correlation due to the interaction between pairs of electrons. The second-order correction, MP2, includes the effects of electron correlation due to the interaction between pairs of electrons and virtual orbitals. Higher-order corrections are also possible, but their contribution to the correlation energy becomes increasingly small. The limitation of MP theory is nonlinear scaling of correction energy to the size of the system.

Another powerful method is Coupled Cluster (CC) approach, similar to configuration interaction (CI) this method involves electron excitation. However, in contrast to CI, CC method is an iterative approach that expands the wavefunction with an exponential series of excitation or cluster operators acting on the Hartree-Fock reference wavefunction. The correlation energy is then calculated as the difference between the CC energy and the Hartree-Fock energy. CCSD(T), where 'SD' stands for single and double excitation are treated using variational principle and 'T' when triple excitation are accounted by using a perturbative method is considered as 'Gold standard' in quantum chemical calculations when high accuracy is required [124].

The above methods include electron correlation in a formally correct manner however, their applicability is limited to only small system due to the costs attributed with the calculations.

In addition to the wavefunction based methods, Density Functional Theory (DFT) is another widely used method for calculating the energy of multi-electron systems as it is based on the electron density rather than the wavefunction (See section 3.1.1).

A faster alternative to the above mentioned methods is the semi-empirical (SE) QM approach, where experiment (empirical) data is used in combination with the aforementioned quantum chemical methods to obtain approximate ground state energies of molecules. These methods are particularly useful for large molecules, where it is impractical to use computationally intensive quantum chemical methods. Examples of semi-empirical methods are Austin Model 1 (AM1) method, PM3

(parameterized method three), and PM6. These methods are based on the approximation of Hartree-Fock methods, where experimental data is used to simplify the energy equation.

Semi-empirical methods based on density functional theory also exist, such as DFT-tight-binding approach. A successful example of these methodologies is Geometry, Frequency, Non-covalent, extended TB (GFN*n*-xTB), where *n* is an integral number, referring to different levels [125].

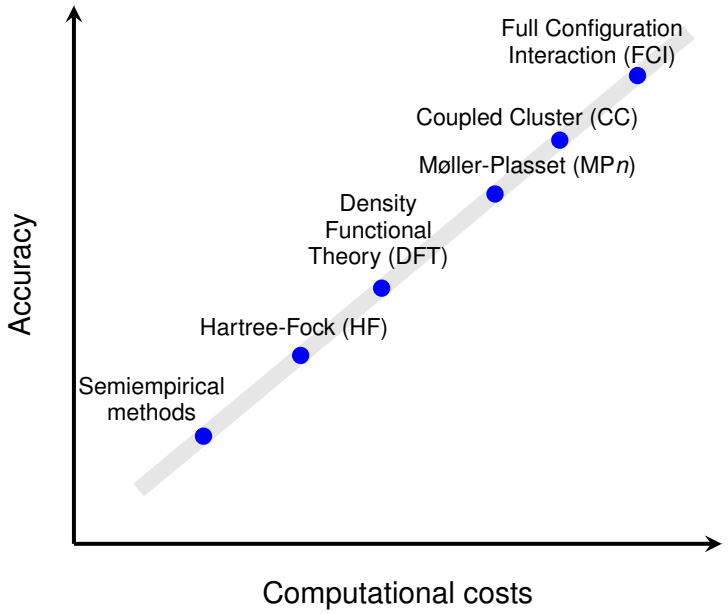

Fig. 3.1.: Methods available for the calculation of energies of multi-electron systems and their computational costs. Adapted from [126].

3.1.1 Density Functional Theory

Another way for the calculation of the electronic ground state energy is Density Functional Theory (DFT). Here, the central object is not wavefunction, but instead the energy of a molecular system is calculated as a function of the electron density (ρ). DFT, first introduced in 1964, is based on two theorems formulated by Hohenberg and Kohn [127]:

- The ground state electronic density, ρ_0(r), uniquely determines the external potential, $\hat{V}_{ext}$.

- There exists a functional E[ρ(r), $\hat{V}_{ext}$] for any external potential $\hat{V}_{ext}$ such that the electron density ρ(r) that minimizes this functional is the exact ground state density.

Thus, the ground state energy of a system can be determined by the global minimum value of

$$E[\rho] = \int \rho(r) V_{ext} dr + F[\rho] \tag{3.7}$$

Where the external potential (V_{ext}) is subjected to the constraint $\int dr\rho(r) =$ N, where N refers to the total number of electrons in the system. It has been shown that different electron densities yields different energies, this is due to the fact that the functional ($F[\rho]$) connecting electron density and ground state energy is unknown (See eq. 3.7).

The energy functional (F[ρ]), is composed of kinetic energy $T[\rho]$, electron-nuclear attraction $E_{Ne}[\rho]$ and electron-electron repulsion $E_{ee}[\rho]$

$$E[\rho(r)] = T[\rho] + E_{Ne}[\rho] + E_{ee}[\rho] \tag{3.8}$$

The electron-electron repulsion can further split into Coulomb (electrostatic), $J[\rho]$, and $K[\rho]$ parts. $K[\rho]$ is the non-classical contribution to the electron-electron interaction containing all the effects of self-interaction correction, exchange and Coulomb correction. Electron-nuclear and Coulomb terms can be calculated using the eq. 3.9 and 3.10. The explicit expression for $K[\rho]$ is still unknown, thus when combined with the kinetic energy correction $T_C[\rho]$, which is not covered by $T[\rho]$ becomes the exchange-correlation energy (See eq. 3.11) of the system (See below).

$$E_{Ne}[\rho] = \sum_{i=1}^{Ne} \sum_{\alpha=1}^{N\alpha} \int \frac{Z_\alpha \rho(r_1)}{r_{1\alpha}} dr_1 \tag{3.9}$$

$$J[\rho] = \frac{1}{2} \int \int \frac{\rho(r)\rho(r')}{|r - r'|} dr dr' \tag{3.10}$$

$$\tilde{E}_{XC} = T_C[\rho] + K[\rho] \tag{3.11}$$

Thus, the exchange-correlation energy contains in itself everything what is unknown. If the exchange-correlation functional was known, the ground state energy can be calculated exactly. However, that is not that case, therefore, exchange-correlation energy must be modelled. To do that, large number of density functionals have appeared in the past and is still an active area of research today (for details, please refer to the following section).

Earlier functionals considered the electron density to be a non-interacting electron gas, thus considering only kinetic and exchange terms. However, this assumption leads to a significant error in total energies of the molecules.

Kohn and Sham have addressed this issue by using orbitals in DFT calculations, leading to improved accuracy of the calculated energies. The Kohn-Sham ansatz [128] for solving eq. (3.7) replaces the fully interacting many-body system with a system of independent particles. The ansatz has two major benefits:

- it reduces the complexity by using single particle systems instead of the many-particle original system
- it separates the kinetic energy term and the interaction of the Hartree term in such as way that the non-classical interaction of the electrons, exchange and correlation, are gathered into one term

Thus, eq. (3.7) takes the form,

$$E_{DFT}[\rho] = T_0[\rho(r)] + E_H[\rho(r)] + \tilde{E}_{XC} + \int drV_{ext}(r)\rho(r) \tag{3.12}$$

Where, T_0 is the kinetic energy of the non-interacting particles, E_H refer to the Coulomb interactions (Hartree energy) and the exchange-correlation of electron is accounted with $\tilde{E}_{XC}$.

3.1.2 Exchange-Correlation Functionals

The exchange-correlation term in equation (3.12) includes the non-classical portion of the electron-electron interactions along with the correction for the self-interaction and the kinetic correlation energy. The quality of density functional theory solely relies on the accuracy of the chosen approximation for $\tilde{E}_{XC}$. Several approximations (classes of functional) are available to model this charge depletion, such as:

- Local Density Approximation (LDA)
- Generalized Gradient Approximation (GGA)
- Meta GGA (*m*-GGA)
- Hybrid Functionals
- Double Hybrid Functionals

Moving down the list, more terms are included in the functional and, as a result, the computational costs increase as well.

Local Density Approximation (LDA)

The local density approximation evolves from the idea of an uniform electron gas, as it assumes uniform electron density around the atom or molecule, thus the contribution to exchange-correlation energy is equal in space. The exchange-correlation energy can be calculated using the following equation.

$$E_{XC}[\rho(r)] = \int \rho(r)\epsilon_{XC}[\rho(r)]dr \tag{3.13}$$

where ϵ_{XC} is the exchange-correlation energy per electron in a uniform electron gas, which can be calculated using Monte Carlo simulations, and $\rho(r)$ refer to the electron density.

The performance of the local density approximation can further increased by incorporating electronic spin, in addition to the electron density which is called as local spin-density approximation (LSDA) [129, 130].

$$E_{XC}^{LSDA}[\rho^{\alpha}\rho^{\beta}] = \int d^3r\rho(r)\epsilon_{XC}(\rho^{\alpha}(r), \rho^{\beta}(r)) \tag{3.14}$$

where, ρ_{α} and ρ_{β} are the spin densities. In systems with a slowly varying electron density, such as, in homogeneous electron gas or simple metal-like systems, LDA has proven successful in predicting properties such as bond lengths. However, in systems where the electron density varies rapidly (e.g., molecules), or in strongly correlated systems, the LDA generally overestimates bond distances thus, resulting in shorter bonds [131].

Generalized Gradient Approximation (GGA)

Since the electron density is far from uniform in a molecule, the gradient of the energy density, $\nabla\rho(r)$, can also be taken into account. By using $\rho(r)$ and $\nabla\rho(r)$, this new type of functional form is called generalized gradient approximation (GGA) functional.

Most gradient corrected functionals are constructed with the correction being a term added to LDA functional:

$$E_{XC}^{GGA}[\rho(r)] = \int f(\rho(r), \nabla\rho(r))dr \tag{3.15}$$

For GGA functionals, the exchange-correlation terms can be separated into to exchange and correlation terms which can be calculated individually.

$$E_{XC}^{GGA} = E_{X}^{GGA} + E_{C}^{GGA} \tag{3.16}$$

$$E_{X}^{GGA} = E_{X}^{LDA} - \sum_{\sigma} \int F(s_\sigma)\rho_\sigma^{4/3}(r)dr \tag{3.17}$$

Where, function F is the reduced density gradient for spin σ

$$s(_\sigma)(r) = \frac{|\nabla\rho_\sigma(r)|}{\rho_\sigma^{4/3}(r)} \tag{3.18}$$

Here, s_σ is the local inhomogeneity parameter and s_σ=0 refers to homogeneous electron gas. A widely used expression for function F was proposed by Becke [132].

$$F = \frac{\beta s_\sigma^2}{1 + 6\beta s_\sigma h^{-1} s_\sigma} \tag{3.19}$$

Where β is an empirical parameter (0.0042) determined by a least-square fit to the exactly known exchange energies of noble gas atoms He through Rn. The correlation functional was later introduced by Perdew in 1986 [133]. Combined, they both form a well known GGA type exchange-correlation functional (BP86).

$$E_{C}^{GGA} = \int d^3r\rho\epsilon_c + \int \frac{d^{-1}e^{\Phi}C|\nabla\rho|^2}{\rho^{4/3}}d^3r \tag{3.20}$$

where

$$\Phi = 1.745\overline{f}\left[\frac{C(\infty)}{C(\rho)}\right]\frac{|\nabla\rho|}{\rho^{7/6}} \tag{3.21}$$

ϵ_C refers to correlation energy per particle of the uniform electron gas and $\overline{f}$ is cutoff a parameter with a value of 0.11. In addition to BP86, there exist several other GGA type functionals with different expressions for either exchange or correlation or both such as BLYP, PBE, etc.

Meta-GGA

To further increase the accuracy of GGA type functionals, the next step is to consider the second derivative of the electron density, $\nabla^2\rho$. Estimating a stable, numerical solution from Laplacian of electron density might be challenging, so an alternative method is needed. A possible formulation of meta-GGA functional is to include a dependence on the kinetic energy, (τ), within the exchange-correlation potential [134] τ can be defined as:

$$\tau(\rho) = \sum_{i}^{occupied} \frac{1}{2}|\nabla\psi(\rho)|^2 \tag{3.22}$$

where ψ are the self consistently determined Kohn-Sham orbitals. With the computational costs comparable to GGA type functionals, meta-GGA type functionals outperform the former resulting in accurate electronic energies and barrier heights. Commonly known meta-GGA functionals for exchange, correlation or both are B95, B98, VSXC, TPSS and r^2-SCAN.

Hybrid Functionals

The energy contributed by the exchange terms is much larger than the correlation term, therefore, an accurate estimation of exchange energy contribution is vital for the calculation of ground state energies. In 1993, Becke introduced 'hybrid' exchange-correlation functionals by combining GGA functionals and exact Hartree-Fock non-local exchange resulting in a new family of hybrid functionals.

By using only a small fraction of Hartree-Fock exact exchange, the DFT results are significantly improved. One of the most commonly used hybrid density function is Becke's three-parameter hybrid functional called B3LYP (see eq. 3.23). It consists of a comibination of Slater-Dirac (S) [135, 136], Becke's 1988 (B88) [132] and, Hartree-Fock (HF) exchange and, Lee, Yang and Parr's (LYP) and, Vosko, Wilk, and Nusair (VWN) [137] correlation functionals.

$$E_{XC}^{B3LYP} = 0.8 \cdot E_X^S + 0.72 \cdot E_X^{B88} + 0.2 \cdot E_X^{HF} + 0.19 \cdot E_C^{VWN} + 0.81 \cdot E_C^{LYP} \tag{3.23}$$

Another popular hybrid density functional is PBE0 [138, 139], which combines Perdew, Burke and Enzerhof exchange (GGA)[140], 0.25 HF exact exchange and Perdew and Wang's correlation functional.

$$E_{XC}^{PBE0} = 0.25 \cdot E_X^{HF} + 0.75 \cdot E_X^{PBE} + E_C^{mPW91} \tag{3.24}$$

A rigorous benchmark study for the performance of transition metal catalyzed reactions has shown that, among all the tested hybrid functionals, PBE0 performed best [141].

Double Hybrid Functionals

Double hybrid density functionals, the first one (B2-PLYP) reported in 2006 [142], have since gained considerable attention in the computational chemistry community. The motivation behind the double hybrid density functionals are similar as in hybrid density functionals. While in the latter, only a portion of the exchange term is substituted by Fock-exchange, the double hybrid density functionals additionally replace part of the correlation functional with a non-local correlation contribution based on second-order Møller-Plesset perturbative treatment (MP2).

The general formulation of double hybrids can be seen in eq. 3.25

$$E_{XC} = (1 - a_X)E_X^{GGA} + a_X E_X^{HF} + (1 - a_C)E_C^{GGA} + a_c E_C^{MP2} \tag{3.25}$$

where E_X^{GGA} is the DFT exchange energy, E_X^{HF} the HF exchange energy, E_C^{GGA} the DFT correlation energy, and E_C^{MP2} the non-local second-order perturbative energy. E_X^{HF} and E_C^{MP2} are scaled by the parameters a_X and a_C, respectively. The values of the two mixing parameters a_X and a_C in Eq. 3.25 have been fitted to small-molecule heats of formation of the G2/97 test set and they amount to 0.53 and 0.27, respectively [143].

Double hybrid density functionals stand computationally expensive compared to the other types of the functionals available. They show high accuracy ($\sim$ 1 kcal/mol) compared the CCSD(T) quantum chemistry 'gold standard', showed in a recent detailed review by Goerigk et al. after a benchmark study of transition metal catalyzed organic reactions [144].

3.1.3 Dispersion Corrections

The lack of the description of long-range London dispersion interactions is a fundamental shortcoming of DFT. However they can be added to the exchange-correlation energy term by using several available dispersion correction schemes such as D4, D3, D3(BJ) and VV10 [145].

$$E_{XC} + E_{disp} = E_{XC}^{disp} \tag{3.26}$$

Dispersion interactions can be empirically defined as: the attractive part of the van der Waals (vdW)-type interaction potential between atoms and molecules that are not directly bonded to each other [146]. The dispersive interaction between two instantaneous electric dipoles can be formulated as: $-\frac{C_6}{R^6}$, where C_6 is a constant, called dispersion coefficient, and R represents the distance between the dipoles. The considration of higher order multipole terms, such as C_8, which captures dipole-quadropole interactions, and C_{10}, capturing quadrupole-quadrupole interactions may result in more accurate dispersion energy. The total dispersion energy is then cal be calculated as a sum over all theses pairwise interactions for atoms i and j

$$E^{disp} = -\sum_{i<j}\left(\frac{C_{6,ij}}{R_{ij}^6} + \frac{C_{8,ij}}{R_{ij}^8} + \frac{C_{10,ij}}{R_{ij}^{10}} + \dots\right) \tag{3.27}$$

This series expansion is truncated at different orders, depending on the model used for the discription of London dispersion forces. This expression is only valid for long-range interactions, therefore, damping fuctions are used to prevent divergance at short inter-atomic distances (see below). The pairwise atomic parameters within the dispersion coefficients C are either obtained from experimental parameter fitting or from high level quantum chemical (CCSD or MP2) calculations.

A commonly used approach for the calculation of dispersion correction E_{disp} is DFT-D3 (first introduced by Stefan Grimme) [147] with Becke Johnson damping [148] is formulated as:

$$E_{disp}^{DFT-D3(BJ)} = -\frac{1}{2}\sum_{i\neq j}\sum_{n=6,8} s_n \frac{C_n^{ij}}{R_{ij}^n + [f_{damp}^{DFT-D3(BJ)}(R_{BJ}^{ij})]^n} \tag{3.28}$$

where i and j represent individual atoms or molecules, s_n are scaling parameters, R_{ij} represents the cutoff radius and C_n are dispersion coefficients for each atom pair.

The damping function helps to avoid the double-counting of electron correlation effects, since short to medium-range correlation is normally included with the density functionals. The damping function f_{damp} for DFT-D3 is:

$$f_{damp}^{DFT-D3(BJ)}([(R_{BJ}^{ij})]^n) = a_1[R_{BJ}^{ij}]^n + a_2 \tag{3.29}$$

The parameters a_1 and a_2 are adjustable and they control the dispersion corrections in short to medium range regimes. The dispersion coefficients for commonly used density functionals are available in the recent works of Grimme *et al* [149].

Dispersion correction can be included into any DFT functional (Eq. 3.26). The inclusion of dispersion corrections is mandatory for realistic calculations on large or condensed chemical systems, since it results in better agreement with highly accurate CCSD energies compared to the performance of the density functionals without the added dispersion corrections [141, 145].

3.1.4 Basis Sets

The basis functions represent atomic orbitals and a basis set is a set of functions combined to represent molecular orbitals. The size of a basis set depends on the number of basis functions assigned to molecular orbital. Many basis sets have been carefully optimized and tested over the years. In principle, the largest basis set available should be employed in order to model molecular orbitals as accurately as possible. However, the computational cost grows rapidly with the size of the basis set so a compromise must be sought between accuracy and cost.

A number of errors, such as basis set incompleteness error (BSIE) and basis set superposition error (BSSE) can emerge by choosing inappropriate basis sets. BSIE can occur when basis functions employed to describe a molecular orbital are insufficent. BSSE emerges from BSIE when spatially close atoms and fragments start to "borrow" basis functions from each other, resulting in an artificial energy lowering for more compact structures.

These errors can be addressed by avoiding very small basis sets when high accuracy is required. The commonly used basis sets belongs to Ahlrichs (def2-XVP), Pople (e.g., 6-31G), Duning (cc-pVXZ) and Jensen (pc(seg)-X) families. More details about these basis sets can be found in any quantum chemistry textbook [134].

The density functionals and basis set used for this work were chosen after benchmark study where, the performance of semi-empirical DFT method (GFN*n*-xTB) and different density functionals and basis set was evaluated against DLPNO-CCSD(T) calculations for a number of rhodium catalyzed organic reactions. The choice to benchmark set was inspired by the MOR41 dataset reported by Goerigk et al. [141], from which all rhodium catalyzed reaction were considered in addition to H_2 oxidative addition using BiPhePhos and XantPhos ligand. The details can be found in Appendix B.

3.2 From Electronic Energies to Molecular Properties

Potential energy surface (PES) is a key concept in computational chemistry. The energy of a system can be referred to as the function $E_{(R)}$, where R is a vector containing the coordinates of all atomic nuclei of the system, and E is the energy of the system that can be calculated by solving the Schrödinger equation (See section 3.1).

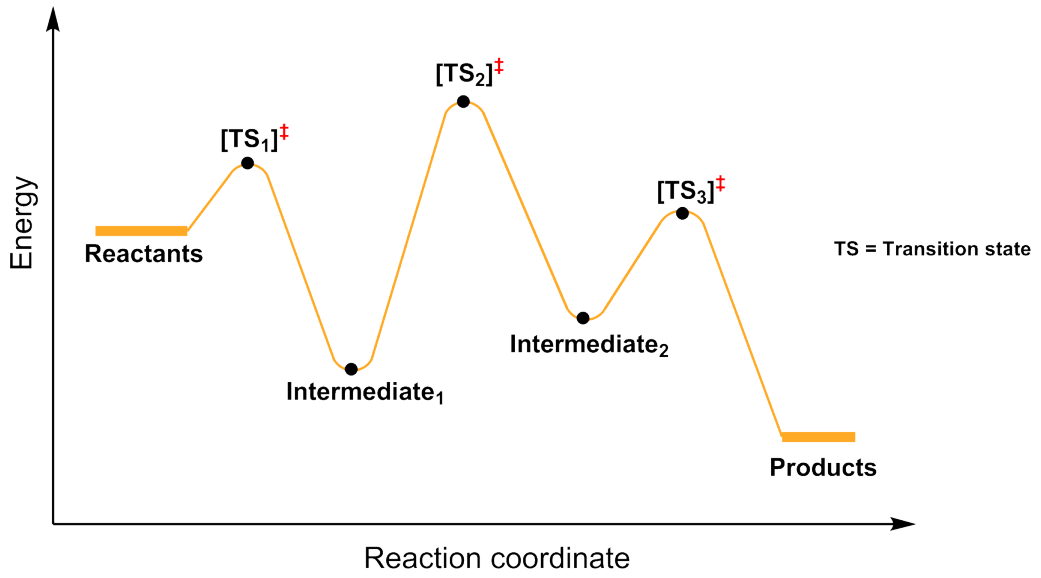

Fig. 3.2.: A 2-dimensional view of a potential energy surface (PES).

In Figure 3.2, the low energy 'wells' correspond to stable species (energy minima) such as reactants, intermediates and products. These species can persist for longer periods of time and, depending on their stability, can also be isolated and characterized. The high energy points 'peaks' are the transition states, critical energy points that must be passed through when the reactants convert to the intermediates and/or products. Mathematically, on PES, for wells (intermediates), the first derivatives of energy corresponding to the reaction coordinates is zero.

$$\frac{\partial E}{\partial R} = 0 \tag{3.30}$$

Any change in the coordinates of the reactants will result in an increase in energy, however for the conversion of the reactants into the products, they have to overcome an energy barrier 'peak' i.e. transition state. To differentiate between a minima and

a transition state, the second derivative of energy must be calculated (eq. 3.31 & 3.32).

$$\frac{\partial^2 E}{\partial R^2} > 0 \qquad \forall\ R\ \ (correspond\ to\ a\ minima) \tag{3.31}$$

$$\frac{\partial^2 E}{\partial R^2} > 0 \quad \forall R\ except\ reaction\ coordinate\ \ \frac{\partial^2 E}{\partial R^2} < 0\ \ (transition\ state) \tag{3.32}$$

The second derivative of energy is also known as Hessian matrix, which differentiates between the minima (wells) and transition states (peaks).

When searching for an energy minimum, the goal is to find the atomic structure with minimum potential energy, starting from a given initial configuration. In the most straightforward way, this can be done by following the energy gradient in every coordinate direction, and when the norm of the force components is below a fixed threshold, the structure is considered relaxed and be referred to an optimum (minimum). Though it sounds rather simple, the challenge is determining in which direction to search the minima and reach convergence within a reasonable amount of time.

There are a number of optimization methods available (for details please refer to any computational chemistry textbook)[119, 134, 150], a commonly used way is find an energy minima is through steepest decent (SD) method [151]. SD follows the direction in which the forces decrease the fastest, using a step size proportional to the slope of the potential energy surface. Adding a memory of previous search direction to the method results in what is called the conjugate gradient method [152].

The second derivative of energy (Hessian) can also be included in the optimization via Newton method, thus accelerating the convergence of the optimization. However, the Hessian is, for many systems, prohibitively expensive to calculate. An excellent compromise in practice is to begin with an approximate Hessian matrix, and update it using gradient and displacement information generated and updated after each optimization cycle (quasi-Newton-Raphson method). In a transition state search, the algorithm tries to maximize the energy along a certain negative eigenvector of the Hessian matrix while minimizing the energy along all other eigenvectors which results in one negative frequency along the reaction coordinate. Thus, a good initial guess for the transition search can make the transition state search significantly faster. The procedure used is called TRIM which stands for Trust Radius Image Minimization [153].

Upon adding the thermodynamic correcation to each energy point on the PES, Gibbs energy profile reaction under investigation is generated (see below).

The Gibbs energy profile of a chemical reaction provides important information about the stability (thermodynamics), and reactivity (kinetics) of molecules generated along the recation pathway. In addition, the effects of reaction parameters such as temperature, pressure and solvent can also be calculated from PES.

3.2.1 Molecular Vibrations

The vibrations are the oscillations around the equilibrium structure which are found by calculation of the Hessian matrix. After taking atomic masses into account, diagonalization of the Hessian matrix results in a set of eigenvectors and eigenvalues. Once the Hessian matrix is diagonalized, the eigenvectors represent the normal modes of vibration and the corresponding eigenvalues measure the stiffness of the potential energy surface along the the corresponding eigenvector. The vibrational frequencies are then calculated by taking the square root of the eigenvalues and multiplying by a conversion factor. A non-linear molecule with N number of atoms has $3N$ degrees of freedom corresponding to transitional, rotational and vibrational motions. $3N-6$ of these are modes of vibration, with 6 degrees of freedom removed due to the transitional and rotational motions. A linear molecule such as H_2, O_2 and CO_2 has $3N-5$ degrees of freedom since rotation along the axis of the molecule has an infinite symmetry number.

For a transition state, one of the eigenvalues will be negative (leading to an imaginary frequency), with the eigenvector corresponding to the reaction coordinate leading away from the transition state structure. However, all minima on the PES have only positive eigenvalues, thus the number of negative eigenvalues can differentiate between a transition state and a minimum.

3.2.2 Thermodynamic Properties

Solution of the electronic Schrödinger equation within the Born-Oppenheimer approximation yields the ground state energy of an atom or a molecule at 0 K. This means, that resulting energy corresponds to a hypothetical, non-vibrating molecule where, atomic nuclei are stationary, with the electrons revolving about them. Experimental measurements are performed on molecules at finite temperature and pressure where, molecules are free to move. To compare the theoretical and experimental results it is necessary to introduce appropriate corrections to allow for these motions. Even at 0 K, atoms within a molecule are always vibrating and the enrgy

attributed to this motion i.e., zero point vibrational energy (ZPVE) is tied up in molcular vibrations. ZPVE can be estimated from the vibrational frequencies generated after calculating the Hessian matrix within the harmonic-oscillator approximation (eq. 3.33).

$$ZPVE = \sum_{i}^{modes} \frac{1}{2} h\omega_i \tag{3.33}$$

where, h is the Planks constant and ω is the vibrational frequency. The ZPVE must be added to quantum mechanical energy to obtain the energy of molecule corresponding to absolute zero temperature, $T = 0\ K$.

To estimate thermodynamic properties such as enthalpy (H), entropy (S), heat capacity (c_p) and Gibbs free energy (G) of a molecular structure at reaction conditions, the molecular partition function must be estimated. The partition function Q enables the estimation of the energetic corrections due to molecular translation (i.e., motion through space), rotation, vibration, and electronic excitation at desired reaction conditions (eq. 3.34).

$$Q(N, V, T) = \sum_{i} e^{\frac{-E_i(N,V)}{k_B T}} \tag{3.34}$$

where, V is the volume, T is temperature, N is the number of particles, i runs over all possible energy states of the system having energy E, and k_B is Boltzmann's constant ($1.3806 \times 10^{-23} JK^{-1}$).

The partition function is calculated using the following assumptions. First, we assume that the molecules do not interact (system is an ideal gas), thus the partition function Q can be rewritten as;

$$Q(N,\ V,\ T)\ =\ \frac{[q(V,\ T)]^N}{N!} \tag{3.35}$$

where, $1/N!$ is deriven from the quantum mechanical indistinguishability of the particles and due to the ideal gas assumption PV in eq 3.43 can be replaced with RT, where R is the universal gas constant ($8.314\ J\ mol^{-1}\ K^{-1}$). Second, we consider that the molecular energy E_i can be expressed as the separable sum of electronic ($elec$), transitional ($trans$), rotational (rot) and vibrational (vib) terms, equation 3.36.

$$E_i \approx E_{i,trans} + E_{i,rot} + E_{i,vib} + E_{i,elec} \tag{3.36}$$

thus, the partition function can be written as:

$$q(V,\ T)\ =\ q_{elec}(T) q_{trans}(V,\ T) q_{rot}(T) q_{vib}(T) \tag{3.37}$$

where,

$$q_{elec} = e^{-E_{elec}/k_BT} \tag{3.38}$$

$$q_{trans}(V,\ T) = \left(\frac{2\pi M k_B T}{h^2}\right)^{\frac{3}{2}} V \tag{3.39}$$

$$q_{rot}(T) = \frac{\sqrt{\pi I_A I_B I_C}}{\sigma}\left(\frac{8\pi^2 k_B T}{h^2}\right)^{\frac{3}{2}} \tag{3.40}$$

$$q_{vib}(T) = \prod_{i=1}^{3N-6}\left(\frac{1}{1-e^{\frac{-h\omega_i}{k_BT}}}\right) \tag{3.41}$$

where, E_{elec} is the electronic energy, M is molecular weight and h refers to Planck's constant (6.6261$\times\ 10^{-34}$ J s). In eq. 3.40, I is the moment of inertia and σ is the symmetry number. $h\omega$ in eq. 3.41 is vibrational energy term within classic harmonic oscillator approximation. For more information the reader is referred to the book of C J Cramer [134].

Once the molecular partition function Q is obtained, the internal energy U, enthalpy, entropy and Gibbs free energy can be calculated by

$$U = k_B T^2 \left(\frac{\partial\ ln\ Q}{\partial T}\right)_{N,V} \tag{3.42}$$

$$H = U + PV \tag{3.43}$$

$$S = k_B\ ln\ Q + k_B T\left(\frac{\partial\ ln\ Q}{\partial T}\right) \tag{3.44}$$

$$G = H - TS \tag{3.45}$$

3.2.3 Free Energy of Solvation

The free energy of solvation ΔG_{solv} represents a very important property for the thermodynamic description of a reaction carried out in solution. Strong intermolecular interactions between solvents/reactants or solvents/catalysts may lead to an increase/decrease in product yields or side product distributions. For a complex multi-step reaction, free energy of reaction (thermodynamics) and activation energy barriers for the transition states (kinetics) in solution can be calculated using a cyclic approach.

For the thermodynamics (ΔG) and kinetics ($\Delta G^{\ddagger}$) of the reaction in solution, reactants A and B are (de)solvated from an solution to the gas phase, and subsequently, the transition state [A-B]‡ and the product C are solvated to yield not only the

standard Gibbs energy in solution ($\Delta G_{solu.}$) but also the activation energy barriers of the transition state ($\Delta G_{solu.}^{\ddagger}$) (Figure 3.3).

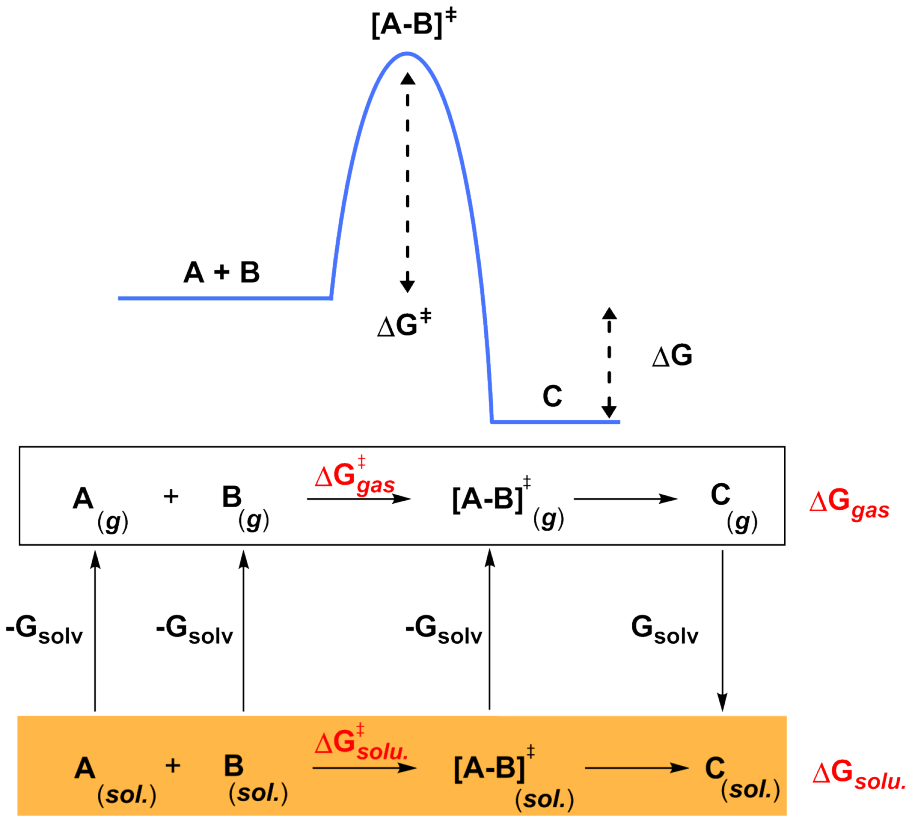

Fig. 3.3.: Estimation of Gibbs free energy of reaction and activation energies of transition states in solution as a circular process involving desolvation and solvation of the reaction species as well as the chemical reaction in the gas phase.

From the theoretical point of view, several approaches have been developed to predict ΔG_{solv} (Figure 3.4). Quite generally, the theories concerning the solvation process can be classified according to an explicit or an implicit treatment of the solvent molecules. In implicit treatment of the solvation process, the solvent is represented by a continuum in which the solute is embedded, whereas the explicit description of the solvation considers a large number of solvent molecules. A hybrid cluster-continuum solvent description only considers the first solvation shell explicitly and the bulk solvent are estimated via continuum solvent models. A brief overview of different solvent models will be discussed in the remainder of this section.

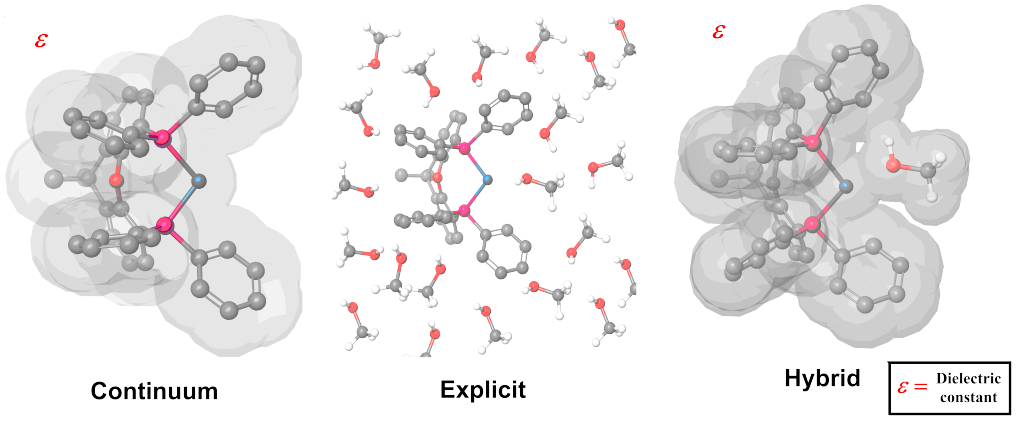

Fig. 3.4.: Different levels of computational solvent representations. Left: continuum solvent model with a specific dielectric constant ϵ; center: the explicit atomistic picture of all solute and solvent molecules; right: mixed cluster-continuum model in which the solute (here a catalyst) and directly interacting solvent molecules are embedded in a dielectric medium. Obtained from [154].

Solvation Models

The simplest and computationally most efficient one is the description of solvent effects by a dielectric continuum (Figure 3.4, left). The polarization of the solute by surrounding solvent molecules is described by an unspecific term depending on the dielectric constant (ϵ). The solvent continuum represents a statistical average over all solvent degrees of freedom at thermal equilibrium. Continuum solvent models represent an appealing approach for the calculation of Gibbs energies of solvation, in particular of relative effects upon changes of solvent or temperature. The dielectric continuum representation is a computationally affordable approach to incorporate polarity effects of the solvent into the intermediates and transition states located on the potential energy surface (PES).

One of the simplest approach for the estimation of free energy of solvation, in implicit regime, is the so-called Born model [155] which applies to spherical solutes with charge q placed at the center of the sphere. It can be calculated via integrating Poisson equation of classical electrostatics, which itself works under the assumption that the solvent cage polarizes linearly in response to the charge on the solute.

$$\Delta G_{solv} = -\frac{1}{2}\left(1-\frac{1}{\epsilon_r}\right)\frac{1}{4\pi\epsilon_0}\times\frac{q^2}{r} \tag{3.46}$$

where, ϵ_0 and ϵ_r are the vacuum and relative permittivity of the solvent respectively and r is the radius of the solvent sphere or cavity created by the solute.

The shape of the cavity used in continuum solvent models has been a subject of debate, as molecular shapes can be rather complex, with multiple partial positive and partial negative charges distributed around the surface of the cavity, thereby a spherical description of the cavities is inadequate. In addition, the choice of cavity may have a significant effect on the solvation energy. Finally, non-electrostatic interactions between solute and solvent, such as dispersion must also be accounted for.

Miertuš et al. [156], have implemented multiple spheres centered at the nuclei of atoms composing the solute molecule, dependent on the atomic radii also known as van der Waals radii, in continuum solvation models. Another approach conceptualized by Lee & Richards [157] and Hermann [158], independently, is the description of cavity via solvent-accessible surface area (SASA). Where SASA is the area traced out by mapping the surface of the solute molecule. There exist some other approaches for cavity generation, for example, Cramer & Truhlar use the radius of half effective width of the first solvation shell [159] and the original conductor like screening model (COSMO) use the minimum radius (radius of hydrogen) found in solvent molecules [160].

A shortcoming of implicit solvent models such as COSMO is that they are not able to distinguish between different solvents with same dielectric constants. To overcome this issue, there exists a modified version named COSMO-RS, where RS stands for realistic solvation that uses charge density (σ) rather than dielectric constant and, allows the estimation of the free energy of solvation not only for solvents with same dielectric constant but also for solvent mixtures [161]. In addition it also includes the terms for the treatment of specific molecular interactions between solute and solvent molecules such as hydrogen bonding. The performance of COSMO-RS is superior to the dielectric solvent models such as COSMO [162].

In continuum solvation models for example, the solute-solvent boundary is not unique, furthermore, solvent molecules in the first coordination shell that may account for strong and specific solute-solvent interactions are not considered. In addition, continuum behavior is not observed at small distances from the solute molecule. All of these shortcomings can be resolved by using a cluster-continuum solvation model [163]. Using cluster-continuum model, the short range solute-solvent interactions (first solvation shell) are treated at the same QM level as the solute, while bulk solvent effects are estimated by using continuum solvation schemes. However, estimation of the number of explicit solvent molecules required to represent the first solvation shell can be expensive in terms of computationals costs.

Explicit treatment of the solvation, on the other hand, is rarely used at quantum mechanical level, due to high complexity and computational costs. Quantum mechanical methods, such as DFT, are generally not recommended for a system larger than 200 atoms [164], which makes the explicit treatment of a large number of solvent surrounding the solute out of scope. Explicit solvent treatment is normally used for biomolecular systems where the solvent of interest is generally water [165, 166], and solvent molecules are described via molecular mechanics, while the solute is treated at quantum mechanical level (QM/MM).

3.3 Thermodynamic and Kinetic Modeling

For chemical reactions, ΔG_r is the Gibbs free energy difference between the reactant and products allows us to know the nature of the chemical reaction i.e. exo- or endothermic and to calculate its chemical equilibrium constant. Hence, for a chemical reaction under given experimental conditions and with a known initial composition of the components of the reaction mixture, ΔG_r enable the calculation of the thermodynamic equilibrium constant K_{eq}. However, ΔG_r does not say anything concerning the rate at which a reaction proceeds towards equilibrium, nor the pathway that is followed, leading to that final products. On the kinetics side, the objective is to calculate the rate of the reaction. Ideally, for complex multi-step reactions, the rate equations for all elementary reactions in the reaction mechanism are included. It should be noted that such a model usually requires quite a lot of rate constants, for both the forward and reverse reactions corresponding to many different transition states. However, in experimental applications, either empirical impressions such as power laws are often fitted to a set of experimental data without accounting for the reaction mechanism or simplified reaction mechanisms are considered thus reducing the complexity of the system and costs related to kinetic parameter estimation [167]. Using quantum chemical methods, the activation energies of all elementary reactions involved within a reaction mechanism can be calculated. Using reaction rate constants from the quantum chemical calculations in combination with the experiments accurate kinetic models can be generated with reduced computational costs. The most commonly used theory for the calculation of kinetic rate constants is the transition-state theory (TST). TST was first introduced by Henry Eyring in 1935 [168]. The standard free energy difference between the reactants and the transition state (peak: see section 3.2), written as $\Delta G^{\ddagger}$ (free energy of activation), provides an estimate of the rate constant for the reaction using TST.

The theory assumes that the concentration of the species at the transition state is in equilibrium with the reactants and can mathematically written as:

$$k = \frac{k_B T}{h} e^{\frac{-\Delta G^{\ddagger}}{RT}} \tag{3.47}$$

In this equation, k_B is Boltzmann's constant, T is temperature, h is Planck's constant, $\Delta G^{\ddagger}$ is the activation energy and R is the universal gas constant. Another important factor to be included in the kinetic modeling of homogeneously catalyzed reactions that are barrier-less. A barrier-less reaction is an elementary reaction step where, for example species A and B can react to form C without needing to cross a potential energy barrier. They may not be critical when evaluating the viability of a reaction mechanism, as they correspond to fast steps, but a rate constant value is nevertheless required to build a kinetic model, and such steps can affect the overall predicted rate of turnover [169]. They occur for a wide range of bimolecular reaction steps common in catalysis, such as addition of a ligand to a coordinatively unsaturated metal center, or addition of some radicals to other species.

Scanning of the potential energy surface often shows that in such cases there is no activation energy barrier. In the absence of an energy peak on the potential energy surface in vacuum (or in solvent), it is not possible to estimate a kinetic rate constant based on TST.

A common way to estimate the kinetic rate constants for such reactions is by assuming that such steps occur in the diffusion-limited regime. On the basis of a combination of theories of diffusion and of collisions [170], a simple expression for the rate constant can then be obtained with as only required input the solvent viscosity η and the temperature T ; $k = 8k_B T/3\eta$. With typical solvent viscosities near room temperature, this corresponds to the magnitude of the rate constant that would arise from the Eyring equation with a Gibbs energy barrier of roughly almost 17 kJ/mol [171].

4

Hydroformylation of Long-chain Olefins: Mechanism, Solvent Effects, Catalyst's Selectivity, and Degradation

Kinetic models are essential for rational design of chemical reactors. Complex multi-step reactions, when elementary reactions are taken into account constitute a highly complex mathematical problem, with a large number of equilibrium and rate constants corresponding to forward and backward reactions. Quantum chemistry methods, such as Density Functional Theory (DFT), enable the calculation of these kinetic rate and equilibrium constants and the identification of the rate-determining step which in return help reduce the complexity of kinetic models.

In the following chapter DFT is used to investigate the Rh(I)-catalyzed hydroformylation (Hyfo) of 1-decene as a representative of long-chain olefins from renewable feedstocks. Hydroformylation, also designated as oxo-synthesis, is a reaction where alkenes react with synthesis gas (CO/H_2) in the presence of a transition metal catalyst to form terminal and branched aldehydes. Figure 4.1 illustrates the formation of aldehydes via hydroformylation of terminal olefins with possible side products.

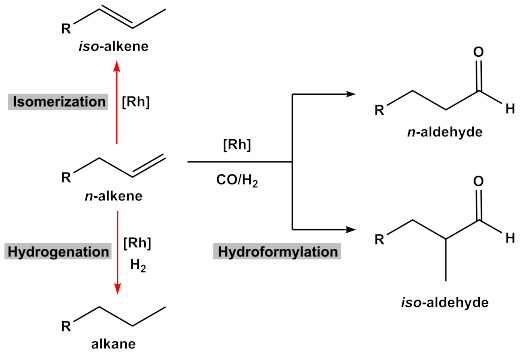

Fig. 4.1.: Schematic representation of the hydroformylation reaction plus possible side reactions. The main reaction gives the desired *n*-aldehyde and undesired *iso*-aldehyde products. Side reactions (isomerization and hydrogenation) lead to the formation of internal alkenes and alkanes, respectively.

It should be noted that the author of this thesis published significant parts of the following chapter in:

- Jameel F., and Stein M., Solvent effects in hydroformylation of long-chain olefins, Molecular Catalysis 503, 2021, 111429-111441 [172].
- Gerlach M., Jameel F., Seidel-Morgenstern, A., Stein M. & Hamel C., Operando characterization of rhodium catalyst degradation in hydroformylation, Catalyst Science and Technology, 13, 2023, 1788-1801 [173].
- Gerlach, M., Kirschtowski, S., Jameel, F., Huxoll, F., Stein, M., Sadowski, G., Seidel-Morgenstern, A. & Hamel, C. Kinetic Modeling of Complex Catalytic Reactions in Multi-phase Systems. In Kraume, M., Enders, S., Drews, A., Schomäcker, R., Engell, S. & Sundmacher, K. (Ed.), Integrated Chemical Processes in Liquid Multiphase Systems. From Chemical Reaction to Process Design and Operation: De Gruyter, Berlin, 2022, 55-188 [174].

In the first part of this chapter, the reaction mechanism of Hyfo, using rhodium(I) central metal ligated to an electron withdrawing BiPhePhos (**BPP**) ligand as a catalyst is investigated. At first, activation of the catalyst via CO dissociation from the pre-catalyst in solution (Section 4.1.1) is discussed. Then, the free energy profile leading to the desired linear aldehydes is presented after optimizing all intermediates and transitions states along the linear pathway without the consideration of solvent effects. Based on the activation energy barriers of the transition states the rate-determining step (RDS) is identified. Subsequently, side reactions leading to internal olefins and alkanes (isomerization and hydrogenation) are resolved and from the activation energy difference between the selectivity determining transition states the catalyst's selectivity towards the desired product is calculated (Section 4.2.1).

During the mechanistic investigations for a homogeneously catalyzed reaction, the effects of substrate and solvent impurities on the catalyst system are often overlooked. Catalyst degradation that can be caused by impurities in the feedstock affects key performance parameters such as catalyst's selectivity, conversion and product yield. One such example of feedstock impurity that may cause deactivation of the catalyst is exposure of the long-chain olefins to the oxygen that to leads an auto-oxidation of the olefins resulting in the formation of peroxides [175–177], thus negatively affect the regioselectivity of the Rh/BPP-catalyzed hydroformylation of 1-dodecene [178]. In hydroformylation on industrial scale, for example, rigorous exclusion of oxygen is difficult to achieve. Therefore, small amounts of peroxides will always be present in the olefin substrate that can potentially deactivate the catalyst. To revive the catalytic activity after its deactivation, the first step is the characterization of

deactivated catalyst species. The results regarding the effects of substrate impurities on the catalyst's stability are presented in Section 4.3.

Finally, the solvent effects on each elementary step are estimated resulting in the kinetic rate constant calculations in solution, which later can be used for reducing the complexity (via reduction in number of unknown parameters) of the kinetic models (Section 3.3).

Within InPROMPT, the hydroformylation experiments were conducted in a temperature-controlled switchable solvent system called thermomorphic multi-component solvent system (TMS) that enables the reaction to proceed without any mass transfer limitation at process conditions, and allows the post-reaction separation of the product from the catalyst via changing the temperature of the reaction mixture [179]. N,N-Dimethylformamide (DMF) was proposed initially as a promising solvent candidate by chemical intuition and was later identified as one of the best performing solvents from a thermodynamic point of view [7, 180]. However, DMF is a toxic substance, and is included in the REACH list of components of very high concern. Thus, there is a need to find alternative solvents in order to replace it [181]. The question, if toxic DMF be replaced with less ecologically harmful solvent without compromising catalytic activity, is addressed in the last part of this chapter (Section 4.3). This was achieved by calculating the effect of solvent on the rate-determining step (RDS) where the reduction in the activation barrier of RDS due to the solvent and explicit catalyst-solvent interactions was chosen as selection criteria.

4.1 Resolution of the Reaction Mechanism

Catalytic cycles that consist of several elementary steps, such as hydroformylation, lead to multi-parameter kinetic models when all intermediates are taken into account [182]. These parameters are sometimes not available experimentally, but can be obtained from quantum chemical calculations. The mechanism of rhodium catalyzed hydroformylation was first postulated by Even et al. [183] and later extended by Kiedorf et al. [184] and Markert et al. [185] to include the side reaction such as double bond isomerization and hydrogenation and is shown in Figure 4.2. Here quantum chemical calculations are used to resolve the complete mechanism of hydroformylation of 1-decene is resolved in the presence of a (BiPhePhos)HRh(I)(CO) catalyst including side reactions to calculate the free energies of all intermediates formed (thermodynamics) and activation energies of all corresponding transition states (kinetics). These kinetic and thermodynamic parameters and their solvent

dependencies will assist in the development and simplification of the kinetic model for rhodium-catalyzed hydroformylation of long-chin olefins.

The resting state of the pre-catalyst **1*** is activated to form the active catalyst species **1** upon CO dissociation. Substrate coordination gives complex **2**, and subsequent hydride insertion results in the formation of Rh-alkyl species **3n** and **3b**, where **n** refers to pathway leading to linear aldehydes, and **b** leads to branched aldehydes. Later, CO is coordinated to the central metal atom, thus forming complex **4**. CO is then inserted into the metal-alkyl bond and the acyl complex **5** is generated. H_2 coordination (**6**) followed by its oxidative addition forms complex **7**, and finally, reductive product elimination recovers the active catalyst **1**.

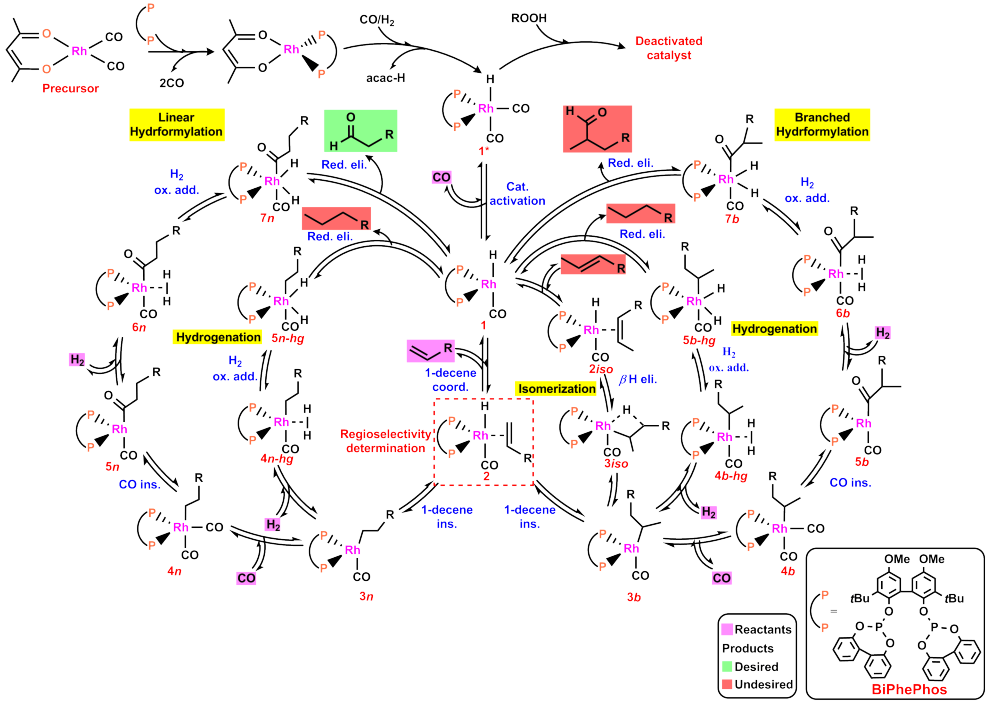

Fig. 4.2.: Catalytic cycle for the hydroformylation of olefins in the presence of bidentate diphosphite rhodium (I) catalyst. Isomerization and hydrogenation are included as side reactions.

4.1.1 Catalyst Activation

Pre-catalyst (or catalyst resting state) **1** can be prepared by mixing the catalyst precursor (acac)Rh(CO)$_2$ and biphephos (BPP) ligand in a DMF/dodecane solvent mixture in the presence of synthesis gas (CO/H_2) for 30 mins at 378 K [184].

The catalytic reaction starts with the generation of a 16-electron active catalyst species **1*** with a free coordination site at the equatorial position after dissociation of a CO from the trigonal-bipyramidal catalyst resting state **1** (See Figure 4.2). The yield of product is critically dependent on the concentration of the active catalyst species and thus, the chemical equilibrium between 1* and 1. The experimentally reported rate constant for CO dissociation from [$HRh(CO)_2$(thiaxantphos)] catalyst is 200 h^{-1}, that corresponds to a free energy of 84 kJ/mol for CO dissociation [186]. A kinetic model after parameter fitting, however, overestimates the thermodynamic equilibrium constant of K_{eq} = 5496.7 L mol^{-1} for catalyst activation, which corresponds to a Gibbs free energy of almost 22 kJ/mol for CO dissociation from the pre-catalyst **1*** leading to the active catalyst **1** in solution [187]. Landis et al. have reported CO dissociation to be a barrierless process with a Gibbs free energy for CO dissociation of 63 kJ/mol in the presence of a Rh-Xantphos catalyst using the B3LYP hybrid density functional [84]. Gellrich and co-workers have also investigated hydroformylation of small chain olefins using a simplified rhodium catalyst model system. They have reported a Gibbs free energy of 44 kJ/mol for CO dissociation from the catalyst resting state leading to an active Hyfo catalyst using CCSD(T) [82]. Hence, catalyst activation is extremely sensitive to both the ligand properties and the computational methods used to estimate them. Therefore, the computational method used in this study (PBE0-D3(BJ)) was selected after a detailed benchmark study consisting of a number of rhodium based catalytic reactions. During the benchmark study, the performance of different density functionals of GGA, meta-GGA, hybrid, double hybrid and semi-empirical (GFN2-xTB) methods was compared against the standard DLPNO-CCSD(T) method and as a result the best performing method was selected (For details, See Appendix B).

Figure 4.3 shows the optimized geometries estimated using PBE0-D3 functional for pre- and activated catalyst with the partial charges calculated using natural population analysis (NPA) on the phosphorus atoms from the bidentate ligand, transition metal, carbon atom in CO and H atom. Fourier-transform infrared (FTIR) studies only showed the formation of the Rh-hydridodicarbonyl complex **1*** where the bidentate ligand occupies the equatorial-equatorial positions plus one axial and one equatorial CO ligand.

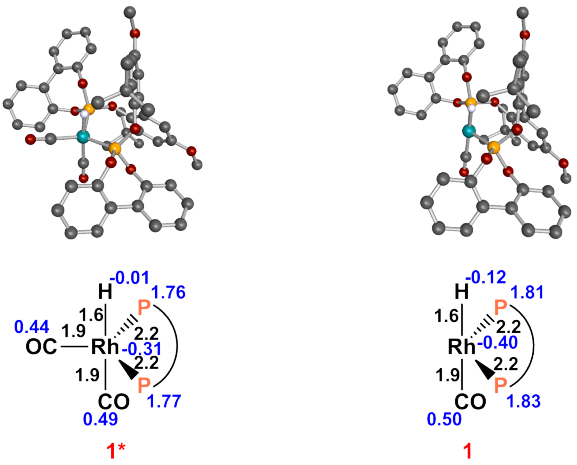

Fig. 4.3.: Activation of pre-catalyst 1* via CO dissociation. Hydrogen atoms from the ligand are omitted for clarity. Bond distances (black) are given in Angstroms. Natural Population Analysis (NPA) charges are given in blue. Obtained from [172].

Given the high dissociation energy, the concentration of the active catalyst species (Complex **1**) will be too low to be spectroscopically observable (of the order of K_{eq} = $2.5e^{-12}$ mol/l for Rh/BiPhePhos catalyst, obtained from $\Delta G_{CO\ dissociation}$ = 84 kJ/mol using PBE0-D3). Recent *in-situ* FTIR studies of the Rh(BiPhePhos) system have shown that a large amount of the pre-catalyst **1*** is present throughout the entire reaction and the active catalyst species could not be detected in batch [80] and continuous experiments [188].

Solvents only affect the CO dissociation energies to a minor degree. The polarity of the solvent only has a marginal effect on the catalyst activation energy. The solvent used in this work for the estimation the solvent effects on all elementary step of the reaction cycle stems from hydroformylation experiments using DMF/dodecane solvent mixture that constituents a Thermomorphic Multiphase Solvent (TMS) system [189]. The energy of CO dissociation when BiPhePhos (BPP) is used as catalytic ligand, is slightly lower in polar DMF than in non-polar dodecane (see Table 4.1).

Tab. 4.1.: Gibbs free energies of CO dissociation from the catalyst resting state in kJ/mol.

		DMF/dodecane composition				
	Gas phase	**(100:0)**	**(70:30)**	**(50:50)**	**(30:70)**	**(0:100)**
$\Delta G_{CO\ diss.}$	84.2	83.7	83.7	84.1	84.6	85.3

4.1.2 Formation of the Desired Linear Aldehydes

After CO dissociation, the substrate 1-decene coordinates at the free coordination site and the π-complex **2** is formed. In the newly formed complex **2**, both the ligand and the double bond of 1-decene lie in the equatorial plane and the hydride and the CO are in axial positions. When 1-decene enters the coordination sphere of the catalytic center, the P-Rh-P bite angle is reduced from 136° in **1** to 116° in complex **2** for BiPhePhos ligand due to the steric hindrance of the ligand. However, upon substrate coordination the metal-ligand (Rh-P) bond length remains the same (See Figure 4.4). Upon the double bond coordination, the electron density shifts from rhodium to the coordinated double bond, the partial negative atomic charges on the alpha and beta carbon atoms are increased and the C=C double bond elongates by 0.1 Å (See Figure 4.4). The coordination of 1-decene to the (BPP)RhH-(CO) catalyst is exergonic by 45.6 kJ/mol.

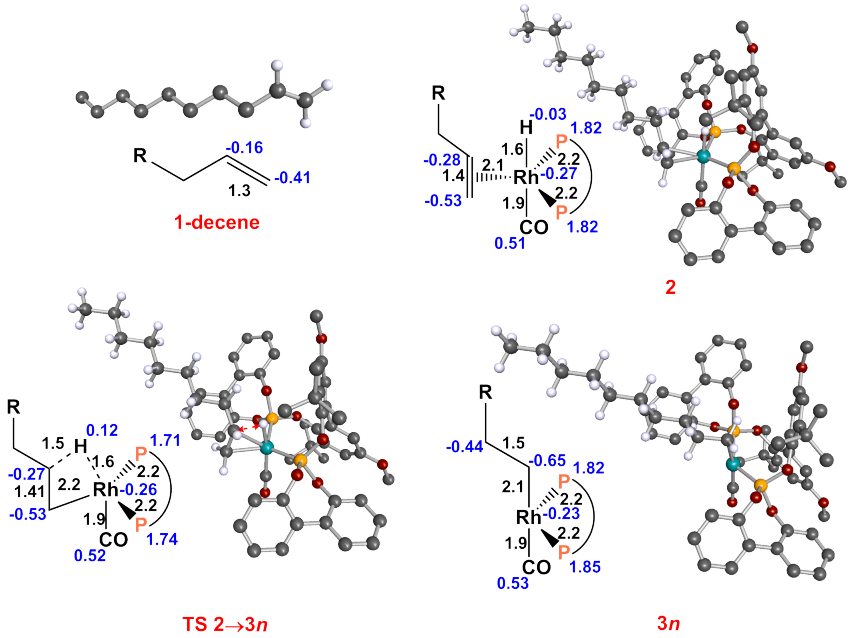

Fig. 4.4.: Ligand effects on the olefin coordination **2** and its subsequent insertion into the Rh(I)-H bond (**TS 2→3n**). Hydrogen atoms from ligand are omitted for clarity. Bond distances (black) are given in Angstroms. NPA charges are given in blue. Obtained from [172].

The subsequent hydride insertion into the double bond is the branching point of the reaction cycle: when the hydride binds to C_β, the linear alkyl complex ***3n*** is obtained. When approaching C_α, the branched alkyl ***3b*** is generated. In either case, a substrate rearrangement of the double bond into an orientation parallel to the H-Rh bond is a prerequisite for the migratory hydride insertion. The located transition state has an

imaginary frequency of –584 cm^{-1}, that corresponds to a concerted motion of Rh-H bond breakage and formation of the H-C_β bond. The calculated activation energy is 45 kJ/mol in the gas phase for (BPP)RhH-(CO) catalyst, which agrees well with the previously reported activation energy of 51 kJ/mol at the CCSD(T) level of theory [82].

For (BPP)RhH-(CO) catalyst the calculated Gibbs free energy of the formation of **3n** from **2** is endothermic by 13 kJ/mol and in agreement with CCSD(T) results of 10 kJ/mol. Following the linear pathway, the Rh-alkyl ***3n*** complex then interacts with carbon monoxide from syngas by forming a trigonal-bipyramidal complex ***4n***.

The newly coordinated CO occupies an equatorial position with the long alkyl chain in an axial position. The Gibbs free energy of equatorial CO binding to the (BPP)-Rh-alkyl **3n** complex is –41.7 kJ/mol. To accommodate the new coordinating CO the P-Rh-P bite angle is reduced from 137° to 118° for BPP catalyst (Figure 4.5).

CO insertion into to the alkyl chain (TS ***4n***→***5n***) results in the formation of an acyl complex ***5n*** that will eventually lead to the desired aldehyde product. The intramolecular CO insertion proceeds via a three-center transition state (**4n**→**5n**) with an activation energy of 29 kJ/mol, in which the Rh-CO bond is partially formed and the Rh-alkyl bond is partially broken, producing the four-coordinate Rh-acyl intermediate **5n** (Figure 4.5), that is 7 kJ/mol more stable than **4n**.

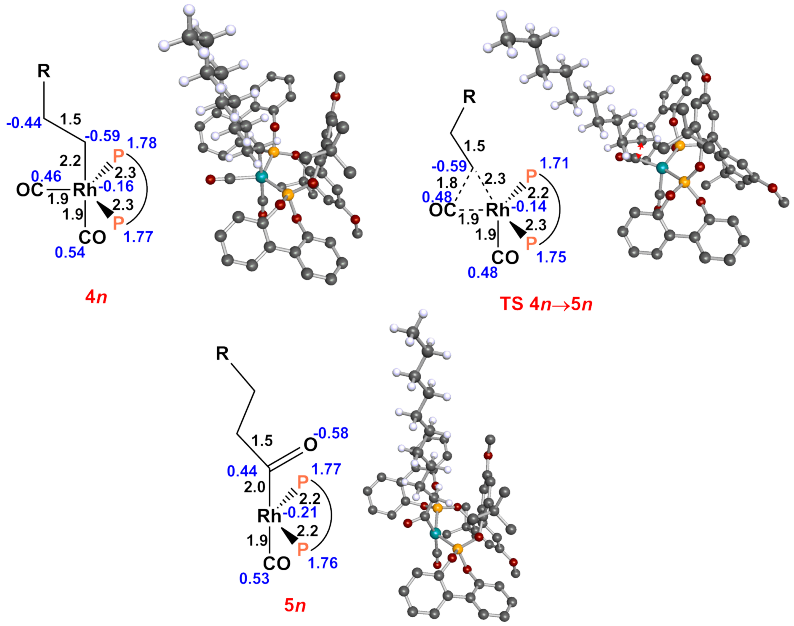

Fig. 4.5.: CO coordination (**4n**) and intramolecular insertion of CO (**4n**→**5n**) to give the undecyl Rh(I)Biphephos complex **5n**. Hydrogen atoms from ligand are omitted for clarity. Bond distances (black) are given in Angstroms. NPA charges are given in blue. Obtained from [172].

Dihydrogen coordinates to **5n** and thereby generates **6n**, an η^2-H_2 adduct. The H_2 approaches the rhodium atom with the H-H bond perpendicular to the Rh-acyl bond. The dihydrogen (H-H) bond slightly elongates to from 0.75 Å to 0.87 Å when coordinated to the Rh center in comparison to the free H_2 molecule. The CO and acyl ligands form a bond angle of 176° in complex **6n**. H_2 coordination to the acyl-complex is endothermic (ΔG =27 kJ/mol) in the gas phase. In the optimized transition state, the H-H distance increases by 0.33 Å compared to the H_2 η^2-complex **6n** with 0.87 Å. The H_2 oxidative addition proceeds via a very small transition state with an activation barrier of only 1 kJ/mol (**6n**→**7n**), generating a six coordinate catalytic complex with both H atoms perpendicular to Rh-acyl bond (see Figure 4.6). In the octahedral complex **7n**, the H and the P atoms constitute the equatorial plane; CO and the acyl chain occupy the axial positions. The formation of **7n** from **6n** is exothermic by -25 kJ/mol in the gas phase.

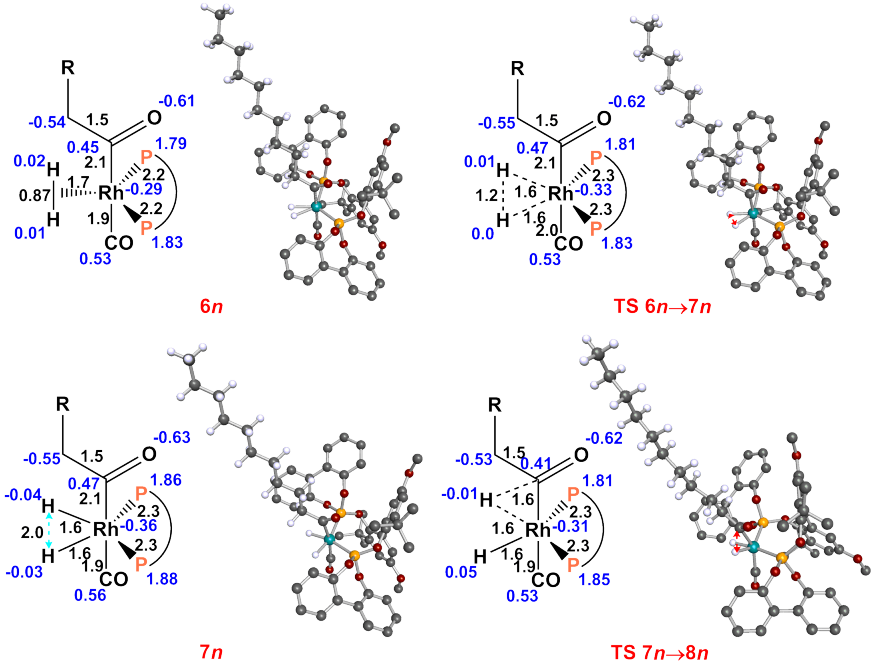

Fig. 4.6.: Optimized structure and atomic charges for complex 6n generated after H_2 coordination to rhodium-acyl species, H_2 oxidative addition transition state (6n→7n), (BPP)RhHH-acyl complex 7n and transition state (7n→8n) that corresponds to reductive elimination of an aldehyde product and simultaneous regeneration of the catalyst. Hydrogen atoms from ligand are omitted for clarity. Bond distances (black) are given in Angstroms. NPA charges are given in blue. Obtained from [172].

The final step of the hydroformylation cycle is the reductive elimination of aldehyde followed by the catalyst regeneration. The reductive elimination occurs through a three-center transition state (***7n***→***8n***), involving a concerted motion of Rh-C bond

breaking and C-H bond formation. In the transition state, the electron density is not evenly distributed between both hydrogen atoms: one H has a slight positive charge while the other is negatively charged and nucleophilic in character. At last, the recently formed aldehyde dissociates from the catalyst, thereby, regenerating the active catalyst. For the (BPP)RhH-(CO) catalyst, the calculated transition state barrier for the aldehyde reductive and release elimination is +50 kJ/mol. The Gibbs free energy of the reduction and elimination reaction from **7n** to **8n** is –10 kJ/mol.

Table 4.2 shows the activation energies of all calculated transition states along the linear hydroformylation pathway for BPP ligated rhodium catalyst in the absence of solvent. The activation energy barrier of hydride insertion is 45.2 kJ/mol. An activation energy of 29.4 KJ/mol is required for CO insertion into the Rh-alkyl bond when an electron withdrawing BPP ligand is used for hydroformylation.

Tab. 4.2.: Calculated Gibbs free energy barriers in gas phase for the transition states occurring along hydroformylation linear pathway. The Gibbs free energies are given in kJ/mol relative to the intermediate prior to the transition state. The thermodynamic correction were calculated at 378 K and 20 bar.

lig.	**Hydride ins.** **2 → 3n**	**CO ins.** **4n → 5n**	**H_2 ox. add.** **6n → 7n**	**Aldehyde red. eli.** **7n → prod.**
BPP	45.2	29.4	1	43.9

Hydrogen activation via oxidative addition on the metal center proceeds with an almost negligible activation energy barrier of 1 kJ/mol for BPP catalyst. The activation energy barriers for product reductive elimination with BPP catalysts are 43.9 kJ/mol, thus making the hydride insertion ($\Delta G^{\ddagger}$ = 45.2 kJ/mol), the slowest elementary step and therefore the rate-determining step (RDS) for hydroformylation of 1-decene.

4.2 Side Reactions

4.2.1 Origin of Catalytic Selectivity

Linear aldehydes are the prime products of interest in the industrial hydroformylation reaction. Thus, the catalyst more selective towards the desired products should be selected for the process design. The chemical and geometrical properties of the ligand has a significant effect on selectivity and kinetics of the hydroformylation. The steric hindrance employed by the rigid, bulky diphosphite ligand, for example, is responsible for its high selectivity towards the desired linear aldehydes (see Chapter

2.1). Following the substrate (olefin) coordination, hydride insertion into the C=C double bond is the branching point for the hydroformylation. For the terminal olefin (1-decene) Rh-H insertion into Rh-C_β bond leads to the formation of **3n**, and eventually to the linear product. Hydride attack to the C_α carbon gives the intermediate **3b** and finally the branched aldehyde (Figure 4.7).

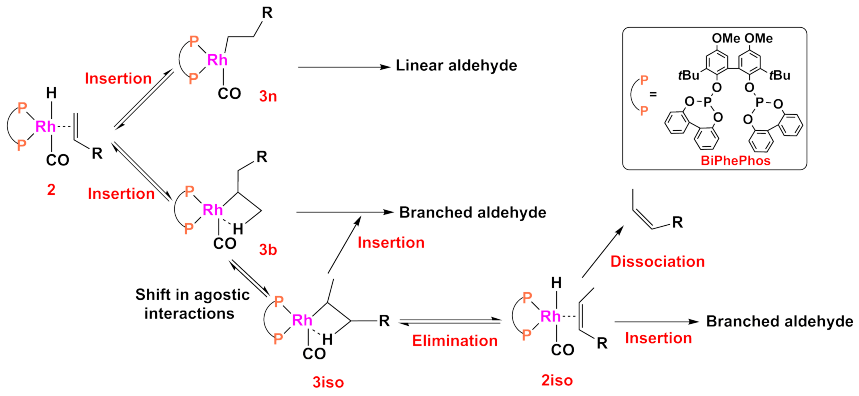

Fig. 4.7.: Olefin insertion from **2** is the branching point for the formation of linear (via **3n**) vs. branched (via **3b**) aldehydes.

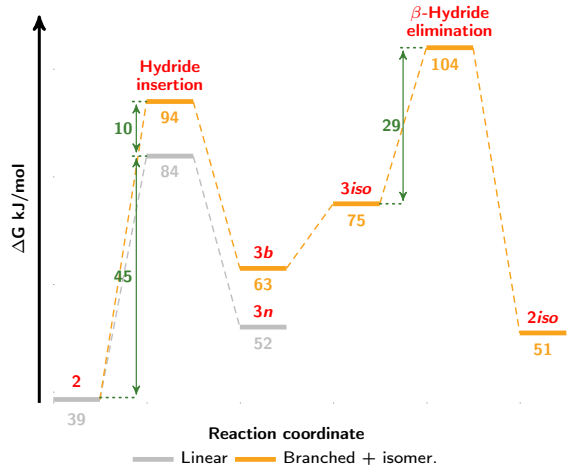

Fig. 4.8.: Relative Gibbs free energies in kJ/mol for the catalyst's selectivity towards the linear aldehydes and isomerization of 1-decene to internal olefins with BiPhePhos. All energies are relative to the catalyst resting state.

Figure 4.8 shows the Gibbs free energy profile for the formation of complex **3b** followed by the hydride insertion in to C_α in comparison to the free energy profile leading to the desired linear pathway. The formation of **3n** is both kinetically and thermodynamically favored over **3b**. The activation energy required for the formation of **3b** ($\Delta G^{\ddagger}_{2\rightarrow 3b}$ = 55 kJ/mol) is 10 kJ/mol higher than that for **3n** ($\Delta G^{\ddagger}_{2\rightarrow 3n}$ = 45 kJ/mol).

Assuming that olefin insertion can be described by first order reaction kinetics, equation 4.1 derived from the Arrhenius equation, can be used to calculate kinetic discrimination between two pathways i.e. catalytic selectivity.

$$S_{l/b} \approx \frac{k_n}{k_b} e^{-(\Delta\Delta G^{\ddagger})/RT} \tag{4.1}$$

where $S_{l/b}$ is the ratio between the reaction rate of two pathways and $\Delta\Delta G^{\ddagger}$ is the difference between the activation energies of the transition states leading to complexes **3n** and **3b**. For (BPP)RhH-(CO) catalyst, the kinetic discrimination by the transition state energy differences between linear and branched products leads to a selectivity of 96:4 at 378 K and 20 bar, which is in good agreement with the experimentally determined selectivity of 99:1 for the same catalyst system [187].

4.2.2 Double Bond Isomerization at the Catalyst

Complex **3b** does not only yield branched aldehydes but can also initiate the isomerization of the double bond (See Figure 4.7). The agostic interaction in complex **3b** between C_α, H and the Rh enables the formation of internal alkenes. Internalization of the double bond occurs via a C-C bond rotation to **3iso** and a "chain walking" mechanism that constitutes of a series of β-hydride eliminations to give **2iso** and further internalized double bond isomers [190]. The shift in the agostic interactions occurs as the C-C bond rotates while still attached to the catalyst forming complex **3iso**. Later β-H is eliminated from C_γ and then complex is **2iso** is obtained with a double bond between C_β and C_γ. In the absence of CO, this leads to a thermodynamic equilibrium distribution of internal olefins which can be well reproduced quantum chemically [190, 191]. The reverse, a tandem isomerization of internal olefins plus hydroformylation towards the linear aldehyde is also possible [187].

For (BPP)RhH-(CO) catalyst, this re-orientation ($\Delta G_{3b \rightarrow 3iso}$ = +12 kJ/mol) is thermodynamically not favored. However, the transition state barrier of +29 kJ/mol for subsequent β-H elimination is 26 kJ/mol lower than that olefin insertion leading to branched Rh-alkyl **3b** complex (See Figure 4.8). The low activation energies for olefin isomerization explains the swift isomerization of the olefin towards a chemical equilibrium concentration. The Gibbs free energy profiles show, that the formation of linear aldehyde (undecanal) is both kinetically and thermodynamically favored when (BPP)RhH-(CO) catalyst is used. The formation of side products, such as branched aldehydes or internal olefins, is suppressed by the electron withdrawing BiPhePhos bidentate ligand.

4.2.3 Alkane Formation

In addition to formation of branched aldehydes and isomerization of the substrate, hydrogenation of the metal-alkyl complex **3n** and **3b** is also a possible (See Figure 4.9). The Rh-alkyl intermediate species **3n** has a free binding site to which CO binds in the productive cycle, whereas H_2 coordination gives saturated alkanes.

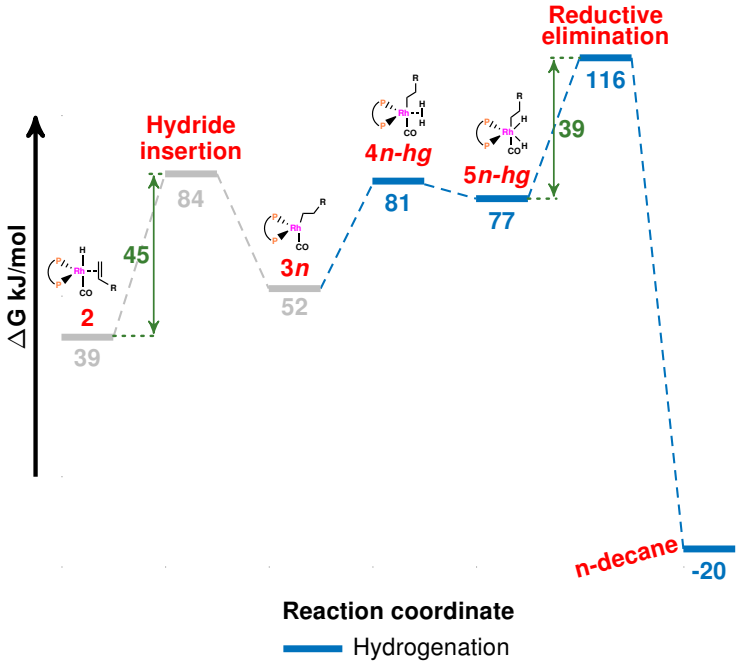

Fig. 4.9.: Relative Gibbs free energy differences in kJ/mol for the hydrogenation of 1-decene to n-decane with (BPP)RhH-(CO) catalyst. All energies are given relative to the catalyst's resting state.

Upon H_2 coordination to **3n**, a H_2·Rh-decyl complex **4n-hg** is formed. The recently coordinated H_2 then swiftly undergoes an oxidative addition and as a result BPP-Rh(III)HH(alkyl) complex **5n-hg** formed. H_2 binding to complex **3n**, however, is thermodynamically not favored ($\Delta G_{H_2\ binding}$ = 29 kJ/mol); see Figure 4.9). The formation of complex **5n-hg** is from **4n-hg** is thermodynamically feasible by -4 kJ/mol for BPP catalyst. Experimentally, there is always a fraction of saturated alkanes present. The activation energy relative to pre-catalyst **1*** for reductive elimination step of decane with 116 kJ/mol is almost 32 kJ/mol higher than the activation energy for hydroformylation of 1-decene in gas phase (84 kJ/mol).

In summary, after resolving the side reactions possibly occurring during hydroformylation using (BPP)RhH-(CO) catalyst, it showed its remarkable selectivity towards the desired linear aldehydes.

4.3 Catalyst Degradation

To investigate the effect of feed impurities on the kinetics of rhodium catalyzed hydroformylation, experiments were carried out using 1-dodecene as long-chain olefins substrate with the BiPhePhos catalyst in DMF/decane TMS solvent mixture and *tert*-Butyl hydroperoxide *t*BuOOH as a model substrate impurity by Martin Gerlach at OVGU Magdeburg [173]. To monitor catalyst degradation, operando FTIR spectroscopy was applied. For carbonyl containing Rh catalysts, the C=O stretching frequencies are of crucial importance to deduce the structural information of catalytic complexes produced during hydroformylation [188, 192]. The degradation of the catalyst (metal/ligand complex) can cause a reduction in intensity of Rh–CO vibrational bands. In addition, the formation of new Rh–CO vibrational bands may occur due to degradation reactions and the formation of new unknown complexes. A significant loss in catalytic selectivity was observed in the presence of hydroperoxide impurities during experiments. A time-dependent difference in spectral data indicated changes in the catalyst species. However, the new spectral peaks appearing due to changes in catalytic species could not be unequivocally assigned to individual compounds. It was shown that quantum chemical (DFT) calculation can accurately describe the IR spectra of these metal-carbonyl complexes [192].

To identify these newly formed deactivated rhodium carbonyl (Rh–CO) species observed during the experiments, a comparison of experimental and calculated spectra of possible deactivated Rh-CO complexes is discussed in the remainder of this section. Figure 4.10 reveals the calculated IR spectra for hydroformylation Rh(I) "catalyst resting state" (BPP)RhH$(CO)_2$ (**1***) (see Figure 4.2) and candidates "Catalyst deactivated" for the degraded species (**II–VII**).

When the BiPhePhos ligand is introduced to the pre-cursor Rh(acac)$(CO)_2$ in the presence of syngas (CO/H_2), the trigonal bipyramidal rhodium hydridodicarbonyl (**1***) is formed with the bidentate ligand and one CO occupying equatorial positions while the second CO and the hydride are in axial positions. For catalyst resting state (**1***), in accordance with the previous studies,[178, 192] the peak at 1968 cm^{-1} corresponds to the Rh–H bond stretch. The peak at 2001 cm^{-1} refers to the equatorial CO, and the peak at 2072 cm^{-1} corresponds to the axial CO vibration.

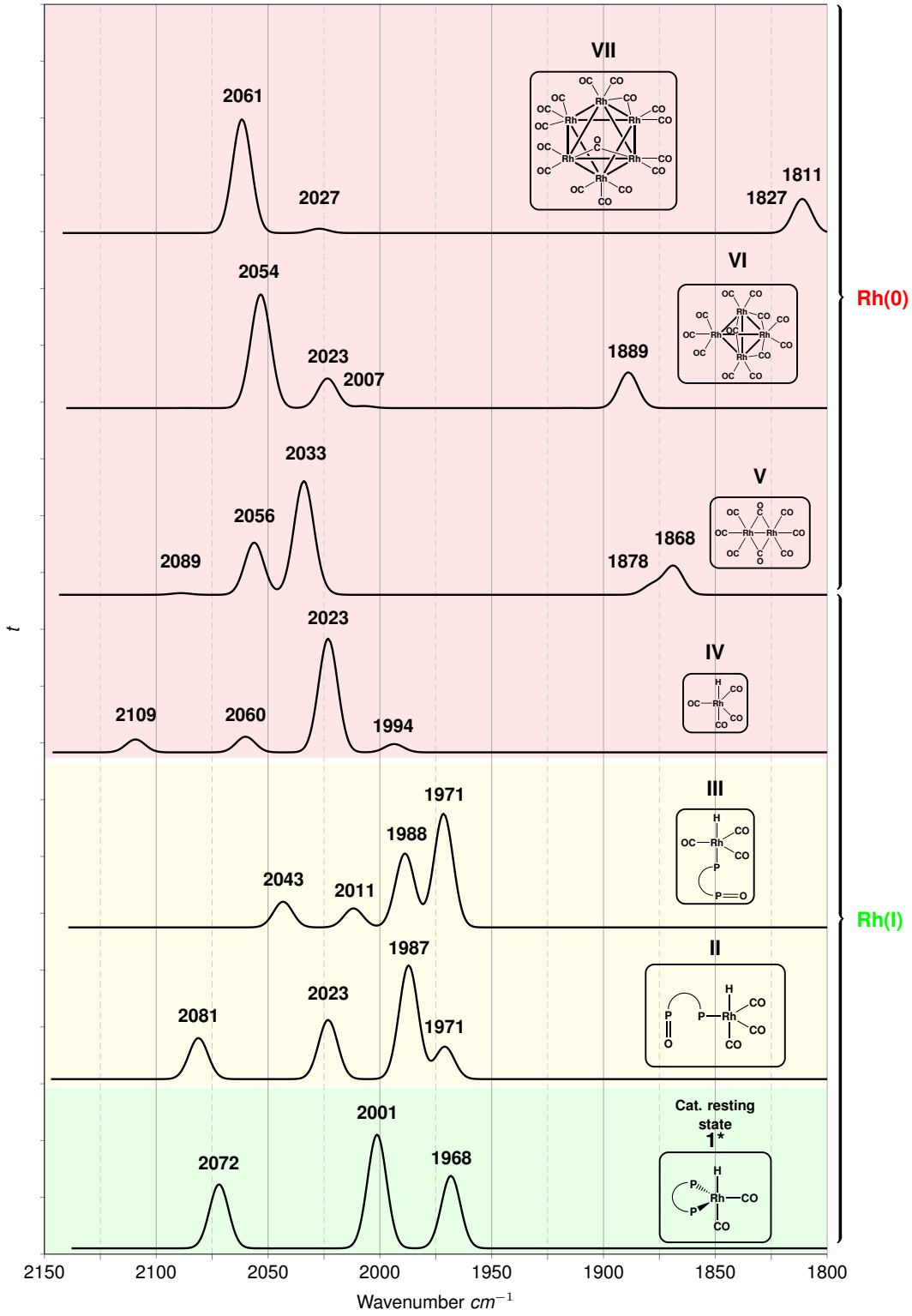

Fig. 4.10.: Calculated IR-spectra of Rh/BPP catalyst in resting state and candidates for degraded species such as oxidized one-arm ligands and formation of rhodium clusters. Obtained from [173]

For degraded species, the Rh/BPP catalyst with oxidized BiPhePhos derivatives are conceivable [49, 176]. One-arm species with a partially oxidized equatorial **II** and axial ligand **III** and the ligand-dissociated $Rh(CO)_4H$ (**IV**) were calculated. External CO could fill the free coordination site so that one-arm complexes with equatorially or axially coordinated BiPhePhos derivatives are formed (see Figure 4.10). The formation of one-arm complexes with a diphosphite ligand and $Rh(acac)(CO)_2$ as precursor was demonstrated by van Rooy et al. by FTIR and nuclear magnetic resonance spectroscopy (NMR) [193]. An increase in the intensity of Rh–CO bands is due to the number of equivalent CO ligands.

New vibrational peaks appear at 1987 cm^{-1} in **II** and 1988 cm^{-1} in complex **III**. The trigonal bi-pyramidal species **II** has two carbonyls and the one-armed BiPhePhos ligand in the equatorial positions, plus the hydride and CO occupying axial positions. The small peak at 1971 cm^{-1} corresponds to stretching vibrations of the axial hydride, and the peaks at 1987, 2023, and 2081 cm^{-1} refer to rhodium–carbonyl bond vibrations. Complex **III** is also a five-coordinated trigonal bipyramidal with an axial coordinated partially oxidized one-arm phosphite. Due to the change in configuration of the mono-dentate ligand, the peak for hydride bond stretch shifts to 2011 cm^{-1}, and the peaks at 1971, 1988, and 2043 cm^{-1} refer to rhodium carbonyl bond stretches. This partial ligand oxidation of the bidentate ligand causes the loss of its characteristic P∩P bite angle, thus reducing the catalyst's selectivity towards the desired n-aldehydes.

When the BPP ligand is fully dissociated, complex **IV** $RhH(CO)_4$ may form which is a trigonal bipyramidal tetracarbonyl rhodium(I) hydride species with the hydride in axial position. The small peak corresponding to metal–hydride stretch is at 1994 cm^{-1}, and the peaks referring to metal carbonyl bond stretch are at 2023, 2030, and 2109 cm^{-1}.

Finally, the formation of Rh carbonyl clusters as dimers, tetramers or hexamers (**V**-**VII**) with special focus on the 1800–2150 cm^{-1} wave number region was investigated. The irreversible formation of $Rh_6(CO)_{16}$ starting from $Rh(acac)(CO)_2$ was also observed by Jiao et al. using FTIR under syngas in absence of a ligand. Here, vibrational bands at 2077 and 1816 cm^{-1} were observed [71]. The formation of these rhodium clusters (complexes **V**-**VII**) is irreversible as experimental studies have shown. No formation of $(BPP)RhH(CO)_2$ catalytic species could be obtained upon injecting more ligand into the catalytic mixture [71]. In contrast, for a Rh/PPh_3-catalyst, Bara-Estaún et al. have reported the formation of Rh(0)–carbonyl clusters to be reversible under H_2-rich conditions [194]. With the cluster formation, new bands in the 1800–1915 cm^{-1} range appear, which correspond to the bridging

carbonyl vibrations for complexes **V** to **VII**. The peaks at 2033, 2056, and 2089 cm^{-1} in complex **V** correspond to terminal metal carbonyl bond vibrations. With the increase in the size of rhodium carbonyl clusters, there is only a minor shift in vibrational band positions but the signal at 2056 cm^{-1} intensifies, and the peak at 2033 cm^{-1} almost disappears for complex **VII** (Rh_6CO_{16}).

For spectral assignment of possible catalyst species due to hydroperoxide-induced degradation of (BPP)RhH-(CO) catalyst, experimental and theoretical IR spectra were compared. Figure 4.11 shows the spectral peak positions and the peak differences from experiment and DFT calculations. Two sets of peaks (**S1** and **S2**) were found in the experimental results. For experimental peak group **S1** ($\tilde{\upsilon}$**S1** = 2098, 2024, 2015 cm^{-1}), there is a difference of $\Delta\tilde{\upsilon}_{exp}$ = 74 cm^{-1} between the first two peaks. For calculated spectra, the difference of $\Delta\tilde{\upsilon}_{calc}$ = 72 cm^{-1} between the peaks in complex **III** (see Figure 4.11) is in good agreement with the experimental peak group difference $\Delta\tilde{\upsilon}_{exp}$ for **S1**.

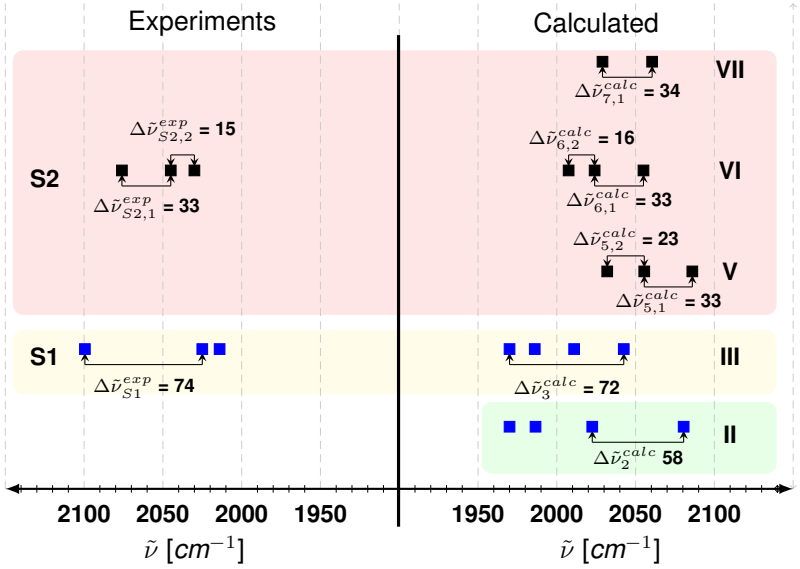

Fig. 4.11.: Comparison of experimental and calculated spectral peak positions (see Figure 4.10) and spacing ($\Delta\tilde{\upsilon}$) for degraded catalyst species. The kinetic experiments were conducted at OVGU Magdeburg by Martin Gerlach. Obtained from [173]

It can also be seen that the peak at 2081 cm^{-1} (Rh–CO stretch) for complex **II** corresponds to the experimental peak at 2098 cm^{-1}. The experimental peak at 2024 cm^{-1} could be assigned to the peak at 2023 cm^{-1} in complex **II** and corresponds to another rhodium–carbonyl stretch. The peak appearing at 2015 cm^{-1} could be seen in complex **III** at 2011 cm^{-1}, which corresponds to the rhodium axial–hydride stretch.

Hence, by comparison with DFT-calculated peak positions and peak experiments it is possible that the spectrum of **S1** corresponds to a mixture of partially oxidized one-arm BiPhePhos species **II** and **III**. The DFT calculations give only a difference of 4 kJ/mol in Gibbs free energy between the mono-oxidized complexes **II** and **III**. Therefore, the inter-conversion between both one-arm species is feasible.

For experimental peak group **S2** ($\tilde{\upsilon}_{S2}$ = 2078, 2045, 2030 cm^{-1}), there is a difference of $\Delta\tilde{\upsilon}_{exp}$ = 33 and $\Delta\tilde{\upsilon}_{exp}$ = 15 cm^{-1} between the first and second peak, as well as the second and third peaks, respectively. For calculated spectra, differences of 33 and 34 cm^{-1} between the peaks in complexes **V-VII** ($\Delta\tilde{\upsilon}_{calc}$, see Figure 4.10) are in good agreement with the experiment peak group difference for **S2**. It is suggested that **S2** represents rhodium carbonyl species without the presence of the BiPhePhos ligand i.e. complexes **IV-VII**. The quantum chemical studies suggest that the characteristic peak of **S2** at 2078 cm^{-1} in the experimental spectra refers to a terminal Rh–C=O stretch vibration which can be found at 2060 cm^{-1} in complexes **IV-VII**. This small difference of -18 cm^{-1} in peak position is not unusual and very sensitive to the choice of functional and basis set. The intensity of the peak increases as the cluster size increases (see Figure 4.10). The difference between the second and third peaks stays almost constant for all the rhodium carbonyl clusters **V-VII**. However, the agreement of the peak spacings suggests that the **S2** mainly comprises of complex **VI**, i.e., $Rh_4(CO)_{12}$.

In summary, deactivation experiments showed that loss of selectivity towards linear aldehydes can be used as fingerprint for catalyst degradation since substrate impurities can cause irreversible changes to the catalyst structure. A comparison to DFT calculated IR spectra of possible candidates for degraded species revealed a good agreement with experimental spectra to identify partially oxidized one-arm derivatives of the ligand BPP and rhodium carbonyl clusters. Based on the experiments, a kinetic model that described catalyst degradation during hydroformylation was proposed. In addition, it was proposed that, for olefin feeds with known hydroperoxide concentrations, periodic dosage of fresh ligand can make up for the diminished selectivity due to the substrate impurities [173].

4.4 Solvent Effects in Hydroformylation

The Gibbs free energy of the hydroformylation reaction (ΔG_r) from olefin to aldehyde shows only a minor solvent dependence of -5 kJ/mol (See Table 4.3), in good agreement with reduction of -7 kJ/mol in Gibbs free energy of reaction reported by

Lamberg et al., when going from a non-polar to a polar solvent using the implicit solvent model COSMO [195].

Tab. 4.3.: Change in of the Gibbs free energy of hydroformylation of 1-decene $\Delta G_{r,hyfo}$ in polar DMF/dodecane solvent mixtures (percentage w/w) at 378 K and 20 bar relative to pure dodecane solvent. The Gibbs free energies of solvation were calculated with COSMO-RS.

	DMF/dodecane composition			
	(100:0)	**(70:30)**	**(50:50)**	**(30:70)**
$\Delta\Delta G_{r,\ hyfo}$	-5	-3.2	-2.3	-1.2

The solvent dependence of individual steps, reactive intermediates and transition states, however, may be different. Figure 4.12 shows the Gibbs free reaction energy profile of hydroformylation of 1-decene by (BPP)RhH(CO) catalyst in the gas phase and in a DMF:dodecance 60:40 solvent mixture.

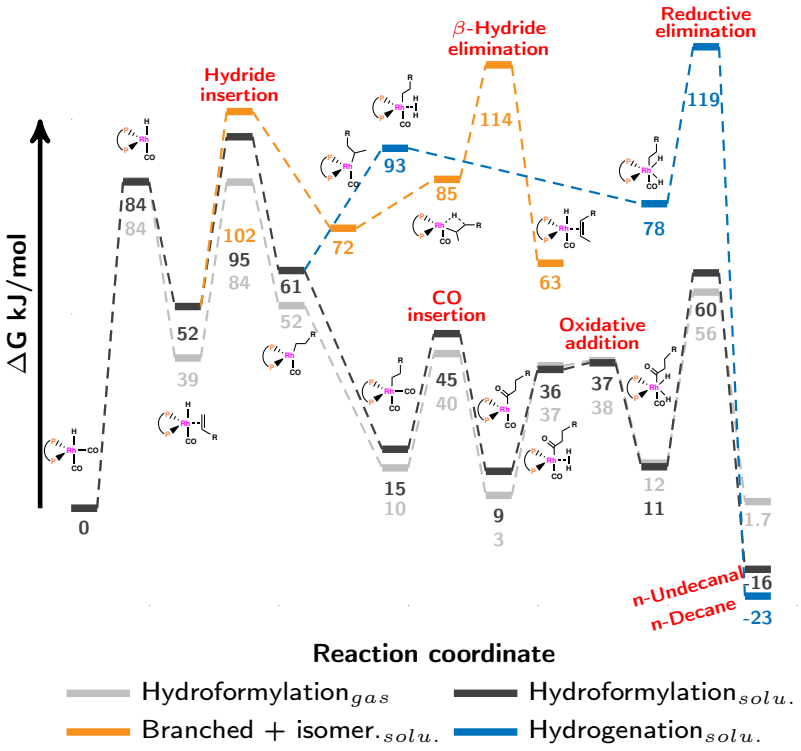

Fig. 4.12.: Solvent effects on the Gibbs free energy profile of the hydroformylation of 1-decence by [(BiPhePhos)RhH(CO)$_2$]. Side reactions such as double bond isomerization towards internal olefins and hydrogenation are included.

In addition to the main hydroformylation reaction cycle forming linear aldehydes, Gibbs free energy profiles of side reactions i.e. the double bond isomerization and hydrogenation are also presented in solution.

The CO dissociation from the pre-catalyst **1** to the active catalyst species **1*** is almost independent of the presence of a solvent (∼84 kJ/mol, see section 4.1.1). However, Gibbs free energy of 1-decene coordination to the BPP/Rh catalyst (**2**) is reduced by 13 kJ/mol in solution compared to the gas phase ($\Delta G_{1\rightarrow 2_{gas}}$ = –45 vs. $\Delta G_{1\rightarrow 2_{solu.}}$ = –32 kJ/mol) making it the most solvent-sensitive reaction step. The solvent lowers the substrate binding affinity by damping the electrostatic interactions between the olefins and catalyst. This destabilization effect will be even more pronounced in polar media (upon increasing the DMF concentration, see Appendix C). In the olefin coordinated catalyst complex **2** and the subsequent transition state for the hydride insertion (TS **2**→**3n**) both the central metal atom and the carbon atoms of the double bond have negative partial atomic charges. In order to proceed with migratory insertion, the hydride changes its polarity from -0.03 to 0.12 (See Figure 4.4) thus, resulting in a reduction in the activation energy for hydride insertion in solution.

Hydride insertion into the Rh-C bond is the highest point in the n-Hyfo reaction cycle relative to the complex **1*** making it the rate-limiting step. The activation energy barrier is increases by 13 kJ/mol in solvent compared to the gas phase relative to the pre-catalyst (84 kJ/mol in gas phase vs. 96 kJ/mol in a DMF/dodecane mixture; see Figure 4.13). This calculated transition state barrier agrees very well with experimental values of 100 kJ/mol for 1-octene using a (XantPhos)RhH(CO) catalyst and CCSD(T) calculations of 104 kJ/mol for the same catalytic system [82].

The solvent effect is largest (12 kJ/mol) for the rate-limiting hydride insertion step due to high sensitivity of substrate binding towards the solvent, whereas it is only 5–10 kJ/mol for the other transition states (See Appendix C).

This emphasizes the necessity of including the solvent effects for the estimation of kinetic parameters. Upon inclusion of solvent effects, the rate of hydroformylation changes by an order of magnitude.

Generally speaking, the first half of the reaction cycle, i.e. from the active catalyst **1*** to the metal-alkyl complex **3n** (Figure 4.2) is more sensitive to solvent effects. The activation energy of hydride insertion relative to complex **2** is slightly reduced (-2 kJ/mol) in solvent. The inclusion of DMF/dodecane does not affect the barrier of CO insertion which remains 30 kJ/mol in the gas phase and in solvent. The binding of molecular hydrogen to the metal-acyl complex **5n** leading to complex **6n** (Figure 4.2) is mildly promoted in solvent (27 kJ/mol in solvent vs. 34 kJ/mol in the gas phase). The subsequent oxidative addition to **7n** is not affected by choice of solvent and the final reduction proceeds with a barrier of 44 kJ/mol in the gas phase and 49 kJ/mol in a DMF/dodecane solution.

In a detailed kinetic network model, olefin coordination was assumed to be rate-determining for both hydroformylation and hydrogenation reactions of 1-decene [187]. Despite several efforts, we were not able to localize a transition state for olefin coordination. Hence, we assumed that the association of 1-decene to the active catalyst is barrierless and should be diffusion controlled. DFT shows that hydride insertion into Rh-C bond has the highest activation energy in the whole reaction cycle.

Since olefin insertion into the transition metal hydride bond is rate-limiting, we explicitly performed a screening of the barrier of this transition state with respect to the composition of the TMS (Figure 4.13).

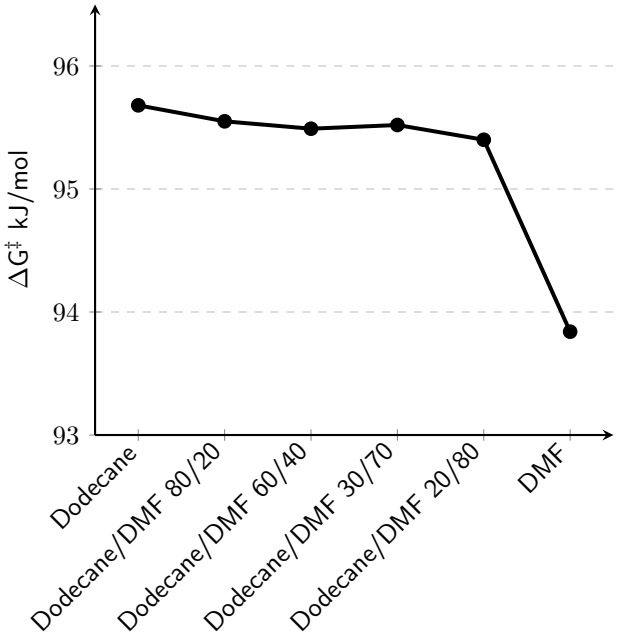

Fig. 4.13.: Solvent control of the transition state barrier of the rate-determining step (1-decene insertion into the Rh-H bond) with BiPhePhos rhodium(I) catalyst.

Solvent stabilization of the transition state geometry is not pronounced. Upon increasing the DMF content from 0 to 20 percent, the barrier reduction is less than 1 kJ/mol. In pure DMF, the stabilization amounts to 2 kJ/mol with respect to pure dodecane. It is this polar medium that has a small effect on the reduction of the transition state barrier (see above). The COSMO-RS treatment of solute-solvent interaction is responsible for the drop by 1 kJ/mol when going from a mixed 20/80 dodecane/DMF solvent to pure DMF. The activation energy for reduction and elimination of undecanal is 6 kJ/mol higher than that for hydride insertion

(43 vs. 49 kJ/mol, see Figure 4.12) and leaves the reductive elimination to be the slowest elementary reaction in the n-hydroformylation cycle when BPP catalyst is used. However, rate of hydroformylation may still be controlled by the hydride insertion step since, upon formation of the Rh-alkyl complex **3n**, the n-aldehyde path is thermodynamically driven downhill.

In solution, the activation energies relative to the pre-catalyst for the side reactions are comparatively higher than the desired linear pathway (double bond isomerization = 114 kJ/mol and hydrogenation = 119 kJ/mol) thus, showing the superior performance of the Rh(BiPhePhos) catalytic system in terms of suppression of iso-aldehyde and alkane formation. In our study we found that the activation energy for hydrogenation to be almost 24 kJ/mol higher than that for hydroformylation in the DMF/dodecane 60/40 solvent system (see Figure 4.12) which is still in good agreement with the experimental 34 kJ/mol higher activation energy for hydrogenation [187].

4.4.1 Finding a Green Solvent Alternative for DMF

It was shown that the DMF concentration in the solvent mixture has a minor influence on the overall activation energy of hydroformylation. Due to the hazardous and toxic nature of DMF, a green solvent alternative must be suggested [44]. To find a promising alternative to polar solvent DMF, thirteen commonly used industrial solvents were investigated as to their effect on the reduction of the activation energy of the rate-determining step $-\Delta\Delta G^{\ddagger}_{RDS}$ (Figure 4.14) using implicit solvation models COSMO-RS and COSMO. The solvent induced reduction of the transition state barrier of the rate-determining step should be maximized (high $-\Delta\Delta G^{\ddagger}_{RDS}$) to achieve high reaction rates. With the increase in solvent polarity (Figure 4.14, x-axis: left to right), the activation energy of the rate-determining step is reduced. The reduction of activation energy going from non-polar to polar solvents is very small (almost 1.5 kJ/mol for COSMO-RS and $\sim$4 kJ/mol for COSMO). However, polar solvents such as short chain alcohols, DMF and N-methyl-2-pyrrolidon (NMP) are preferred. In contrast, solvents such as THF, toluene, or n-heptane are again expected to result in lower reactant-conversion rates. A highly polar solvent such as water does indeed further reduce the activation energy barrier by almost 5 kJ/mol when compared to the activation energy barrier calculated in the absence of solvent. Thus, in principle, could be used as an alternative for DMF. However, water is not an appropriate solvent candidate for the BPP catalyst used in experiments due to its low solubility in water. DMF with a dielectric constant of 37.5 and methanol with 32.7 are expected to perform equally well.

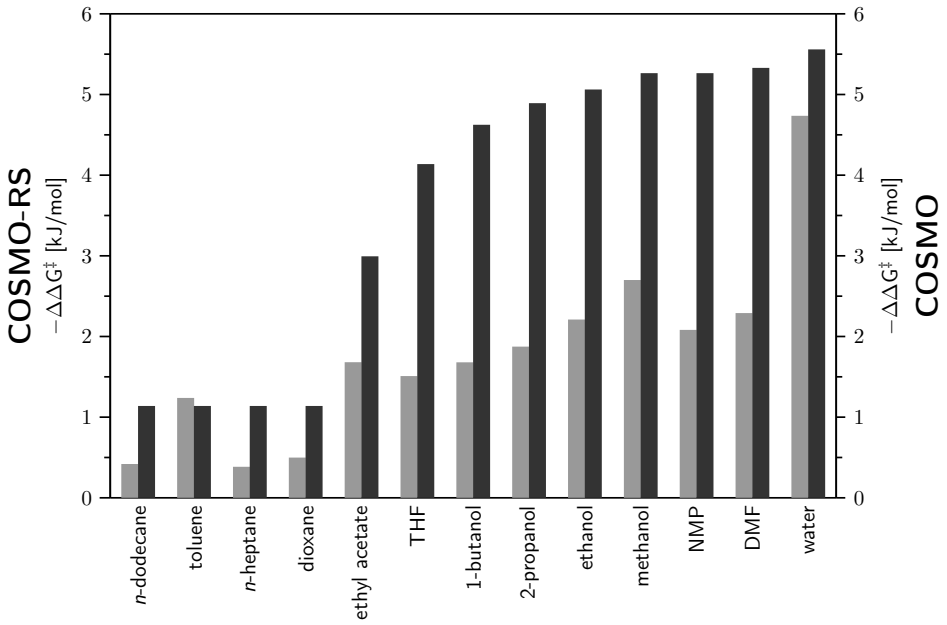

Fig. 4.14.: Solvent effects on the activation energy of the rate-determining step in hydroformylation. The reduction of the transition state barrier at infinite dilution calculated using COSMO-RS (left axis, light gray) and COSMO (right, dark gray) implicit solvation models in 13 different selected solvents relative to those in the gas phase in the absence of any solvent.

Thus, when combining the results from two implicit solvent models, it can be concluded that polar solvents are preferred over non-polar solvents for hydroformylation. As a result of the solvent screening steps, the number of promising solvents candidates is significantly reduced. DMF, NMP, and methanol are expected to show similar performance in terms of reduction of activation energy for the rate-determining step. However, they can further be investigated based on their explicit coordination to the catalyst.

Since the polarity of the solvent has a minor effect on the rate of hydroformylation, methanol can be a possible green solvent substitute for DMF. However, the electron withdrawing phosphite BiPhePhos catalyst is insoluble in methanol [196], a TMS solvent mixture using methanol as polar solvent is not possible for this catalyst. Therefore, a catalyst with a different ligand that is soluble in methanol must be selected without compromising the catalyst's activity and selectivity. Therefore, a water-soluble rhodium–SulfoXantPhos catalyst was selected due to its high selectivity towards linear aldehydes. Since long-chain olefins such as 1-decene are not soluble in water, their solubility can be increased by either using nonionic surfactants acting carriers for the substrate and catalyst [197] or by using a co-solvent such as 1-butanol (formation of biphasic system) [198]. However, the former system

suffers from low activity and the latter from high catalyst leaching (15 ppm) in the product phase. A TMS solvent system using methanol instead of water as polar and decane as non-polar solvent was successfully reported for hydroaminomethylation (hydroformylation + reductive amination) reaction using an electron donating SulfoXantPhos catalyst [189].

4.5 Conclusions for Rh-Catalyzed Hydroformylation

Upon mechanistic elucidation including all elementary steps the rate limiting step is located for BPP/Rh catalyzed hydroformylation of long-chain renewable olefins with 1-decene as a model substrate. The pathway towards the desired linear n-aldehyde is kinetically preferred which rationalized the high selectivity of BiPhePhos. Impurities in the olefin substrates reduce the catalyst's selectivity towards the desired linear aldehydes and generates partially oxidized one-arm derivatives of ligand BiPhePhos and rhodium carbonyl clusters. Double bond isomerization at the catalyst and olefin hydrogenation are chemically possible side reactions but are kinetically disfavored.

Solvent effects and solvent control of the thermodynamics and kinetics of each intermediate species and transition state are presented. Whereas the chemical equilibrium is almost unchanged, the individual chemical steps in the reaction cycle show various dependencies. Whereas the presence of a solvent slightly reduces the activation energy for hydride insertion, the activation energy for CO insertion and oxidative addition of H_2 is independent of solvent effects and the barrier for the reductive elimination increases by 5 kJ/mol.

With hydride insertion as the rate-determining step, the control of the kinetics of this step can drive the yield of the entire process. A careful choice of solvent which stabilizes this transition state but does neither inhibit the catalyst nor product release is a delicate issue. 'Green solvents' with a reduced environmental impact also support the transformation of the chemical industry towards sustainability. Computer-aided solvent design will be helpful in accomplishing this task.

5 Computer-Aided Solvent Selection for Rhodium Catalyzed Reductive Amination of Aldehydes

This chapter focus on the solvent selection for homogeneously catalyzed complex multi-step reactions. For this purpose, a multi-step solvent screening approach is proposed that can reduce the overall experimental burden associated with the design and selection of highly active solvent systems. This process is outlined in Figure 5.1 and composed of following steps:

1. Resolution of the complete reaction mechanism in a vacuum provides information about the thermodynamics of the reaction: Gibbs free energy, $\Delta G^{0}{}_{r(gas)}$, and the kinetics: rate-determining step, $\Delta G^{\ddagger}{}_{r(gas)}$.

2. An estimation of the impact of solvent polarity on the thermodynamics and kinetics for a number of solvent candidates using a simple continuum solvent model yields de/stabilization in the Gibbs free energy of reaction $-\Delta\Delta G_{r(solu)}$ and the activation energy of the rate-determining step $-\Delta\Delta G^{\ddagger}{}_{r(solu)}$ in solution. Furthermore, the thermodynamic activity coefficient (a) of the reactants in different solvents is another possible descriptor for solvent screening. The aim of the screening is to find a solvent with the lowest activation energy barrier for the rate-determining step and the highest thermodynamic activity for the reactant in that given solvent, thus maximizing the reaction rate.

3. Calculate the explicit solute-solvent and catalyst-solvent interactions using the top-ranked solvents from the previous step to find the solvent with the highest activity.

4. Validate the model-predicted solvent candidates through experiments.

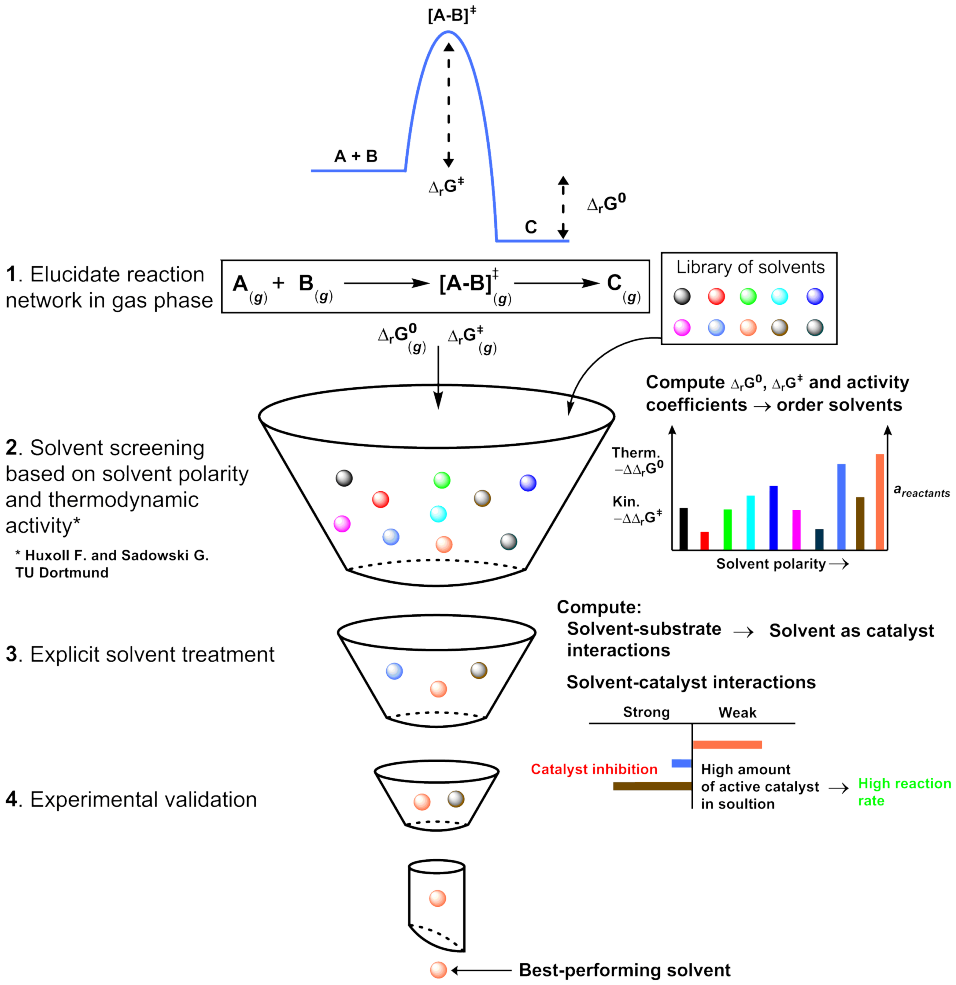

Fig. 5.1.: Process to screen solvent candidates for complex, homogeneously-catalyzed multi-step chemical reactions.

This solvent screening workflow will be discussed in detail and applied to an exemplary case of transition metal-catalyzed reductive amination (RA) of aldehydes, as it illustrates the different types of solvent interactions that are crucial for solvent selection. A rhodium(I)/SulfoXantPhos catalyst is used for the hydrogenation of the enamine ((E)-N,N-diethylundec-1-en-1-amine) produced from the reaction of 1-undecanal (representing long-chain aldehydes) and diethylamine (DEA) as substrates. A complete reaction mechanism for the reductive amination of long-chain aldehydes is resolved, with special emphasis on the solvent effects on all elementary steps. The results presented in this chapter are obtained through the implementation of quantum mechanical methods presented in chapter 3.

Parts of this chapter were published in the following research articles:

- Jameel F., and Stein M., The Many Roles of Solvent in Homogeneous Catalysis - The Reductive Amination Showcase, Journal of Catalysis 405, 2022, 24-34 [199].
- Huxoll F., Jameel F., Bianga J., Seidensticker T., Stein M., Sadowski G., and Vogt D., Solvent Selection in Homogeneous Catalysis—Optimization of Kinetics and Reaction Performance, ACS Catalysis 11, 2021, 590-594 [200].
- Kirschtowski S., Jameel F., Stein M., Seidel-Morgenstern A., Hamel C., Kinetics of the reductive amination of 1-undecanal in thermomorphic multicomponent system, Chemical Engineering Science 230, 2021, 116187 [13].
- Jameel F., Huxoll, F., Stein, M., Sadowski, G., (2022). Solvent Selection for Reactions in Liquid Phases. In Kraume, M., Enders, S., Drews, A., Schomäcker, R., Engell, S. & Sundmacher, K. (Ed.), Integrated Chemical Processes in Liquid Multiphase Systems. From Chemical Reaction to Process Design and Operation: De Gruyter [154].

Reductive amination (RA) is an atom-efficient technique for synthesizing amines [201] that results in only water as a byproduct. It is an approach that is highly valued in green chemistry due to its ability to generate minimal waste. The reaction initiates with the nucleophilic addition of an amine to the carbonyl group of an aldehyde to produce a hemiaminal, and a subsequent dehydration step results in an enamine or imine. Recent mechanistic studies suggest that the enamine pathway is preferred in neutral media [202]. In contrast, the protonation of the aldehyde or amine nitrogen in the presence of an acid results in imine or iminium intermediates, respectively. The hydroaminomethylation reaction with a rhodium diphosphine catalyst was investigated through high-pressure NMR experiments, which confirmed the existence of enamine species before hydrogenation. Hence, this study is focused on the reductive amination via the enamine pathway. The final tertiary amine is obtained by hydrogenation of the enamine in the presence of a transition metal catalyst and hydrogen gas (Figure 5.2).

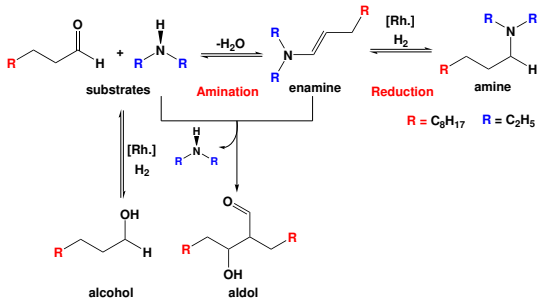

Fig. 5.2.: Production of long-chain diethylamines from aldehydes via reductive amination.

Possible side reactions are the formation of alcohols by catalytic hydrogenation of aldehyde and aldol condensation.

5.1 Reaction Mechanism

Figure 5.3 displays the complete reaction mechanism for rhodium-catalyzed reductive amination (RA), including all possible elementary steps. Reaction begins with the association of substrates to form a pre-complex **2**, followed by the nucleophilic attack of diethylamine on the undecanal and formation of a hemiaminal (**3**) intermediate. Water is released as a result of intramolecular condensation where OH^- dissociates first, followed by proton abstraction from the second carbon to produce an enamine (**5**). Either a cationic rhodium species or a Rh(I)-hydride has been previously discussed in the literature as an active catalyst for enamine reduction. The latter has only been characterized and assigned by ^{1}H NMR studies [203].

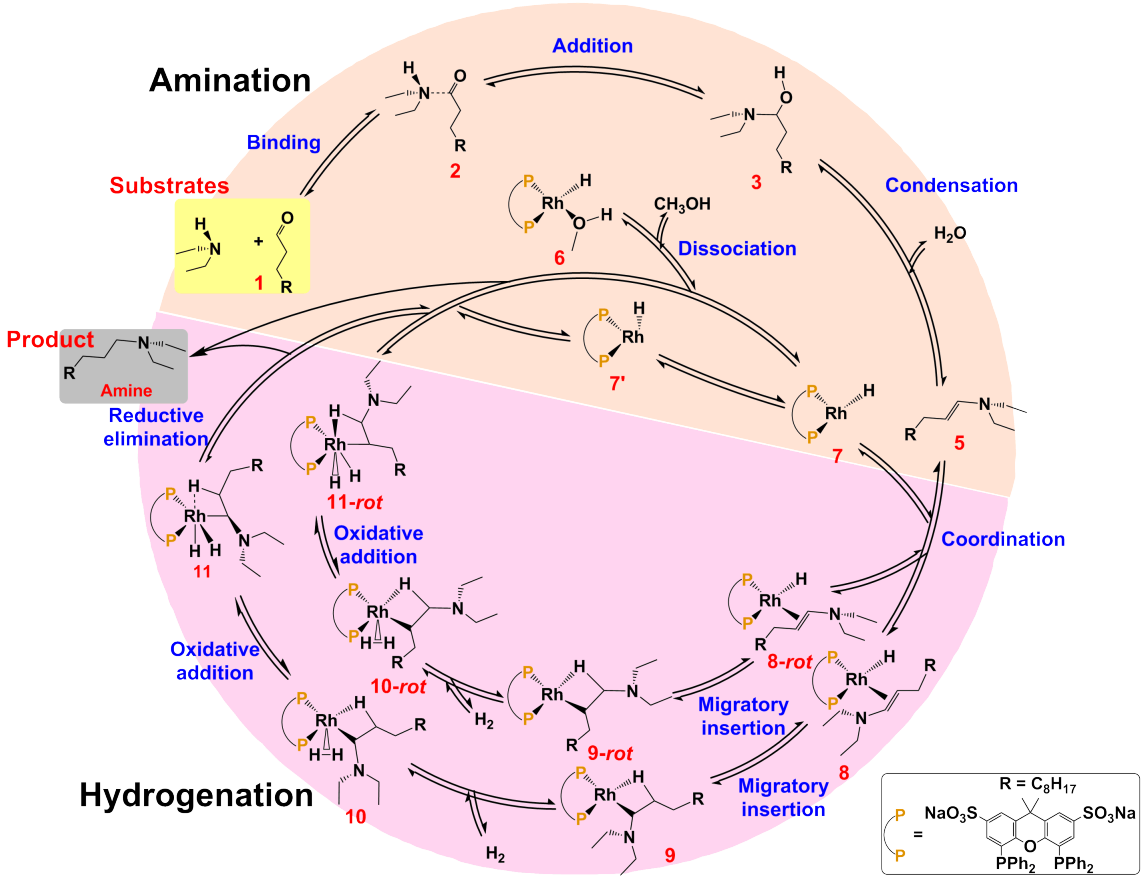

Fig. 5.3.: Synthesis of long-chain amines from aldehydes obtained from oleochemicals and diethylamine by a bidentate phosphine Rh-hydride catalyst. All steps, intermediates, and transition states connecting them are described in the text.

Upon dissociation of a solvent molecule from pre-catalyst **6**, a free binding site is formed at the catalyst (**7**), facilitating subsequent binding of the substrate enamine and formation of complexes **8** and **8-rot**. Alkylamine complexes **9** and **9-rot** are generated via hydride migratory insertion into the enamine. Later, hydrogen (H_2) coordination to the metal center leads to the complexes **10** and **10-rot**, which then is followed by H_2 oxidative addition resulting in complexes **11** and **11-rot**. Finally, the tertiary amine product is released as a result of the reductive elimination reaction and the catalyst is regenerated.

5.2 Solvent Effects on Amination

The Gibbs free energy for the amination of 1-undecanal and diethylamine (DEA) is 6.2 kJ/mol at 373 K in the gas phase using the PBE0-D3(BJ)/def2-TZVP hybrid density functional. The PBE0 density functional was chosen after a benchmark study of a number of rhodium catalyzed reactions, where the performance of different density functionals was compared with DLPNO-CCSD(T) coupled cluster calculations (for details, see Appendix B). Figure 5.4 illustrates how the Gibbs free reaction energy of amination using a continuum solvation model COSMO is affected by the polarity of twelve frequently employed industrial solvents, as indicated by their solvent dielectric constants (ϵ). The thermodynamics of amination of 1-undecanal and DEA depend significantly on the polarity of the solvent, since non-polar solvents suppress enamine formation. However, in polar solvents (Δ G_r = -2 kJ/mol) the enamine formation is thermodynamically driven.

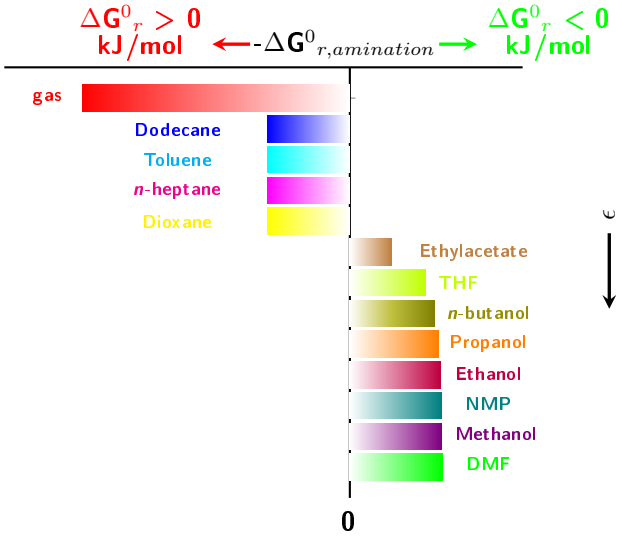

Fig. 5.4.: Solvent effects on the thermodynamics of enamine formation.

Figure 5.5 displays the Gibbs free energy profile for the amination of 1-undecanal and DEA to form the enamine (**5**) in both the gas phase and an implicit solvent comprised of a mixture of methanol and dodecane in a 99:1 w/w composition. The COSMO-RS solvent model was utilized to calculate the solvent effects, and the selection of methanol:dodecane solvent mixture stems from experiments.

In the absence of solvent, the change in Gibbs free energy for the association of diethylamine and 1-undecanal is 18 kJ/mol, which increases by 9 kJ/mol in solution. The activation energy associated with the proton transfer was calculated to be 143 kJ/mol in the gas phase. Polar solvent, on one hand, de-stabilize the intermediate (**2**) prior to the transition state and, on the other hand, stabilize the transition state, thus reducing the activation energy by 20 kJ/mol ($\Delta G^{\ddagger}_{2\rightarrow 3}$ =123 kJ/mol). Formation of hemiaminal complex (**3**) is almost independent of the solvent as the Gibbs free energy of hemiaminal formation decreases by only 1 kJ/mol (from -4 to -5 kJ/mol) when only the polar effect of the solvent is considered. Water is formed when the OH^{-} abstracts an proton from the β-carbon and as a result enamine is generated. The activation energy for this intra-molecular condensation is 177 kJ/mol in gas phase. Inclusion of implicit solvent reduces the activation energy by 17 kJ/mol ($\Delta G^{\ddagger}_{3\rightarrow 5}$ =160 kJ/mol).

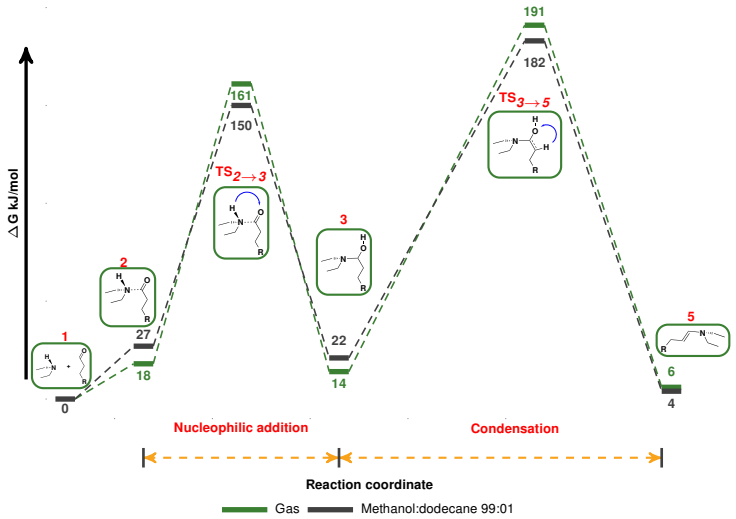

Fig. 5.5.: Gibbs free energy profiles of enamine (**5**) formation at (373 K and 30 bar) from undecanal and DEA as substrates in gas phase and in an implicit polar solvent. The Gibbs free energies of solvation were calculated for methanol:dodecane 99:1 w/w solvent mixture using COSMO-RS. The Gibbs free energies were calculated at PBE0-D3(BJ)/def2-TZVP level of theory.

The activation energies of the transition states are reduced by 17-20 kJ/mol when implicit solvent models are used to estimate solvent effects. Nevertheless, these

activation energies are quite high due to the ease with which enamine are usually produced, i.e. by stirring the substrates in conventional organic solvents. This indicates that the direct addition-dehydration mechanism, as depicted in Figure 5.5, is less probable. Therefore, it is hypothesized that amination occurs through an alternative mechanistic pathway, where substrate-solvent interactions explicitly stabilize the activation energies of transition states. Such interactions cannot be estimated using only continuum solvent models, but a cluster-continuum solvent model can provide estimations (refer to theory 3.2.3). Boz and colleagues suggest that the water generated during amination may reduce the activation energies of transition states by acting as a proton transfer agent [202]. However, an excess of water in the reaction mixture will shift the thermodynamic equilibrium towards the reactant side and thus stop the formation of enamine. Short-chain alcohols, such as methanol and ethanol, have the ability to form hydrogen bonds with the substrate (proticity) and can act as proton transfer agents during amination. Long-chain alcohols were not investigated due to the large size of possible conformational space. Therefore, we used a cluster-continuum solvent model to investigate the effect of methanol as a polar, hydrogen bond donating (protic) solvent for amination.

5.2.1 Explicit Solvent Coordination

To resolve the substrate-solvent interactions in the presence of explicit solvent molecules, at first, solvent coordination sites, where a solvent molecule can bind to the substrate, should be resolved. The carbonyl oxygen of the long-chain *n*-aldehyde has two electron lone pairs hence it acts as a hydrogen bond acceptor of two methanol molecules.

In the most plausible scenario, diethylamine acts as a hydrogen bond donor and forms a hydrogen bond with one methanol, enhancing the amine's basic character (Figure 5.6, left). However, when the nitrogen lone pair of diethylamine is the hydrogen bond acceptor of a methanol proton, the amine's lone pair is not available for the nucleophilic attack to the carbonyl group. This binding situation is feasible but the barrier for the nucleophilic attack is far too high (Figure 5.6, right).

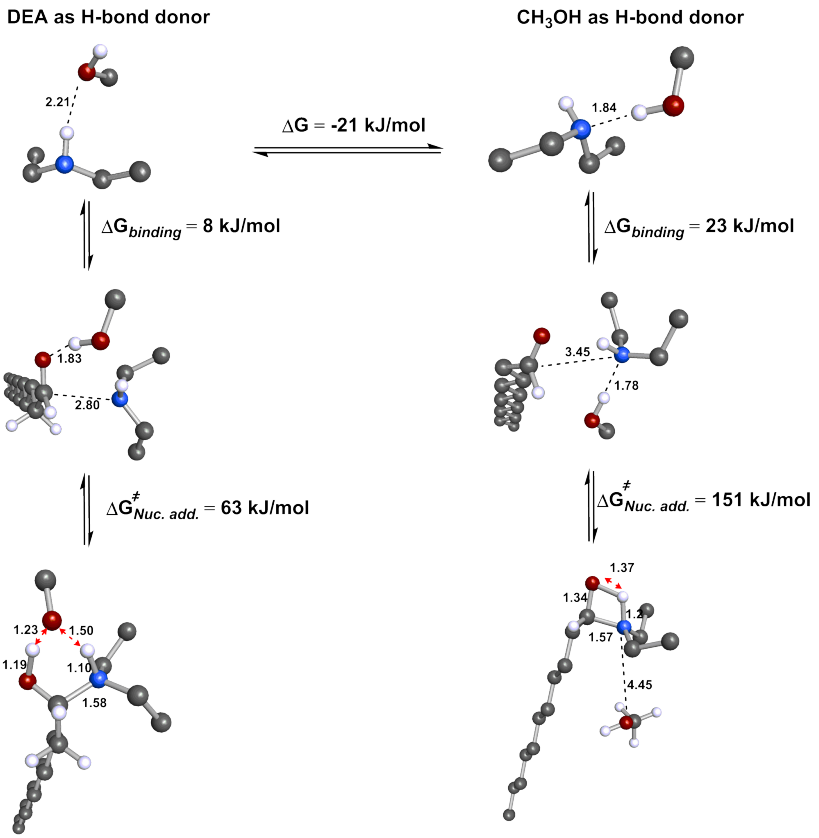

Fig. 5.6.: Substrate binding and nucleophilic addition of diethylamine to the undecanal when (left) diethylamine, (right) methanol acting as hydrogen bond donor. The structures were optimized at PBE0(D3)/def2-TZVP level of theory.

Secondly, the optimal number of explicit solvent molecules should be found to describe the substrate-solvent interactions accurately, as excessive number of explicit solvent molecules will significantly increase the computation costs. Pliego and Riveros [163] have suggested that the explicit solvent molecules should be introduced incrementally into the cluster, followed by an optimization of the structure to find the energy minima. When the incremental changes in Gibbs free energies between $(n+1)$ and n solvent molecules becomes negligible, it gives the optimal number of solvent molecules to describe the solvent effect from the first solvation shell. Finally, the solvation effects beyond the first solvation shell are included via continuum solvation.

Here, the bulk solvent effects (solvent effects due to the polarity of solvent), were estimated in three different solvent compositions (pure dodecane, methanol:dodecane 50:50, methanol:dodecane 99:1 solvent mixtures). Figure 5.7 shows the incremental change in the Gibbs free energy of binding of 1-undecanal and DEA with respect to the number of explicit molecules.

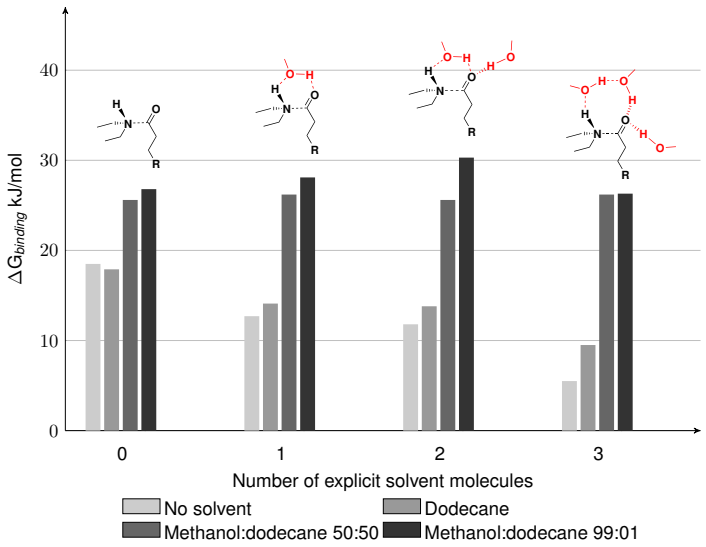

Fig. 5.7.: Gibbs free energy of substrates (1-undecanal and DEA) binding in the presence of explicit solvent molecules. The bulk solvent effects were calculated using an implicit solvent model COSMO-RS.

In the absence of solvent, the change in Gibbs free energy upon association of diethylamine and 1-undecanal is 18 kJ/mol, which slightly decreases by 0.6 kJ/mol in pure dodecane but increases by 7 and 8 kJ/mol in methanol:dodecane 50:50 and 99:1 solvent mixtures, respectively.

Methanol may act as a hydrogen bond donor to the carbonyl oxygen and simultaneously as an acceptor of the proton from diethylamine. This reduces the Gibbs free energy of association by 5.8 kJ/mol. When solvent effects are taken into account using an implicit solvent model, it increases again by 1.4, 13.5, and 15.4 kJ/mol in pure dodecane and methanol:dodecane 50:50 and 99:1 mixed solvents, respectively. The origin of this increase in energies of association is the de-solvation penalty that increases with solvent polarity.

A second methanol molecule may form another hydrogen bond to the carbonyl oxygen, but it reduces the Gibbs free energy of association by a mere 1 kJ/mol. Implicit solvation slightly destabilizes complex formation and shows the same trend as for the single methanol molecule coordination.

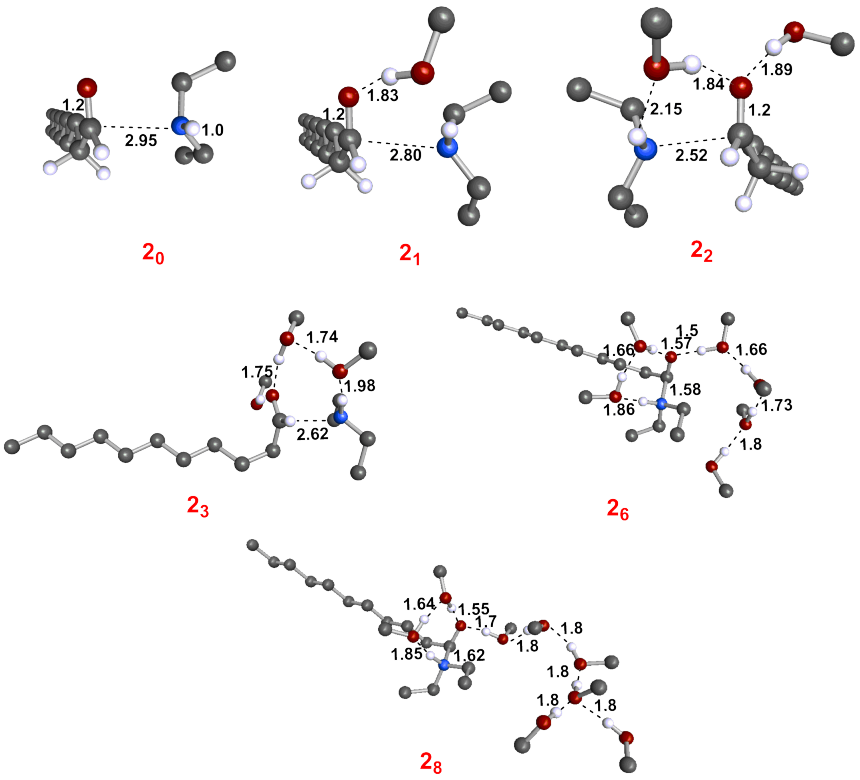

Fig. 5.8.: Structural details for solvent assisted substrates binding. Hydrogen atoms from the non-polar chain were omitted for clarity. Atomic distances (black) are given in Angstroms.

The addition of a third methanol molecule affords such a cyclic micro-solvation with the lowest Gibbs free energy of association (5.5 kJ/mol). Considering implicit solvation leads to an increase by 4 and 20 kJ/mol in dodecane and mixed methanol:dodecane solutions. No significant change in the Gibbs free energy was observed upon considering higher number ($n = 6$ and 8) of explicit solvent molecules, as they do not interact directly with the solute (Figure 5.8).

Similarly, the effect of the number of explicit solvent molecules on the activation energy of proton transfer (Figure 5.9) from amine to aldehyde were also investigated. In the absence of solvent, nucleophilic addition and proton transfer occur simultaneously with an activation energy of 142 kJ/mol. Solvent only has a minor effect on the activation energy of the corresponding transition state when its effect are calculated using an implicit solvent model. The activation energy of the simultaneous nucleophilic addition and proton transfer reduces by 4, 18, and 21 kJ/mol in pure dodecane and methanol:dodecane 50:50 and 99:1 solvent mixtures, respectively. Determining the ideal number of explicitly coordinating solvent molecules

to a transition state structure is a complex task. In this case, the explicit solvent molecules can participate in the reaction mechanism as proton transfer agents.

Explicit coordination of one methanol molecule mediates proton transfer through a six-membered concerted transition state. The activation energy barrier is reduced by 80 kJ/mol due to methanol coordination. Furthermore, the barrier is reduced by 5, 13, and 16 kJ/mol in pure dodecane and methanol:dodecane 50:50 and 99:1 solvent mixtures, respectively, when bulk solvent effects are included using an implicit solvent model.

Hydrogen bonding of a second methanol molecule to the aldehyde reduces the transition state energy by a further 14 kJ/mol relative to the one methanol assisted transition state. When implicit solvent effects are included, the Gibbs free energy of activation is only slightly further reduced by 3, 7, and 13 kJ/mol in pure dodecane and methanol:dodecane 50:50 and 99:1 solvent mixture, respectively.

When three explicit methanol molecules are considered, the proton from diethylamine is transferred to undecanal via a two methanol proton shuttle. This gives a transition state barrier of 16.4 kJ/mol which is a 126 kJ/mol lower with respect to the direct proton transfer. The activation energy exhibits minor dependence on solvent polarity, with values of 17, 19, and 20 kJ/mol in pure dodecane and solvent mixtures of methanol:dodecane 50:50 and 99:1, respectively.

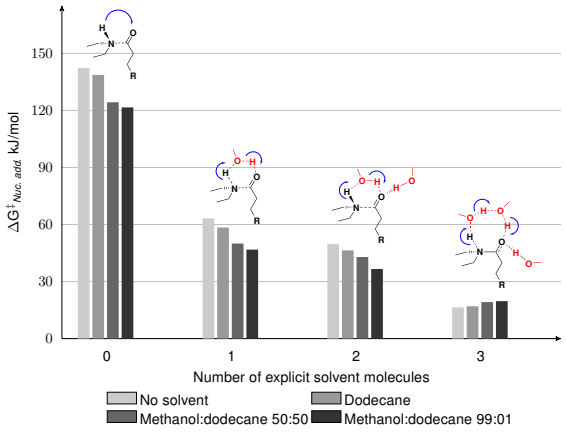

Fig. 5.9.: The effect of explicit solvent interactions on the Gibbs free energy of the transition state for the initial proton transfer from the amine to the aldehyde. The bulk solvent effects were calculated using implicit solvent model COSMO-RS in pure dodecane and methanol:dodecane 50:50 and 99:1 solvent mixture.

The lowest activation energy is obtained when three explicit methanol molecules are considered; when one explicit methanol forms a hydrogen bond with the carbonyl

oxygen and two explicit methanol molecules form a proton shuttle (Figure 5.10; left). To confirm this result, the possibility of three methanol molecules making a proton shuttle and none of forming a hydrogen bond with the carbonyl oxygen (TS 3_3; Figure 5.10; center) was also considered. The transition state for this cyclic path is 32 kJ/mol higher than the two proton shuttle transition state. In addition, a proton transfer transition state involving 6 explicit methanol molecules was also optimized. Here, two methanol molecules form the proton shuttle, one forms a hydrogen bond to the carbonyl oxygen and the remaining 3 form a linear chain of hydrogen-bonded methanol cluster (TS 3_3; Figure 5.10; right). The calculated activation energy for the transition state with 6 explicit molecules is again 10 kJ/mol higher than the transition state with three explicit solvent molecules. Therefore, it can be concluded that the transition state with three explicit methanol molecules, where two form a proton shuttle and one one is coordinated to carbonyl oxygen, is the kinetically one. Thus, the systematic approach to find the optimum number of explicit solvent molecules has shown that two solvent molecules coordinating to the carbonyl oxygen lone pairs plus one solvent molecule bridging between the substrate are the optimal number solvent molecules required for the description of the first solvation shell.

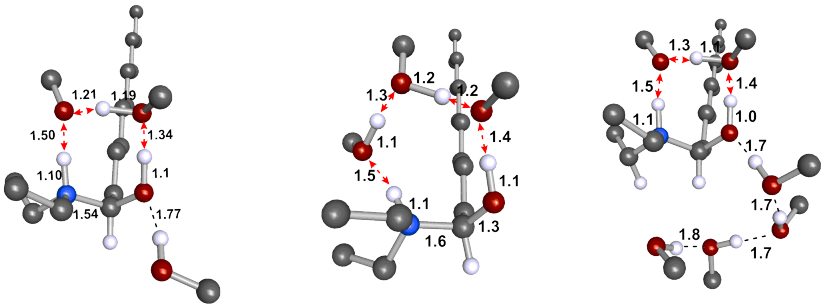

Fig. 5.10.: Structural details for solvent assisted proton transfer from amine to aldehyde in the presence of three explicit methanol molecules, left: two making a proton shuttle and one coordinated to carbonyl oxygen and center: three solvent molecules making a proton shuttle assisting the proton transfer. Right: six explicit solvent molecules: two making a proton shuttle, one making a hydrogen bond with carbonyl oxygen and remaining three coordinated to the latter methanol resulting in a linear chain. Hydrogen atoms from the non-polar chain were omitted for clarity. Bond distances (black) are given in Angstroms.

5.2.2 Solvent Effects on Hemiaminal Formation

Following the nucleophilic addition of diethylamine to the undecanal, the subsequent proton transfer leads to the hemiaminal (3; Figure 5.3). Table 5.1 shows the effects

of implicit solvation and explicit methanol coordination on the thermodynamics of hemiaminal formation.

Tab. 5.1.: Solvent effects on the formation of the hemiaminal (3). Gibbs free energies are given in kJ/mol. The solvent molecules in the first solvent shell were treated explicitly, plus the bulk solvent effects were calculated in pure dodecane and methanol:dodecane 50:50 and 99:1 solvent mixture using implicit solvent model COSMO-RS.

No of explicit solvent molecules	No implicit solvent	dodecane	Methanol: dodecane (50:50)	Methanol: dodecane (99:1)
0	-4.9	-2.8	-4.7	-5.0
1	2.2	2.0	0.7	0.2
2	-6.0	-5.3	-4.4	-4.5
3	-12.6	-12.2	-8.6	-4.9

In the absence of any solvent treatment, the Gibbs free energy for hemiaminal formation is -4.9 kJ/mol and is only slightly dependent on the composition of polar/non-polar methanol:dodecane mixed solvents. Non-polar dodecane leads to an increase by 2 kJ/mol in Gibbs free energy, but with increasing methanol composition, the free energy of reaction reaches -4.7 and -5 kJ/mol.

When explicit coordination of one methanol is considered, the formation of the hemiaminal becomes marginally endothermic (2.2 kJ/mol). The consideration of implicit solvent effects lowers the Gibbs free energy by 0.2, 1.5, and 2 kJ/mol in pure dodecane and methanol:dodecane 50:50 and 99:1 solvent mixtures, respectively and brings it close to a thermoneutral process.

Hydrogen bonding of a second explicit methanol significantly affects the thermodynamics of hemiaminal formation. The Gibbs free energy of hemiaminal formation is reduced by 8.2 kJ/mol compared to the single methanol coordinated complex. When the solvent effect is taken into account using an implicit solvent model, the Gibbs free energy of the hemiaminal formation exhibits only a minimal dependence on solvent. In pure dodecane and methanol:dodecane 50:50 and 99:1 solvent mixtures, it becomes -5.3, -4.4, and -4.5 kJ/mol, respectively.

Three methanol molecules, two of which are coordinating to the carbonyl oxygen lone pairs, and the third is bridging between the amine group and one methanol solvent molecule, constitute the complete first solvation shell. Attempts to incorporate more solvent molecules were unsuccessful and did not improve the energetics any further. The formation of the hemiaminal becomes thermodynamically favored

(-12.6 kJ/mol) when three explicit solvent molecules are considered. When considering the polar effects of solvent using an implicit solvent model, the energy increases by 0.4, 4, and 7.3 kJ/mol in pure dodecane, as well as methanol:dodecane 50:50 and 99:1 mixed solvents, respectively. However, this process remains exothermic and is in line with the experimentally established thermodynamic equilibrium constant of 8.5 M^{-1}, corresponding to a Gibbs free energy of -5.4 kJ/mol for hemiaminal formation [204].

5.2.3 Solvent Effects on Condensation

Water release from the hemiaminal (**3**) yields (E)-N,N-diethylundec-1-en-1-amine (enamine) **5**. In an intra-molecular condensation reaction, at first, OH^- dissociates and then a proton is abstracted from the β-carbon of the hemiaminal resulting in formation of a water molecule. Table 5.2 gives the effects of explicit and implicit solvation on the activation energy barrier of condensation.

Tab. 5.2.: Solvent effects on the Gibbs free energies of the transition state of enamine (**5**) formation (in kJ/mol) via a condensation step from the hemiaminal **3**. The solvent molecules in the first solvent shell were treated explicitly while the bulk solvent effects were calculated in pure dodecane and methanol:dodecane 50:50 and 99:1 solvent mixture using an implicit solvent model COSMO-RS.

No of explicit solvent molecules	No implicit solvent	dodecane	Methanol: dodecane (50:50)	Methanol: dodecane (99:1)
0	177	172	163	160
1	116	111	97	94
2	99	95	96	94
Concerted Release of Water				
3′	77	76	75	72
Stepwise Release of Water				
3″	47 15	47 18	45 20	45 23

In the absence of a solvent, water is released directly through a four-membered transition state with an activation energy barrier of 177 kJ/mol. When solvent effects are considered using an implicit solvent model, the activation energy decreases by 5, 14, and 17 kJ/mol in pure dodecane, methanol:dodecane 50:50, and 99:1 mixtures.

When methanol acts as a proton transfer agent, it releases water through a six-membered transition state that lowers the activation energy barrier by 61 kJ/mol

compared to the activation energy without explicitly considering the solvent influence. Furthermore, the addition of bulk solvent effects by means of an implicit solvent model results in an additional reduction of the barrier by 5, 19, and 22 kJ/-mol in pure dodecane and 50:50 and 99:1 methanol:dodecane solvent mixtures.

The Gibbs free energy of the transition state decreases by an additional 17 kJ/mol when two methanol molecules aid the condensation step, as opposed to only one explicit methanol assistance. Furthermore, the activation energy decreases by 4, 3, and 6 kJ/mol when incorporating the polar effects of solvents with an implicit solvent model in pure dodecane, methanol 50:50, and 99:1 solvent mixtures, respectively.

When three methanol molecules are explicitly considered, the formation of the enamine **5** can either occur in a concerted or step-wise manner, as depicted in Figure 5.11. Prior to releasing water, explicit solvent molecules reorient, leading to complexes $\mathbf{3'}_3$ and $\mathbf{3''}_3$, both of which are slightly higher in energy compared to the previous intermediate $\mathbf{3}_3$.

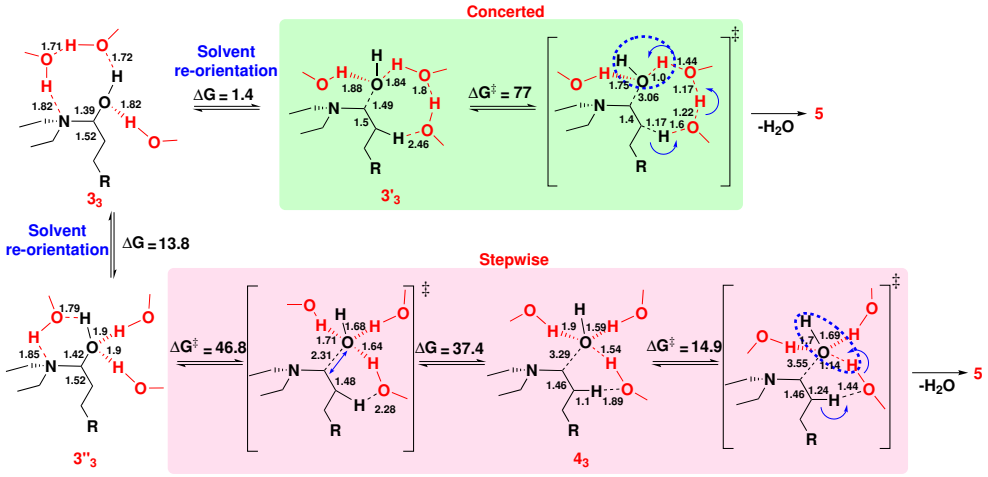

Fig. 5.11.: A concerted and step-wise mechanism for the formation of (E)-N,N-diethylundec-1-en-1-amine (enamine) **5** via solvent assisted condensation of a hemiaminal intermediate (energies in kJ/mol). Explicit solvent molecules are shown in red, blue arrows depict the proton movement, and the interatomic distances in Å are given in black.

In complex $\mathbf{3'}_3$, two solvent molecules form a cyclic structure between the carbonyl oxygen and a proton from the β-carbon. The third molecule forms a second hydrogen bond with the oxygen of the hemiaminal complex. The re-orientation of solvent molecules from $\mathbf{3}_3$ to $\mathbf{3'}_3$ is almost thermoneutral with a slight change in the Gibbs free energy of + 1.4 kJ/mol, which upon inclusion of solvent effects using an implicit solvent model, it becomes 2.0, –2.8, and –5.4 in pure dodecane and methanol:dodecane 50:50 and 99:1 solvent mixture, respectively.

Following the formation of the intermediate $\mathbf{3'}_3$, the condensation proceeds in a concerted mechanism. Where the proton abstracted from the β-carbon by the solvent molecule and then transferred to the hydroxide via a two methanol molecule proton shuttle. The activation energy barrier for this pathway is 77 kJ/mol, which is almost 22 kJ/mol lower than for the two methanol case (See Table 5.2). Bulk electrostatic solvent effects only has a minor effect on the activation energy barrier and reduces it by another 1, 2, and 5 kJ/mol in pure dodecane and methanol:dodecane 50:50 and 99:1 solvent mixtures, respectively.

In $\mathbf{3''}_3$, two methanol solvent molecules form hydrogen bonds with the oxygen atom, and one methanol forms a cyclic structure acting as a hydrogen bond donor to the hemiaminal nitrogen and as a hydrogen bond acceptor of the hydroxyl group. This re-orientation is associated with a change in Gibbs free energy by 13.8 kJ/mol in the absence of an bulk polar solvent effects (and lower by 0.4, 2.3, and 4.8 kJ/mol in pure dodecane and methanol:dodecane 50:50 and 99:1 solvent mixtures, respectively).

Following the formation of $\mathbf{3''}_3$, the condensation occurs in a step-wise manner. The solvent-assisted OH^- dissociation leads to a transition state with an increase of the C$\cdots$OH, distance (from 1.42 to 2.31 Å) and an activation energy of 47 kJ/mol due to the stabilization by three strong hydrogen bonds. The activation energy for OH^- dissociation is slightly reduced by 2 kJ/mol in methanol:dodecane 50:50 and 99:1 solvent mixtures. In the intermediate $\mathbf{4}_3$, the dissociated OH^- is at 3.29 Å from the α-carbon and stabilized by the explicit methanol molecules. One of them is at 1.89 Å to the β-carbon hydrogen atom. The Gibbs free energy of $\mathbf{4}_3$ formation is 37.4 kJ/mol, which reduces by 1.4, 3.4, and 5.2 kJ/mol in pure dodecane, methanol:dodecane 50:50 and 99:1 mixtures. Proton abstraction from the β-carbon in $\mathbf{4}_3$ occurs by one methanol molecule, which is at 1.44 Å distance in the transition state. The activation energy barrier for proton abstraction is 25 kJ/mol in the absence of implicit solvent, which slightly increases by 3, 5, and 8 kJ/mol in implicit solvent.

The significant difference in the activation energies associated with both pathways suggests that, in polar hydrogen bonding solvent, the water release occurs in a step-wise rather than in a concerted fashion.

5.2.4 Free Energy Profile of Amination in Solution

Figure 5.12 illustrates the effect of explicit solvent coordination on the Gibbs free energy landscape for the amination of 1-undecanal and diethylamine (DEA) to give

(E)-N,N-diethylundec-1-en-1-amine (enamine) **5**. It is observed that the required Gibbs free energy for substrate binding decreases by 12.5 kJ/mol in solution with the inclusion of explicit solvent molecules. The barrier for nucleophilic addition decreases by 126 kJ/mol when a proton is added to the carbonyl oxygen by a two-methanol proton shuttle rather than a direct transfer. The Gibbs free energy required for hemiaminal formation decreases from -4 to -12.6 kJ/mol in solution, when considering explicit solvent coordination. In the presence of a protic solvent, hemiaminal condensation occurs through a kinetically favored step-wise pathway that reduces the activation energy by over 120 kJ/mol.

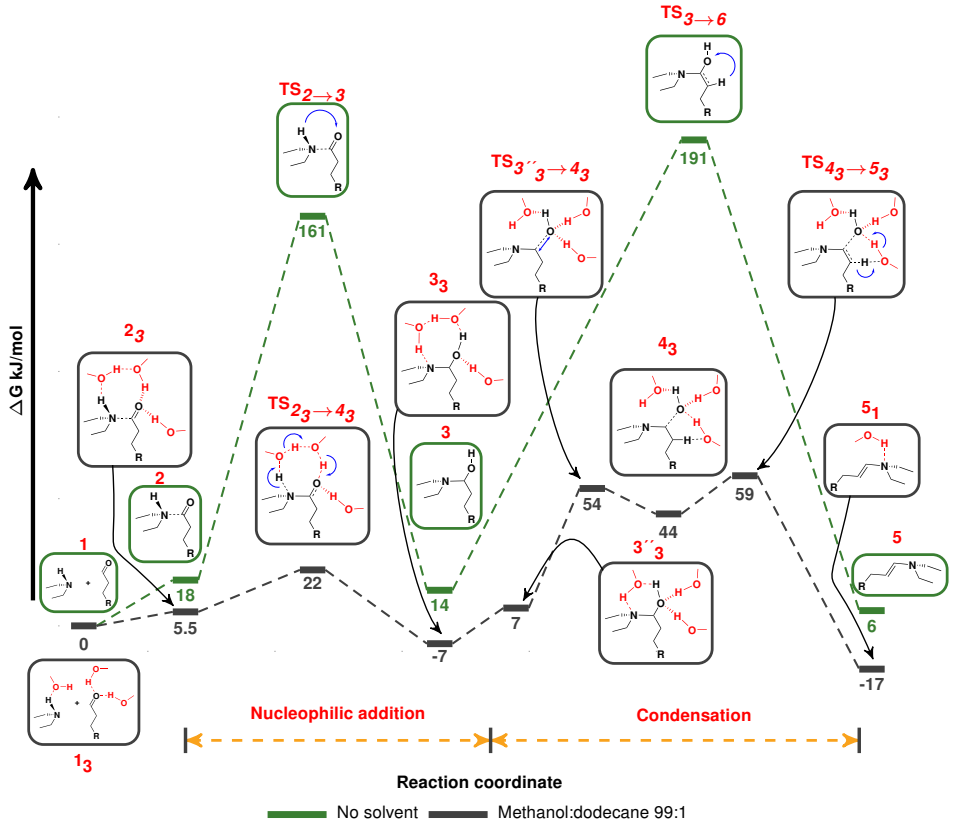

Fig. 5.12.: Gibbs free energy profile of the enamine (5) formation from 1-undecanal and diethylamine via direct (in gas phase, blue) and in methanol:dodecane 99:1 solvent mixture (dark gray): when solvent effects are calculated using a cluster-continuum solvent model. All energies are given in kJ/mol. Explicit coordination of methanol molecules significantly affects the reaction mechanism and the potential energy surface.

In summary, from the thermodynamic screening we have established that for amination, polar solvents have a superior performance than the non-polar ones. In solution, the activation energies of the transition states are only slightly reduced

when solvent effects are considered using simple implicit solvent models. To describe the solvent effect accurately, explicit substrate-solvent interactions must be considered. Figure 5.12 shows that the explicit solvent molecules alter the shape of the free energy landscape of the amination reaction. Participation of the solvent as catalyst alters the reaction path from an energetically unfavorable direct to a more feasible, step-wise pathway with low activation energies for the corresponding transition states. In solution, explicit solvent assistance flattens the overall potential energy landscape, thus effectively driving the thermodynamics and kinetics of the enamine formation.

5.3 Multi-step Solvent Screening for Rhodium-catalyzed Reductive Amination

5.3.1 Reduction of Enamine

The first step in the computer aided solvent design is to elucidate the reaction network underlying the desired chemical transformations in gas phase. All possible elementary steps involved in the rhodium catalyzed hydrogenation of enamine are depicted in Figure 5.3. For the reduction of enamine a transition metal catalyst is required. For this work, a rhodium(I)-hydride catalyst coordinated to a bidentate SulfoXantPhos (SX) ligand is employed due to its solubility in water, since water is formed as a side product during reductive amination.

Coordination Modes of Enamine

The double bond of the (E)-N,N-diethylundec-1-en-1-amine (enamine, **5**) binds to the transition metal atom of the catalyst. However, the bulky SulfoXantPhos (SX) ligand requires the substrate to adapt its conformation. Hence, the long-chain coordinating substrate must reorient to fit into the catalyst-ligand pocket. Due to its long undecyl and diethylamine chains, substrate **5** can adopt two different conformations when coordinated with **7** thus, generating complexes **8** and **8-rot** (see Figure 5.13). Complex **8** exhibits a square-planar structure with the enamine double bond positioned perpendicularly to the (P∩P)-RhH plane, while the amine group faces towards the ligand.

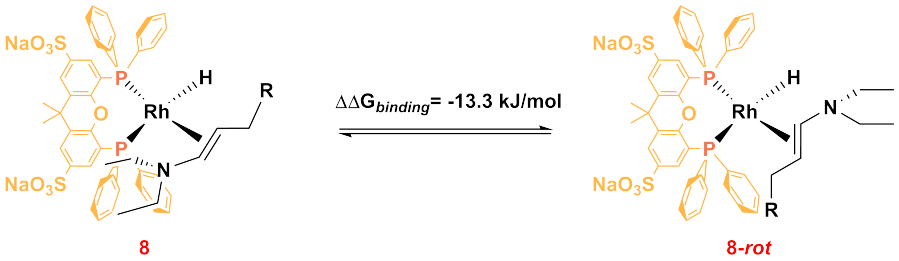

Fig. 5.13.: Enamine binding to a sterically demanding bulky (SulfoXantPhos)RhH catalyst.

In **8-rot**, the C=C double bond rotates by nearly 180 degrees, positioning the NEt_2 group to face away from the ligand and towards the solvent. The long-chain alkyl residue R is flexible enough to avoid direct contact with the SX ligand. Enamine binding is 13 kJ/mol more favorable in **8-rot**. However, a direct inter-conversion from **8** to **8-rot** is not feasible due to ligand restrictions; the substrate must dissociate and rebind to create the latter. Beyond 8 and 8-rot, no additional catalyst-substrate conformers or rotamers were identified because of the steric requirements of both the ligand and the long-chain substrate.

Identification of the Rate Limiting Step

Figure 5.14 shows the Gibbs free energy profile for the catalytic reduction of conformers **8** and **8-rot**. Since substrate coordination to **7** completes the rhodium coordination sphere, direct solvent-catalyst interactions are not possible. A rotation of the C=C double bond parallel to the H-Rh bond is necessary for the hydride migratory insertion into the enamine double bond.

Hydride migratory insertion to C_α or C_β leads to the alkylamine complexes **9-rot** or **9**, respectively. The sterically demanding SX ligand hinders C=C bond rotation (see above) which makes the hydride migratory insertion the selectivity controlling elementary step for the catalytic reduction of enamine **5**. From **8**, the hydride can only bind to C_α, while C_β migratory insertion is impossible due to the restricted C=C bond rotation. In gas phase, the activation energy barrier (**TS 8** $\rightarrow$ **9**) for hydride binding to C_β is 23.8 kJ/mol. From **8-rot**, hydride binding to C_α occurs with a lower activation energy barrier (**TS 8-rot** $\rightarrow$ **9-rot**) of 17.4 kJ/mol without considering solvation.

As a result of hydride binding, square-planar alkylamine complexes **9** and **9-rot** are generated containing beta-agostic interactions. Formation of **9** and **9-rot** is endothermic by 10.01 and 10.07 kJ/mol, respectively.

For the second reduction step, molecular hydrogen binds to the alkylamine complexes **9** and **9-rot**, thus forming square-pyramidal complexes **10** and **10-rot**, with H_2 coordinated perpendicular to the (P∩P)Rh-alkylamine. H_2 coordination is endothermic by 33.8 and 28.3 kJ/mol.

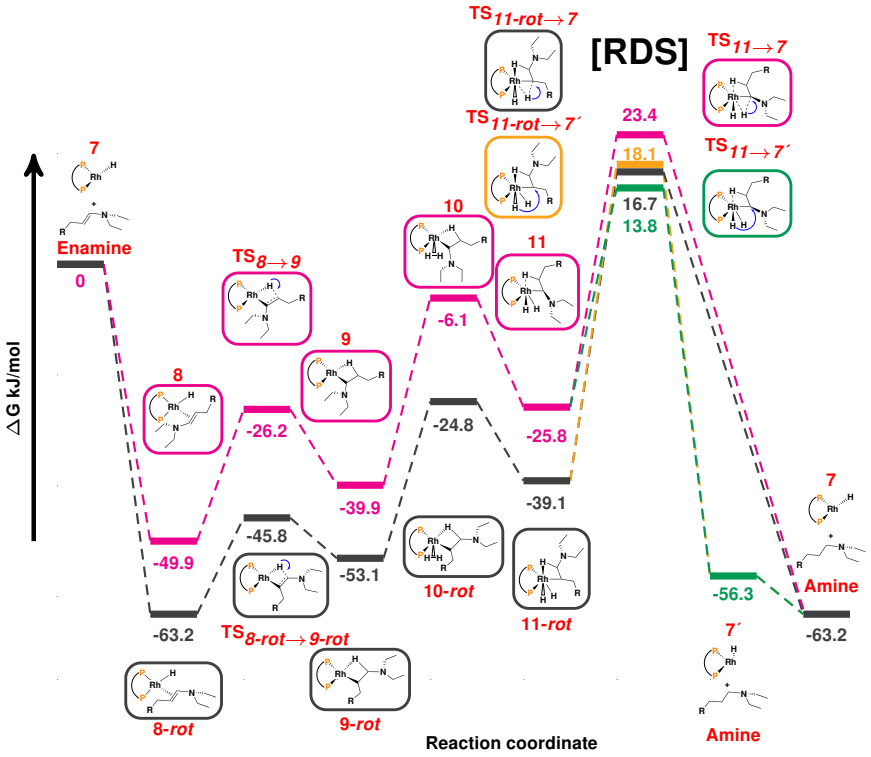

Fig. 5.14.: Gibbs free energy potential energy landscape for (SulfoXantPhos)RhH catalyzed reduction of (E)-N,N-diethylundec-1-en-1-amine in kJ/mol.

The activation energy of oxidative addition corresponds to the H-H bond splitting and the shift of the agostic interaction from the equatorial to axial plane, thus changing the coordination geometry from square-pyramidal to octahedral. Oxidative addition of H_2 to the central metal atom (**TS 10** → **11**) occurs without an energy barrier. However, **TS 10-rot** → **11-rot** occurs with a small activation energy of 2.5 kJ/mol.

As a result of H_2 oxidative addition, six-coordinate octahedral (SX)Rh-HH-(alkylamine) complexes **11** and **11-rot** are formed. The Gibbs free energy corresponding to the **11** and **11-rot** formation is –19.7 and –14.3 kJ/mol, respectively.

Finally, in the last step, the migratory insertion of the hydride to the alkylamine takes place, allowing the formation of the N,N-diethyldecylamine (Amine) product along with the catalyst regeneration.

Following each of the two intermediates **11** and **11-rot**, there are two possibilities for the reductive elimination of the final amine product (See Fig. 5.14). From complex **11**, the final product's reductive elimination can be achieved via **TS 11** $\rightarrow$ **7** or **TS 11** $\rightarrow$ **7′** by overcoming activation energy barriers of 49.2 or 39.5 kJ/mol, respectively. The first case corresponds to the migration of the axial hydride, while the second is the migration of equatorial hydride to the C_α of alkylamine. The difference in activation energies in the absence of solvent between these transition states is almost 10 kJ/mol in favor of **TS 11** $\rightarrow$ **7′**. The product from (**TS 11** $\rightarrow$ **7**) is the active catalyst **7** and the desired amine product, however latter (**TS 11** $\rightarrow$ **7′**) generates a catalytic isomer **7′**, which only upon re-isomerization recovers the active catalyst **7** ($\Delta G_{7' \rightarrow 7}$ = -6.9 kJ/mol).

A similar situation occurs in the case of complex **11-rot**, where either the axial or equatorial hydride approaches C_β of the alkylamine. The corresponding activation energies for **TS 11-rot** $\rightarrow$ **7** and **TS 11-rot** $\rightarrow$ **7′** are 55.8 and 57.2, respectively.

From Fig. 5.14, it is evident that the catalytic hydrogenation of enamine is controlled by the reductive elimination of amine, which is the rate-determining step (RDS) (i). Additionally, the the formation of **8-rot** may thermodynamically be favored (ii), but the activation energies of the rate-determining transition states ($\Delta G^\ddagger$ = 49.2 and 39.5 kJ/mol) after the formation intermediate **8** are lower compered to the activation energies for the rate-determining step ($\Delta G^\ddagger$ = 55.8 and 57.2 kJ/mol) following the formation of **8-rot** complex, in absence of solvent. Thus, it is more likely that the catalyst reduction of the enamine will proceed following the formation of intermediate **8** due to the smaller activation energy for the rate-determining transition state.

The release of the final amine product is exothermic by -24.1 and -37.4 kJ/mol in the absence of solvent.

5.3.2 Implicit Solvent Screening for Reductive Amination

Since the rate-determining step represents the slowest elementary stage in a multi-step reaction, the rate of reaction can be determined by its activation energy. A favorable solvent must decrease the activation energy of the rate-determining transition state, thus increasing the reaction rate.

Once the reaction network is resolved and the rate-determining step is located, the effect of solvents on the activation energy of the rate-limiting transition state can be calculated for a large number of solvents. We have chosen a set of 12 organic

solvents that are commonly used and have different polarities and functional groups. However, the computational cost would not significantly increase if a larger number of solvent candidates are screened. The impact of the solvent on the activation energy of the rate-limiting step can be explained by the decrease in activation energy caused by the solvent compared to that in the gas phase. This reduction is represented as $\Delta\Delta G^{\ddagger}_{solu} = (\Delta G^{\ddagger}_{solu} - \Delta G^{\ddagger}_{gas})$. If the change in Gibbs free energy of activation, $-\Delta\Delta G^{\ddagger}$, is positive, it suggests that the activation energy barrier is lower in the chosen solvent as compared to the gas phase. This indicates that the reaction rate will increase when performed in that particular solvent.

In addition to implicit solvent screening, Fabian Huxoll in the group of Prof. Gibriele Sadowski at TU Dortmund have suggested that the effect of solvent on the rate of a chemical reaction can be also be expressed by thermodynamic activities (a) of the substrates. The thermodynamic activity calculations were performed by Fabian Huxoll using the group-contribution method Modified UNIFAC(Do) at TU Dortmund. The thermodynamic activities can be defined either as the product of the mole fraction x_i and the mole fraction-based activity coefficient γ_i^x or the as the product of the concentration c_i and the concentration based activity coefficient γ_i^c (See Eq. 5.1).

$$a_i = c_i \cdot \gamma_i^c = x_i \cdot \gamma_i^x \tag{5.1}$$

Using thermodynamic activities the effect of solvent on the reactants is estimated. It is however assumed that, the reaction rate constant k does not depend on solvent as long as the transition state is not affected by the solvent. At the start of the reaction ($t = 0$), the backward reaction can be neglected therefore the rate of reaction can only be described by the $k_{forward\ reaction}$. It is thus possible to predict the solvent influence on the rate of reaction from the thermodynamic activities (See Eq. 5.2).

$$r = k_{forward\ reaction} \cdot a_{reactants} \tag{5.2}$$

Fast reaction rates and turnover frequencies can be achieved for reductive amination using the solvent with the high thermodynamic activity of the enamine. Additionally, potential solvents for the reaction are also screened and investigated based on the enamine activity ($a_{enamine}$) in solution.

Figure 5.15 shows, the reduction in the activation energy of the rate-determining transition state with Rh(I)/SulfoXantPhos as the catalyst (left axis) and thermodynamic activities of enamine (right axis), in various solvents. The reduction in activation energy of the rate-determining transition state suggests that polar solvents such as alcohols and dimethylformamide (DMF) are promising solvent candidates for the reductive amination. Non-polar solvents, such as long-chain alkanes, toluene,

and dioxane, exhibit the least reduction in the activation energy of RDS when compared to gas-phase calculations. To validate the outcomes of the implicit solvent screening, Fabian Huxoll at TU Dortmund calculated the thermodynamic activity of enamine using the same group of solvent candidates. After conducting thermodynamic activity screening, DMF, NMP (N-methyl-2-pyrrolidone), and methanol were found to be promising candidates for the RA, as in these solvents a fast conversion of the enamine to the amine is expected. Conversely, solvents with low thermodynamic activity for enamine substrates in solution, such as tetrahydrofuran (THF), toluene, and n-heptane, are expected to reduce the reaction rate and thus result in a lower yield of amines. Both implicit solvent and thermodynamic activity-based screening methods resulted in a similar ranking of solvent candidates.

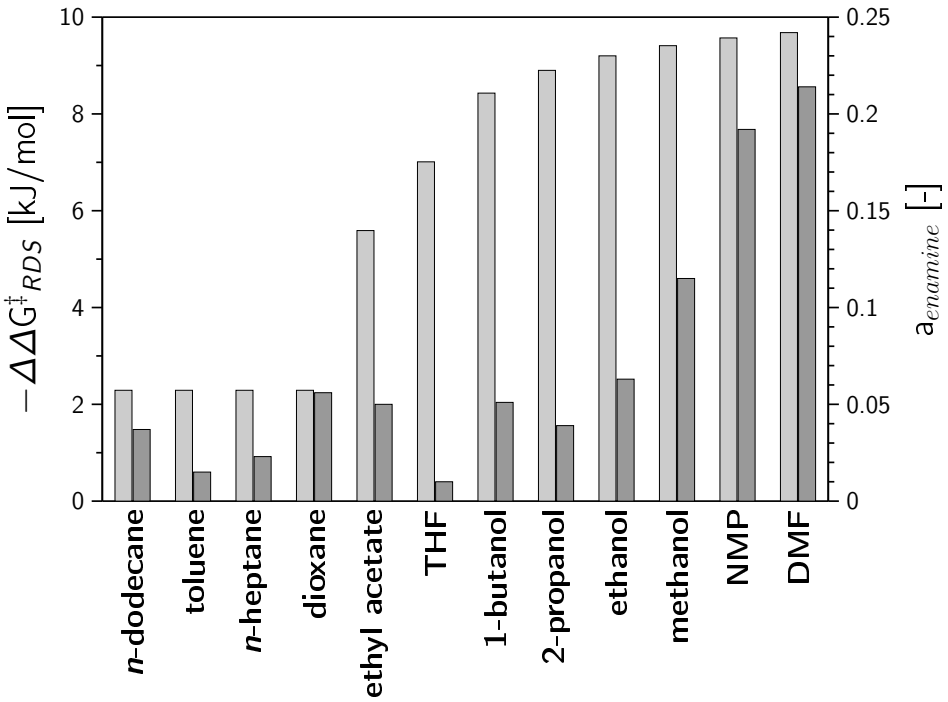

Fig. 5.15.: Calculated solvent effects on the rate-determining step; difference in Gibbs free energy of activation relative to gas-phase calculations (left axis, light gray bars). Thermodynamic activity of the enamine in 12 different selected solvents (right axis, dark gray bars).

In addition to the estimation of solvent effects on reaction rate using an implicit solvent model the effect of solvent on the Gibbs free energy of reductive amination (ΔG_r^0) was also investigated. The Gibbs free energy of reductive amination of undecanal and DEA is -57 kJ/mol at 373 K and 30 bar of pressure in gas phase. This value is in good agreement with the reaction energy of -59.7 kJ/mol for the same reactants reported by Boz et al using Møller-Plasset theory (MP2). The overall

thermodynamics of the reductive amination of 1-undecanal with diethylamine (DEA) are only marginally dependent on the polarity of the solvent by -4 kJ/mol with polar media such as DMF being preferred (see Appendix C.2).

In summary, a variety of polar and non-polar solvents were evaluated based on two performance descriptors: the reduction in activation energy of the rate-determining transition state in the solvent ($-\Delta\Delta G^{\ddagger}_{RDS}$) and the thermodynamic activity (a) of the enamine. After screening the solvents, the three best performing solvents (DMF, NMP, and methanol) were selected for further refinement. A total of twelve solvents were analyzed in the screening process.

5.3.3 Explicit Solvent Treatment

After identifying promising solvent candidates from the initial screening process, the next step is to examine the interaction between the catalyst and solvent using computationally intensive methods. To accomplish this, two solvent candidates, DMF (a polar solvent) and methanol (a polar/protic solvent capable of hydrogen bonding), were selected from the three candidates (DMF, NMP, and methanol) identified during the previous step. Catalyst-solvent interactions refer to the interactions between solvent molecules and the catalyst present in the solution. The active catalytic species (7) (SX)RhH has a vacant coordination site that can be accessed by the solvent and the substrate (Figure 5.16). To produce the amine product, the catalyst-substrate interactions need to be stronger than the catalyst-solvent interactions to allow coordination of the catalyst with the substrates (enamine and H_2). In an optimal solvent, the catalyst-solvent interaction must be weak so that it does not compete with the coordinating substrate and inhibit the catalyst.

Fig. 5.16.: Substrate and solvent coordination to the (P∩P)RhH catalyst for enamine reduction. Here, P∩P corresponds to a SulfoXantPhos ligand

Table 5.3 provides the calculated binding free energies for the enamine, H_2, and possible competitive binders, such as the selected solvents methanol and DMF. Enamine substrate shows higher binding energy to the catalyst than the solvents.

Tab. 5.3.: Substrate and solvent Gibbs free binding energies to (SX)RhH catalyst in kJ/mol at 373 K and 30 bar of pressure.

enamine		H_2	methanol	DMF	DMA	CO
8	-50	-34	-15	-41	-62	-150
8-rot	-63					

DMF on one hand due its strong binding to the catalyst competes with the reducing agent and thus would obstruct the H_2 activation. Furthermore, the thermal decomposition of DMF into CO and DMA (dimethylamine) at high temperatures [205, 206] can potentially deactivate the catalyst by making the catalytic site unavailable to the substrates. Thus, the concentration of active transition-metal catalyst available in DMF may actually be lower due to potential catalyst inhibition, which can reduce the yield of RA.

Methanol, on the other hand, is a solvent with weak coordination to the catalyst ($\Delta G_{methanol\ binding}$ = -15 kJ/mol), so the substrate can displace the solvent molecule, coordinate to the Rh catalyst, and form a tight catalyst-substrate complex **8** (See Figure 5.3). When solvent effects are taken into account using an implicit solvent model, the free energy of methanol coordination to the catalyst ($\Delta G_{methanol\ binding}$) becomes -13 kJ/mol in a non-polar dodecane and almost thermoneutral with -3 and -2 kJ/mol in methanol:dodecane 50:50 and 99:1 w/w solutions, respectively. Thus, at reaction conditions, solvent de-coordination is facile, and active catalyst species and a solvent coordinated catalyst complex are in equilibrium. This demonstrates that methanol is, therefore, a more suitable solvent for the reductive amination with desirable thermodynamic and environmental properties (See above).

The screening of solvent effects on the activation energy of RDS and resolution of catalyst-substrate and catalyst-solvent interactions has shown that methanol is a promising candidate for rhodium-catalyzed reductive amination of 1-undecanal and diethylamine. In summary, these findings suggest methanol as the preferred solvent. DMF, despite its promising results during solvent screening, is not recommended as a polar solvent due to the possibility of catalyst inhibition. Non-polar solvents, such as toluene and *n*-heptane, will result in low product yields.

5.3.4 Experimental Validation

Based on the results from the previous steps, reductive amination experiments were then carried out in different polar, polar and hydrogen bond donating, and non-polar

solvents using 1-undecanal and diethylamine as substrates by Jonas Bianga, a PhD student in the group of Prof. Dieter Vogt at TU Dortmund (Figure 5.17).

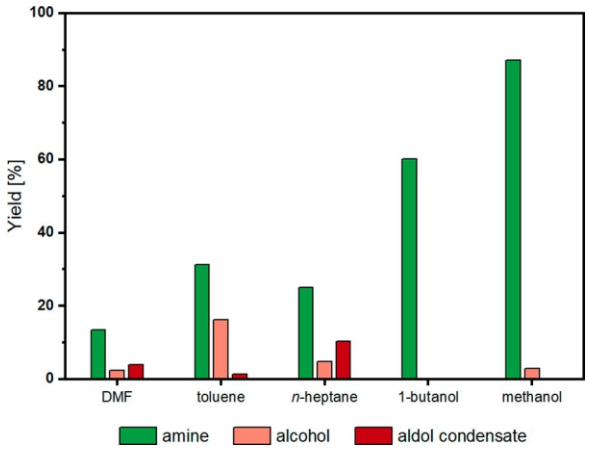

Fig. 5.17.: Experimentally determined yields for rhodium catalyzed reductive amination of 1-undecenal and diethylamine generating amine (green), alcohol (light red), and aldol condensate (dark red) as reaction products in the various solvents. Reaction conditions: pH_2 = 3.0 MPa, T = 373.15 K, t = 2 min, 500 rpm, waldehyde = 4 wt %, naldehyde/nEt2NH = 1/4, nRh = 1 mol %, Rh/ligand = 1/1. Ligand: Xantphos. Yields determined by GC-FID using external standard method. Obtained from [200].

The experimental yields of the desired amine product and byproducts (alcohol and aldol condensates) in pure solvents are presented here. DMF despite showing the largest reduction in the activation energy of the rate-determining step estimated using an implicit solvent model (See Section 5.3.2) showed the lowest yield of amine product. Upon investigation of explicit catalyst-solvent interactions, DMF was discarded as a potential solvent for reductive amination, as it potentially can cause catalyst inhibition. The highest yields of the amine product were achieved in methanol and butanol. Small amounts of alcohol were formed as side product as no aldol condensates were detected.

These results confirm the findings of the computational solvent screening which suggest that reductive amination of aldehydes is more favorable in short-chain alcohols, specifically methanol, compared to other solvents. The negative impact of solvents, such as toluene and n-heptane, becomes evident due to the high amount of byproduct formation and lower overall yield when compared to methanol. These findings provide evidence that the method for screening solvents, as described in this work, is suitable for generating a list of promising solvent candidates for the reductive amination reaction of 1-undecanal and diethylamine (DEA).

5.4 Conclusions for Computer-Aided Solvent Selection

Multiple roles of the solvent in rhodium-catalyzed reductive amination were identified, including stabilization of reaction intermediates and transition states, and its function as a co-catalyst and catalyst inhibitor. These findings were established through a thorough mechanistic elucidation process. Effect of properties such as solvent polarity, ability to form hydrogen bonds with reaction species, participation as co-catalyst, explicit substrate-solvent and catalyst-solvent interactions were showen to have significant effects on the kinetics and thermodynamics of the reaction.

To find optimal solvents for metal-catalyzed reactions, a solvent screening workflow was proposed where at first the reaction mechanism is resolved including all possible intermediates and transition states in the absence of solvent to find the rate-determining step. Later a number of solvent candidates are screened based on the effect solvent polarity on the activation energy of the rate-determining step followed by the explicit solvent treatment for only the best performing solvent candidates. Finally, the model-predicted solvent candidates can be tested by experiments.

During amination, explicit solvent coordination significantly promotes the substrate (1-undecanal and DEA) binding by increasing the electrophilicity of the carbonyl carbon atom. The activation energies of nucleophilic addition and condensation are only slightly reduced when the effect of solvent are estimated using an implicit solvent model. A hydrogen bond donating solvent such as methanol can participate in the reaction as a proton transfer agent. An optimum of three explicit methanol molecules can directly interact with substrates and transition states, fully completing the first solvation shell. The inclusion of explicit solvent participation significantly reduces the activation energies. The solvent molecules play an active role in facilitating the enamine formation by driving the water elimination reaction via a step-wise, rather than a concerted mechanism.

In the transition metal-catalyzed reduction step, solvent may compete with the reaction substrates (enamine and H_2) to occupy the free coordination site at the catalyst. A favorable solvent should exhibit weak catalyst-solvent interaction so it can be easily displaced by the coordinating substrates. The final reductive elimination step of the amine product is rate-limiting step. The hydride approaching C_α instead of C_β of the alkylamine intermediate is kinetically favored. With reductive elimination as the rate-determining step, the control of the kinetics of this elementary step can drive the yield of the entire process.

After the complete mechanism elucidation (Step 1), effect of a number of solvent candidates was examined to find an optimal solvent for reductive amination via the multi-step solvent screening approach considering the reduction in activation energy of the rate-determining step in solvent (Step 2). The rapid solvent screening (Step 2) significantly reduced the vast number of solvent candidates. Then, we estimated solvent-catalyst interactions through explicit solvent treatment (Step 3). As a result, DMF can be dismissed as a solvent due to its potential to deactivate the catalyst and its inability to form hydrogen bonds with the substrates. Batch experiments conducted at TU-Dortmund confirmed these findings. The experiments revealed that DMF, toluene, and n-heptane are unsuitable solvents for the reductive amination of 1-undecanal and diethylamine, as they produce high amounts of byproducts. Of the solvents tested, methanol, particularly short chain alcohols, is the optimal choice for reductive amination (Step 4). In addition to providing superior catalytic performance, methanol is also a more environmentally friendly option in terms of green chemistry, while DMF is often considered "hazardous" [43, 207].

In conclusion, this multi-step solvent screening workflow enables quick *in-silico* solvent screening without the need of any prior experimental data. This generally applicable workflow can serve as a robust tool to select optimal solvents for homogeneously catalyzed multi-step reactions and significantly reduce time-consuming experimental solvent screening.

6

Effects of Ligand and Gas Composition on Rhodium-Catalyzed Hydroaminomethylation of Long-Chain Olefins

This chapter discusses the combination of hydroformylation (Hyfo) and reductive amination (RA), also known as hydroaminomethylation (HAM), of long-chain olefins obtained from renewable sources. The ultimate objective is to produce secondary amines (Figure 6.1). This investigation utilizes quantum chemical calculations to refine the mechanistic reaction kinetic model for the HAM of 1-decene in a thermomorphic multiphase solvent (TMS) system consisting of methanol and dodecane. By examining the detailed reaction mechanism, including the impacts of ligand, solvent, and reactant gas composition, it addresses limitations in the current kinetic model, resulting in an improved model.

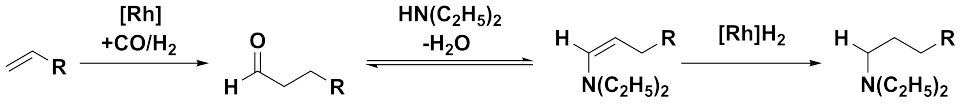

Fig. 6.1.: Conversion of olefins to amines in the presence of synthesis gas (CO /H_2), an amine substrate (in this case diethylamine) and a transition metal catalyst by hydroaminomethylation (HAM).

Kortuz et al. [95] proposed a mechanistic kinetic model for the HAM reaction of 1-decene in a methanol:dodecane TMS by combining the kinetic models of Jörke et al. [187] and Kirschtowski et al. [13] for the underlying hydroformylation of 1-decene and reductive amination of 1-undecanal, respectively. It is important to note that the RA-system of Kirschtowski et al. [13] differs from the Hyfo system of Jörke et al. [187] in terms of solvent system, ligand and reactant gas composition: where Hyfo was carried out in the presence of syn gas (CO/H_2) in DMF:dodecane solvent mixture and RA was performed under high pressure of H_2 gas only in methanol:dodecane solvent mixture. During the hydroaminomethylation of styrene and piperidine in the presence of syngas in THF solvent using a rhodium catalyst with a diphosphine ligand, Crozet et al., confirmed the formation a (P∩P)RhH-CO catalyst using NMR

spectroscopy [100]. In order to find an effective TMS for HAM, with the aim of an efficient post-reaction catalyst recovery, Bianga et al. have shown experimentally that the hydroaminomethylation reaction (Hyfo + RA) cannot be carried out in DMF and have proposed methanol as an alternative instead [208]. However, due to the low solubility of BiPhePhos (BPP) in water, it is also not recommended for HAM. Instead, a water-soluble SulfoXantPhos (SX) was used for the HAM experiments [95, 208, 209]. Kortuz et al. [95] not only formulated the kinetic model for HAM based on these previous contributions, but also performed a heuristic set of experiments for reparametrization of the pre-existing kinetic model. Later Kortuz et al. [209], have extended the kinetic model to include a mechanistic formulation of the final hydrogenation step, allowing for a detailed mechanistic description. The experiments in both papers focused primarily on the effects of temperature, pressure, and solvent system. In a recent contribution, Rätze et al. [210] investigated HAM of 1-decene in methanol:dodecane solvent mixtures to refine the kinetic parameters reported previously by Kortuz et al. Five HAM experiments were performed. Where the effect of the gas phase concentration on reaction kinetics was investigated. In addition, kinetic parameters for HAM were re-estimated using the parameters from the kinetic model of Kortuz et al., as initial guess.

To overcome the uncertainties and simplifications in the existing kinetic models for HAM proposed by Wieland et al. [209] and Rätze et al. [210], this chapter aims to resolve the effects on HAM kinetics by systematically considering a number of parameters, such as the change in ligand, gas phase composition, and particularly the effect of solvent. The effect on the kinetics of Hyfo by changing the coordinating bidentate ligand from BiPhePhos (BPP) to SulfoXantPhos (SX) in solution are investigated in the first part of this chapter. The choice of solvent mixture is based of the kinetic experiments driven by the computational solvent screening (See Chapter 5). The effect of reactant gas composition on the kinetics of hydrogenation will be resolved in the latter part.

6.1 Ligand Effects on Hydroformylation

The complete catalytic cycle of hydroformylation was taken from Chapter 4 and was re-estimated using SX as a bidentate coordinating ligand. Table 6.1 shows the effect of the choice of ligand BPP and SX, and solvent composition on the activation of the catalyst upon CO dissociation. The energy required for CO dissociation increases by almost 17 kJ/mol when an electron-donating SX ligand is used.

Tab. 6.1.: Gibbs free energies of CO dissociation from the catalyst resting state in kJ/mol.

			Methanol:dodecane composition				
	lig.	**Gas phase**	**Methanol**	**(70:30)**	**(50:50)**	**(30:70)**	**Dodecane**
$\Delta G_{CO\ diss.}$	**BPP**	84.2	83.8	83.7	84.2	84.6	85.3
	SX	101.4	104.9	105.4	105.6	106.1	106.3

The high CO dissociation energy from the pre-catalyst can be attributed to the electronic properties of the catalytic ligand. The natural charge analysis shows higher electron density on the phosphorous atoms of the electron-donating SX ligand compared to the electron with-drawing BPP ligated rhodium catalyst (See Figure 6.2). Upon CO dissociation, the partial charge on the central rhodium atom increase from -0.31 to -0.40 for BPP catalyst, however the electron density on the rhodium atom for SX catalyst remains almost unchanged (-0.23 in **1**** and -0.24 in **1**). In addition, upon CO dissociation the partial charge on the hydride atom also increases by 0.11 and 0.8, for BPP and SX catalysts, respectively. The increase in the CO dissociation energy due the change in ligand, significantly affect the amount of active catalyst present in the reaction mixture, since the thermodynamic equilibrium shifts towards the pre-catalyst side.

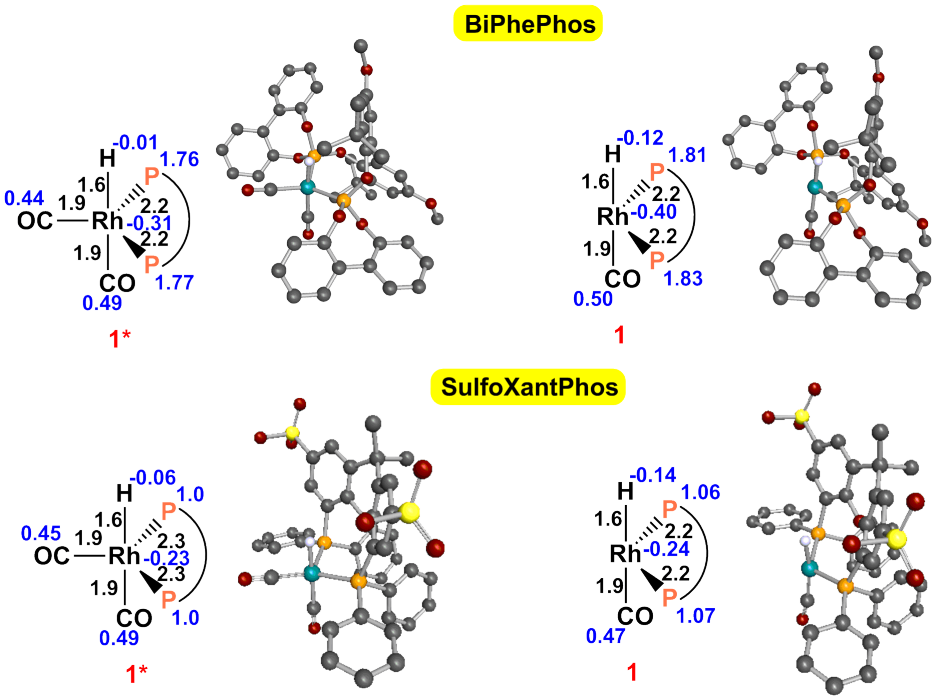

Fig. 6.2.: Conversion of the pre-catalyst **1*** to the active catalyst **1** via CO dissociation. Hydrogen atoms from the ligand were are omitted for clarity. Bond distances (black) are given in Angstroms; NPA charges are given in blue.

This is in agreement with several previous studies suggesting that electron-withdrawing ligands accelerate hydroformylation by facilitating CO dissociation (catalyst activation) [211–213]. A significant increase in the CO dissociation constant $K_{CO\ diss.}$ from 5500 to 82305 was also reported by Rätze et al., when an electron withdrawing ligand BPP is substituted with an electron donating SX ligand during hydroformylation [210]. This large change in the thermodynamic equilibrium constant corresponds to an increase of almost 10 kJ/mol in the Gibbs free energy of CO dissociation at 378 K and 20 bar (experimental conditions for hydroformylation). The solvent has only a marginal effect on the catalyst activation energy for BPP and SX modified rhodium catalysts.

Figure 6.3 shows the Gibbs free energy differences for all elementary steps in the hydroformylation reaction cycle including the formation of desired linear aldehydes and possible side products with BPP and SX catalysts in the gas phase and in a methanol:dodecane 50:50 solution. The solvent composition corresponds to the methanol:dodecane solvent system used during the HAM experiments conducted by Kortuz et al. [95, 209] The bidentate ligand has a strong influence on the overall hydroformylation process, with catalyst activation being the most ligand-sensitive reaction step (See above).

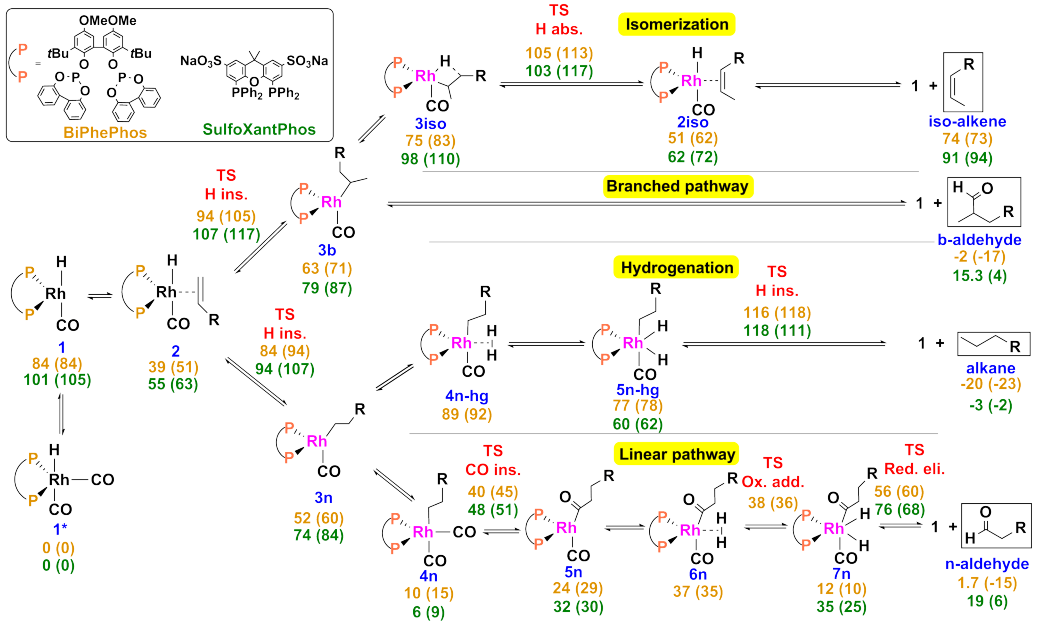

Fig. 6.3.: Gibbs free energy differences for the elementary steps of hydroformylation of 1-decene forming 1-undecanal via the linear pathway, isomerization of substrate and alkane formation after hydrogenation using BPP (orange) and SX (green) catalyst in gas phase and methanol:dodecane 50:50 solution. Values in the parenthesis corresponds to the free energy differences in solution. The thermodynamic corrections were calculated at 378.15 K and 20 bar.

Upon the olefin coordination, electron density shifts from rhodium to the coordinated double bond (see Figure 6.4), thus increasing the partial negative atomic charges on the alpha and beta carbon atoms and slightly elongates the C=C double bond by 0.1 Å when compared to free 1-decene. The coordination of 1-decene to the BPP catalyst is exergonic by -45.6 kJ/mol and for SX-catalyst by -46 kJ/mol. For BPP catalyst, the Gibbs free energy of 1-decene coordination to the catalyst **1*** ($\Delta G_{1 \rightarrow 2}$) is 13 kJ/mol lower in solution than in gas phase. However, for the electron-donating SX catalyst, the reduction in the Gibbs free energy of the 1-decene binding is only 3 kJ/mol when the effects of solvent are taken into account.

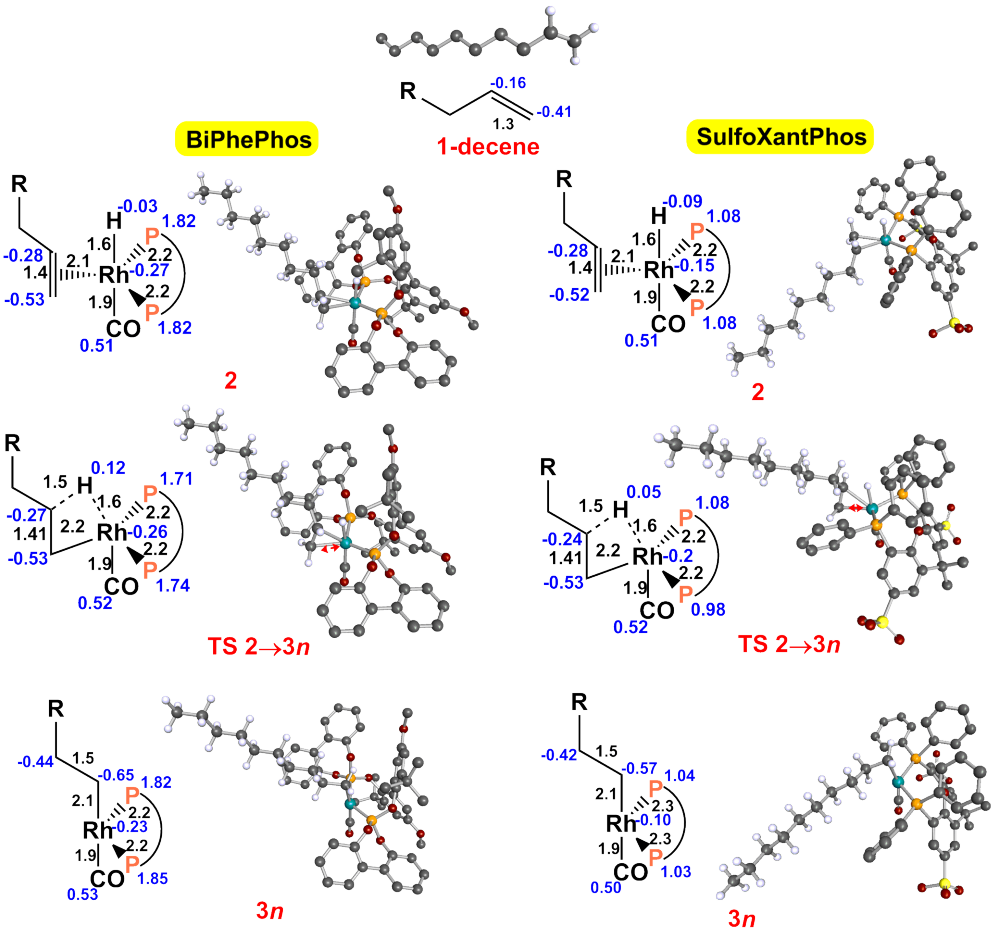

Fig. 6.4.: Structural and charge distribution details of the 1-decene coordination to Rh catalyst **2**, migratory hydride insertion into C=C double bond (TS **2** → **3n**) and the rhodium-alkyl formation in the presence of BPP and/or SX catalysts. Hydrogen atoms from ligand are omitted for clarity. Bond distances (black) are given in Angstroms; NPA charges are given in blue.

During the hydride insertion transition state, using BPP ligated rhodium catalyst, the electron density from the hydride shifts to the phosphorous atoms of the bidentate

ligand. As a result the partial charge on the inserting hydride changes from -0.03 to +0.12. The partial atomic charge on the central rhodium atom remains almost unchanged. However, when SX catalyst is used the electron density shifts from hydride to rhodium catalytic center as the partial charge on rhodium increases from -0.15 to -0.2 and the charge of the inserting hydride changes from -0.08 to +0.05 (See Figure 6.4). This results in a slight reduction of almost 6 kJ/mol (45.2 kJ/mol and 39.6 kJ/mol for BPP and SX catalyst, respectively) in the activation energy for hydride insertion when SX catalyst is used. However, when the solvent effects are taken into account, for both BPP and SX catalyst, the hydride insertion proceeds with an activation energy of 43 kJ/mol.

The Gibbs free energy for Rh-alkyl formation ($\Delta G_{2 \rightarrow 3n}$) is 6 kJ/mol higher for the SX-Rh catalyst (19 kJ/mol) than for the Rh-BPP catalyst in gas phase. The Gibbs free energy for the formation of the Rh-alkyl complex **3n** increases slightly from 19 kJ/mol in the gas phase to 21 kJ/mol when solvent effects are considered for the SX catalyst.

Similarly, the Gibbs free energy of CO coordination to the Rh-alkyl complex ($\Delta G_{3n \rightarrow 4n}$) is again 12 kJ/mol higher when SX is used as the catalytic ligand. The natural population analysis (NPA) revealed that the increase in CO binding energy stems from the reduced electron density on the central rhodium atom when SX catalyst is used for hydroformylation, i.e. -0.16 in (BPP)Rh(alkyl)(CO) and -0.08 in (SX)Rh(alkyl)(CO) **4n** complexes (See Figure 6.5). CO coordination to the SX-Rh alkyl complex is facilitated by 6 kJ/mol in the solvent (-68 kJ/mol in the gas phase versus -74 kJ/mol in solution).

An activation energy of 29.4 kJ/mol is required for the insertion of CO into the Rh-alkyl bond ($\Delta G^{\ddagger}_{4n \rightarrow 5n}$), when an electron-withdrawing BPP ligand is used for hydroformylation. However, with an electron-donating SX ligand, the activation energy for CO insertion in the gas phase increases by almost 13 kJ/mol (42.3 kJ/mol). The activation energy of CO insertion into Rh-alkyl bond is independent of solvent composition.

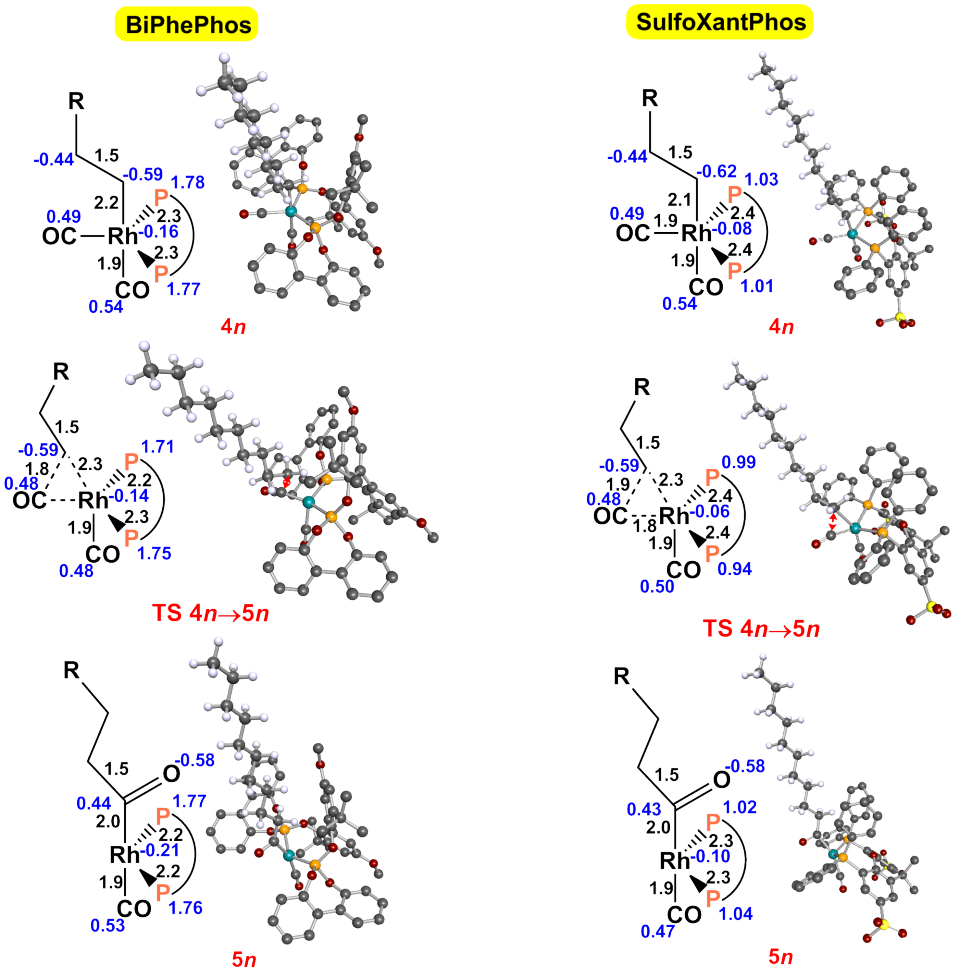

Fig. 6.5.: Structural and charge distribution details of CO coordination (**4n**) and intramolecular insertion of CO (TS **4n**→**5n**) to the give the undecyl complex **5n** using BPP and SX ligated rhodium catalysts. Hydrogen atoms from ligand are omitted for clarity. Bond distances (black) are in Angstroms; NPA charges are given in blue.

Hydrogen activation by oxidative addition at the metal center proceeds with an almost negligible activation energy of 1 kJ/mol for BPP catalyst. No transition state could be optimized for the SX-ligated rhodium catalyst despite several efforts, since the oxidative H_2 addition for the SX catalyst probably proceeds without an energy barrier.

For BPP catalyst, the Gibbs free energy associated with the oxidative H_2 addition (**6n**→**7n**), is endergonic in the gas phase (+3 kJ/mol) and becomes exergonic in solution, i.e. (-10 kJ/mol).

The activation energies for reductive product elimination with BPP and SX catalysts are 43.9 and 41.4 kJ/mol, respectively in the absence of solvent. During the

transition state, the electron density shifts from the hydrogen atoms and rhodium center to the ligand phosphorous atoms (See Figure 6.6).

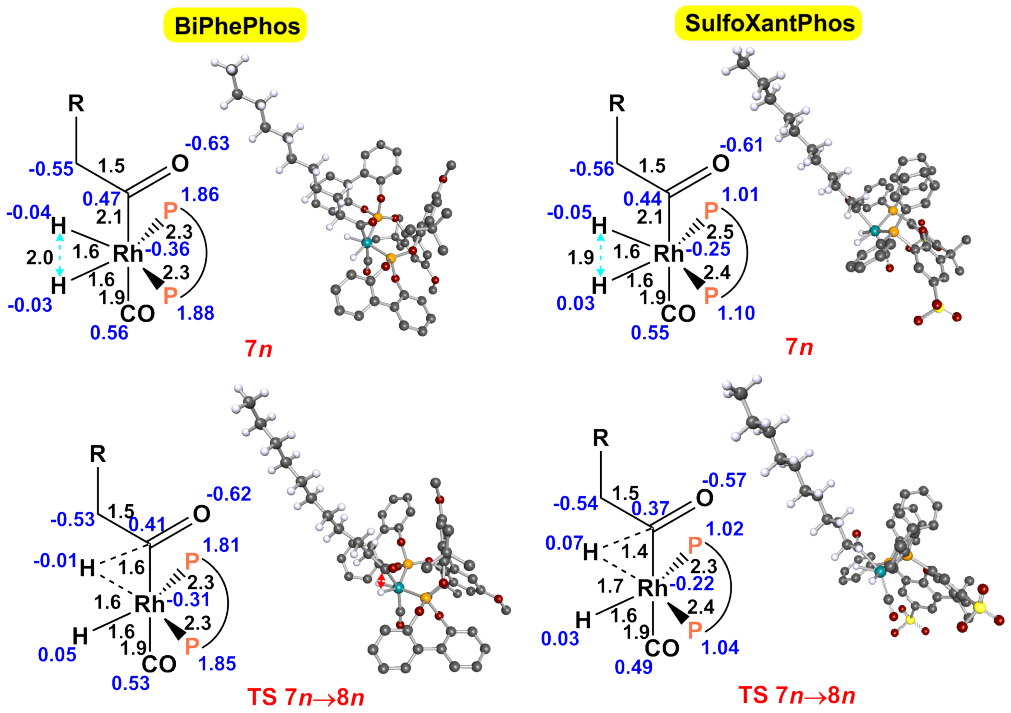

Fig. 6.6.: Structural and charge distribution details of the reductive elimination transition state, where H is inserted into Rh-C bond releasing the final aldehyde product and regenerating the active catalyst **1** using BPP and SX ligated rhodium catalysts. Hydrogen atoms from ligand are omitted for clarity. Bond distances (black) are in Angstroms; NPA charges are given in blue.

In addition, the charge on the C_α atom is reduced from 0.47 to 0.41 for BPP and 0.44 to 0.37 for SX in the transition state when compared to **7n** complex. For BPP catalyst, the activation energy for reductive elimination of aldehydes increases by 6 kJ/mol in solution compared to the gas phase. Similarly for SX catalyst system, the activation energy of reductive elimination of undecanal in solution is only 2 kJ/mol higher than the activation energy calculated without the presence of solvent.

Table 6.2, shows the activation energies of transition states along the linear hydroformylation pathway for both BPP- and SX-ligated rhodium catalysts in gas phase and in solution.

Tab. 6.2.: Gibbs free activation energies in the gas phase and in 50:50 methanol:dodecane solution (in parenthesis) for the transition states occurring along the linear hydroformylation pathway. Gibbs free energies are given in kJ/mol, with respect to the intermediate before the transition state. The thermodynamic corrections were calculated under the experimental reaction conditions of 378 K and 20 bar.

lig.	**Hydride ins. 2 → 3n**	**CO ins. 4n → 5n**	**H_2 ox. add. 6n → 7n**	**Aldehyde red. eli. 7n → prod.**
BPP	45 (43)	29 (30)	1 (1)	44 (50)
SX	40 (44)	42 (42)	-	41 (43)

For BPP, the highest activation energy in solution is the product reductive elimination i.e, 50 kJ/mol. However, with the activation energy of 44 kJ/mol, hydride insertion is slowest elementary step when an electron donating SX catalyst is used. In addition, the activation energy for CO insertion is 12 kJ/mol higher for SX catalyst than for BPP catalyst.

Similar to the BPP catalyst (See Chapter 4), for SX catalyst, hydride insertion into the C=C bond is again the highest point in the linear hydroformylation reaction cycle compared to the catalyst resting state **1*** (overall activation energy) and when solvent effects are taken into account, the overall activation energy ($\Delta G^{\ddagger}_{\mathbf{1^*}\rightarrow \mathbf{TS\ 2\rightarrow 3n}}$) increases by 12 kJ/mol (94 kJ/mol in the gas phase versus 106 kJ/mol in methanol). This calculated activation energy agrees very well with the previously reported activation energy of 104 kJ/mol for the hydroformylation of 1-octene catalyzed by an electron donating (XantPhos)RhH-CO catalyst system using CCSD(T) calculations [82].

For SX catalyst system, there exist a difference of almost 10 kJ/mol (107 kJ/mol vs. 117 kJ/mol in solution, see Figure 6.3) between the activation energies for the olefin insertion leading to the complex **3n** i.e., linear pathway and complex **3b**, branched pathway, that yields a selectivity of 97:3 (linear:branched) over branched aldehydes in solution. Thus, BPP and SX catalyst have the same selectivity towards the linear aldehydes. This indicates that the selectivity of the catalysts towards the desired linear aldehydes in hydroformylation depends on the geometrical properties of the ligands and not on the electronic properties, since monodentate ligands are known for high activities but rather low selectivities for hydroformylation [66, 71, 214]. The overall activation energy for hydrogenation following the formation of the Rh-alkyl complex **3n** is nearly 7 kJ/mol lower when a SX catalyst is used compared to a BPP catalyst (see Figures 6.3 and 4.12), showing that the electron-donating SX ligand accelerates hydrogenation compared to the electron-withdrawing BPP catalyst.

In summary, the electron-withdrawing BPP phosphite ligand drives the hydroformylation reaction via a low energy pathway, ensuring higher yield and productivity compared to an electron-donating SX catalyst. The catalyst activation strongly depends on the electronic properties of the coordinating bidentate ligand, as the CO dissociation energy increases by 21 kJ/mol in solution. This shows that in a catalytic mixture, when an electron donating SX catalyst is used, the amount of active catalyst is significantly lower due to larger $K_{CO\ dissociation}$ than in the BPP catalyst system. Therefore, a large amount of rhodium is required to obtain the same amount of active catalyst compared to the BPP catalyst system. Moreover, the overall activation energy required for hydroformylation increases by 13 kJ/mol for the SX catalyst compared to the BPP catalyst in methanol:dodecane solution, indicating that the hydroformylation rate is lower when (SX)RhH-CO catalyst is used. Rätze et al. have also reported an increase of 13 kJ/mol in the activation energy of hydroformylation of 1-decene when BPP ligand is exchanged with the SX ligand [210]. The difference in catalytic activity of BPP and SX catalyst systems was also confirmed experimentally by Ternel et al. [215], who studied the hydroformylation of methyl 10-undecenoate using BPP as catalyst in toluene as solvent, and Gaide et al. [216] studied the hydroformylation of the same substrate using SX as catalyst in water:1-butanol 50:50 solution. A high turnover number (TON) in the range of 2000-3500 h^{-1} was reported for BPP, while a turnover number as low as 1500 h^{-1} was obtained for the SX catalyst. The high TOF points towards the superior performance of BPP catalyst over the SX catalyst for hydroformylation reaction. However, during HAM since, water is formed as a by-product and due to its poor solubility in water, BPP catalyst is not recommended [180]. Therefore, despite the low reaction rates, a water soluble SX catalyst is recommended due to its selectivity (linear:branched 97:3) towards the desired linear aldehydes (See above). The formation of water during HAM not only affects the ligand selection but also influence the post reaction phase separation in methanol:dodecane TMS system. Therefore, the water formed during HAM should be constant removed using either distillation or nano-filtration to avoid negative influence of the reaction performance and to avoid phase separation in the reactor [217].

6.2 Transition from Hydrogen to Synthesis Gas for Rhodium-catalyzed Enamine Reduction

Faßbach et al. have investigated the effects on syngas composition, ligand, and reaction conditions i.e. temperature and pressure on the rhodium-catalyzed hy-

droaminomethylation of olefins in solution [117, 218]. The experiments have shown that, during HAM, high CO concentrations in syngas promotes the hyfo step, since catalyst activation occurs via CO dissociation and CO also acts as a substrate during the reaction. Excess H_2 in syngas leads to high activity for the hydrogenation of enamine. Moreover, when different syngas compositions were studied for HAM using 1-octene as olefins substrate, the highest yields of amines were obtained when a threefold excess of hydrogen was used in syngas in 1-butanol:water 50:50 solution [117].

From high pressure NMR experiments of rhodium-catalyzed HAM of styrene and piperidine Crozet et al. have reported that the active catalyst for hydroformylation and reductive amination is the same [219]. However, in the kinetic model of HAM reported by Kortuz et al. [95, 209], the kinetic parameters for the catalytic hydrogenation of enamine were initially taken from the reductive amination model of Kirschtowski et al. [13], where catalytic reduction is carried out in the presence of only hydrogen rather than syngas. To refine the HAM kinetic model, it is therefore necessary to investigate the effect of syngas on the active catalytic species and thereby on the kinetics of enamine reduction. The catalyst preparation procedure for enamine reduction was the same for both RA and HAM experiments [13, 101]. The only exception was the change in gas composition. The active catalyst is generated by heating a mixture of catalyst precursor Rh(acac)(COD) and ligand (SX) in the presence of either pure hydrogen or synthesis gas, where (SX)RhH (**7**) catalyst is generated in the former and (SX)RhH-CO (**7-CO**) catalyst in the latter case (See Figure 6.7).

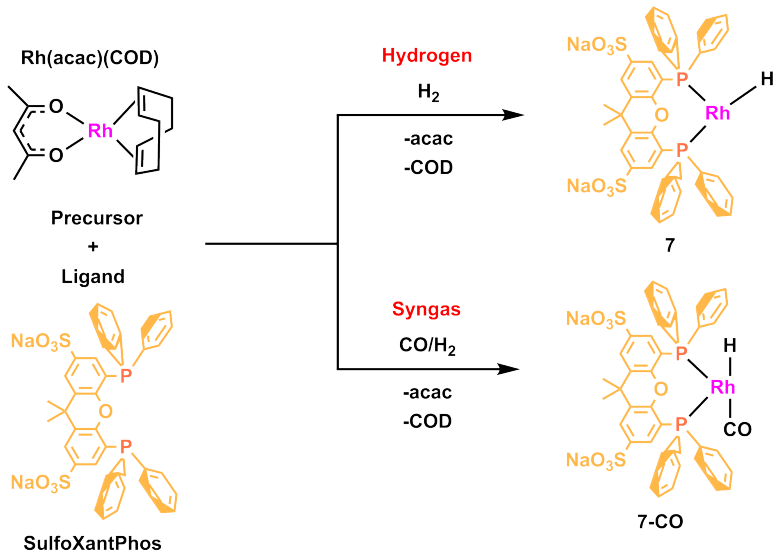

Fig. 6.7.: Formation of the active catalyst for enamine reduction in the presence of hydrogen (**7**) and syngas (**7-CO**).

In the following, the Gibbs free potential energy surface for the catalytic hydrogenation of enamine with (SX)RhH-CO catalyst is discussed (Figure 6.8). Later a comparison between the Gibbs free energy profiles of catalytic hydrogenation with (SX)RhH (**7**) and (SX)RhH-CO (**7-CO**) is presented (See Figure 6.9).

6.2.1 Hydrogenation of enamine with (SX)RhH-CO catalyst

The reaction follows the same mechanism described in chapter 5.1. The active catalyst **7-CO** react with the enamine to form a [(SX)RhH-CO-enamine] complex, referred to as **8-CO**, where the enamine and bidentate SX ligand occupy the equatorial plane, while H and CO are present at the axial positions. Figure 6.8 shows the Gibbs free energy profiles for amine formation by catalytic hydrogenation of enamine.

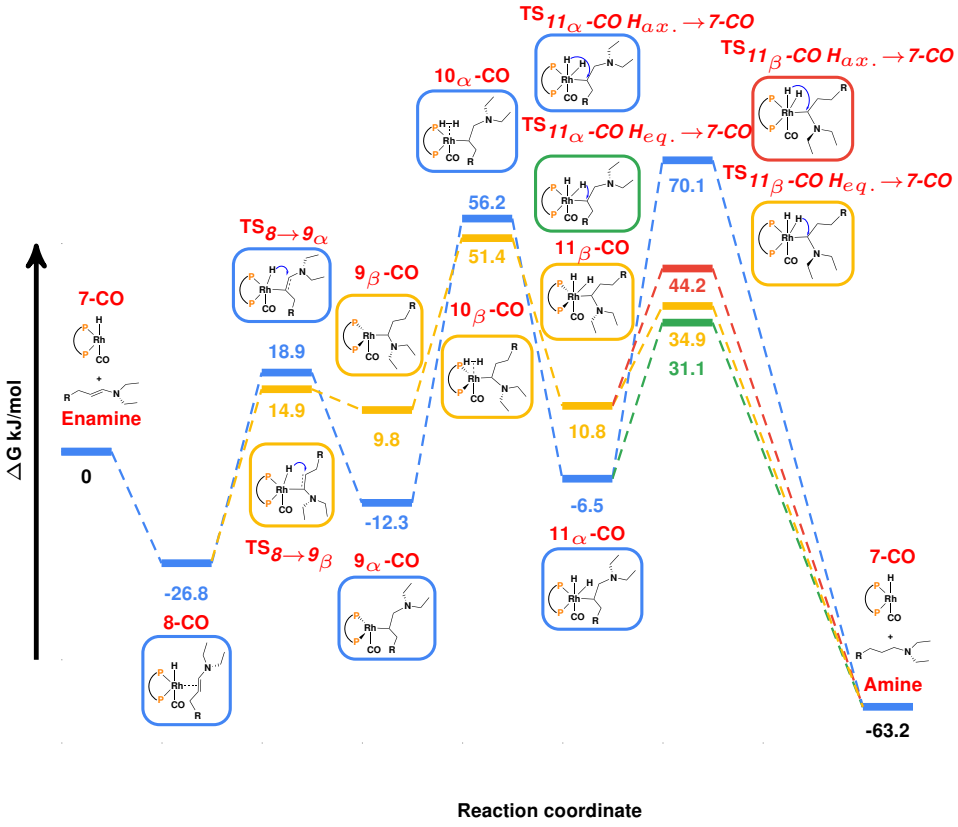

Fig. 6.8.: Gibbs free energy potential energy profiles for (SulfoXantPhos)RhH-CO catalyzed reduction of (E)-N,N-diethylundec-1-en-1-amine (enamine) in kJ/mol. Hydride migration to C_α and C_β leading to intermediate **9_α-CO** and **9_β-CO** are shown in blue and yellow, respectively. The green and red energy profiles refer to the product formation by migratory insertion of hydride at equatorial and axial positions within complexes **11_α-CO** and **11_β-CO** into the Rh-C bond, respectively. The thermodynamic corrections were calculated at 373.15 K and 30 bar.

Coordination of enamine to the active catalyst **7-CO** leads to the formation of the intermediate **8-CO** and is an exergonic process ($\Delta G_{7-CO \rightarrow 8-CO}$ = -26.8 kJ/mol). This is consistent with the enamine coordination energy of -22.6 kJ/mol reported by Crozet et al. [100]

Once **8-CO** is generated, insertion of the hydride into the C-C double bond of enamine substrate proceeds via a four-membered transition state in which hydride can either migrate to C_α or C_β, resulting in **9**$_\alpha$**-CO** and **9**$_\beta$**-CO**, respectively. The corresponding activation energies for the insertion process are ($\Delta G^{\ddagger}_{8-CO \rightarrow 9-CO_\alpha}$) 45.7 kJ/mol and ($\Delta G^{\ddagger}_{8-CO \rightarrow 9-CO_\beta}$) 41.7 kJ/mol. The formation of both **9**$_\alpha$**-CO** and **9**$_\beta$**-CO** relative to **8-CO** is inherently endergonic ($\Delta G_{8-CO \rightarrow 9_\alpha-CO}$ = 14.5 and $\Delta G_{8-CO \rightarrow 9_\beta-CO}$ = 36.6 kJ/mol) and leads to distorted octahedral geometries (for structural details see Figure 6.10).

The following process in the reaction sequence corresponds to the coordination of H_2 to form a dihydrogen intermediate (**10**$_\alpha$**-CO** and **10**$_\beta$**-CO**) and the subsequent oxidative addition of the latter to form the dihydrido species (**11**$_\alpha$**-CO** and **11**$_\beta$**-CO**). The coordination of H_2 is endergonic for both pathways 68.5 and 41.6 kJ/mol, respectively, whereas oxidative addition corresponds to a barrierless process. The high energy of H_2 coordination to alkylamine complexes is consistent with the coordination energies of 77 and 45 kJ/mol reported by Crozet et al. [100] The corresponding **11**$_\alpha$**-CO** and **11**$_\beta$**-CO** complexes adopt an octahedral geometry with the hydride and carbonyl groups in the axial positions. The oxidative addition of dihydrogen is an endergonic process in both cases ($\Delta G_{10_\alpha-CO \rightarrow 11_\alpha-CO}$ = 5.8 and $\Delta G_{10_\beta-CO \rightarrow 11_\beta-CO}$ = 1 kJ/mol, respectively).

Finally, in the last step, the migration of a hydride to the alkylamine (**11**$_\alpha$**-CO** and **11**$_\beta$**-CO**) takes place, allowing the formation of the amine product together with the regeneration of the catalyst. From each of these intermediates, there are two possibilities for the final hydride insertion, where either an equatorial or an axial hydride can be inserted into the Rh-alkylamine bond. Following the **11**$_\alpha$**-CO** intermediate, the activation energy for an equatorial hydride insertion is 37.6 kJ/mol in the absence of solvent, while the activation required for the axial hydride insertion is 39 kJ/mol higher (i.e. 76.6 kJ/mol) than for the equatorial hydride migration to C_β. Similarly, equatorial and axial hydride insertion proceed according to the **11**$_\beta$**-CO** with activation energies of 24.1 and 33.3 kJ/mol, respectively. For both routes, formation of the amine product and regeneration of the catalyst is thermodynamically driven with free energies of product formation of -56.7 and -74 kJ/mol relative to **11**$_\alpha$**-CO** and **11**$_\beta$**-CO**.

From Figure 6.8, it becomes clear that, after the formation of the enamine-coordinated **8-CO** complex, the migration of hydride to C_β as a result of H migratory insertion is kinetically favored. The formation of alkylamine (**9$_\alpha$-CO**) is 22.1 kJ/mol lower in energy compared to **9$_\beta$-CO**. Since the Gibbs free energy of H_2 coordination to **9$_\alpha$-CO** is significantly higher for **9$_\beta$-CO**, the hydrogenation of enamine is more likely to may occur following the first hydride migration to C_β (yellow pathway). Comparing all four possible routes for the catalytic reduction of enamine, it is least likely to proceed via axial hydride insertion into the Rh-C bond via **11$_\alpha$-CO** intermediate due to the high activation energy of the corresponding reductive elimination transition state ($TS_{11_\alpha - COH_{ax.} \rightarrow 7-CO}$, blue pathway). For other three energy routes, first hydride insertion is the slowest elementary step with activation energies of 41.7 and 45.7 kJ/mol when the hydride migrates to C_β and C_α of the coordinated enamine, respectively. This is in agreement with the results obtained by Crozet et al. when studying the rhodium-catalyzed hydrogenation of enamine generated from styrene and piperidine [219]. However, since the insertion of the second hydride is the highest activation energy point relative to the active catalyst during hydrogenation in the free energy profiles therefore, the rate of reaction is controlled by this step. The overall activation energy for the hydrogenation of enamine following the first hydride migration to C_β relative to the active catalyst is 34.9 and 44.2 kJ/mol for the equatorial and axial hydride insertions into the Rh-alkylamine bond, respectively (see Figure 6.8, yellow and red free energy profiles) in the gas phase. When solvent effects are included, these above mentioned activation energies increase further by 14.6 and 12.2 kJ/mol ($\Delta G^{\ddagger}_{11_\beta - CO\ H_{eq.} \rightarrow 7-CO}$ = 49.6 and $\Delta G^{\ddagger}_{11_\beta - CO\ H_{ax.} \rightarrow 7-CO}$ = 61 kJ/mol) in methanol:dodecane 50:50 solution (For complete Gibbs free energy profiles in solution, see Appendix C.2). Crozet et al. [219] reported overall activation energies of 78 and 94 kJ/mol for the rhodium-catalyzed hydrogenation of enamine formed after the amination of styrene and piperidine in THF solvent. These activation energies are significantly higher than the activation energy of 18.3 kJ/mol for the hydrogenation of enamine reported by Kortuz et al. [209]

Figure 6.9 shows, the comparison of Gibbs free energy profiles of the rhodium-catalyzed hydrogenation catalyzed by the catalyst species **7** and **7-CO** in methanol: dodecane 50:50 mixture. The Gibbs free energy profiles in different solvent compositions are given in Appendix C.2. Both of these species have SX as the coordinating ligand and a free coordination site accessible for the enamine substrate (for structural details, See Figure 6.10).

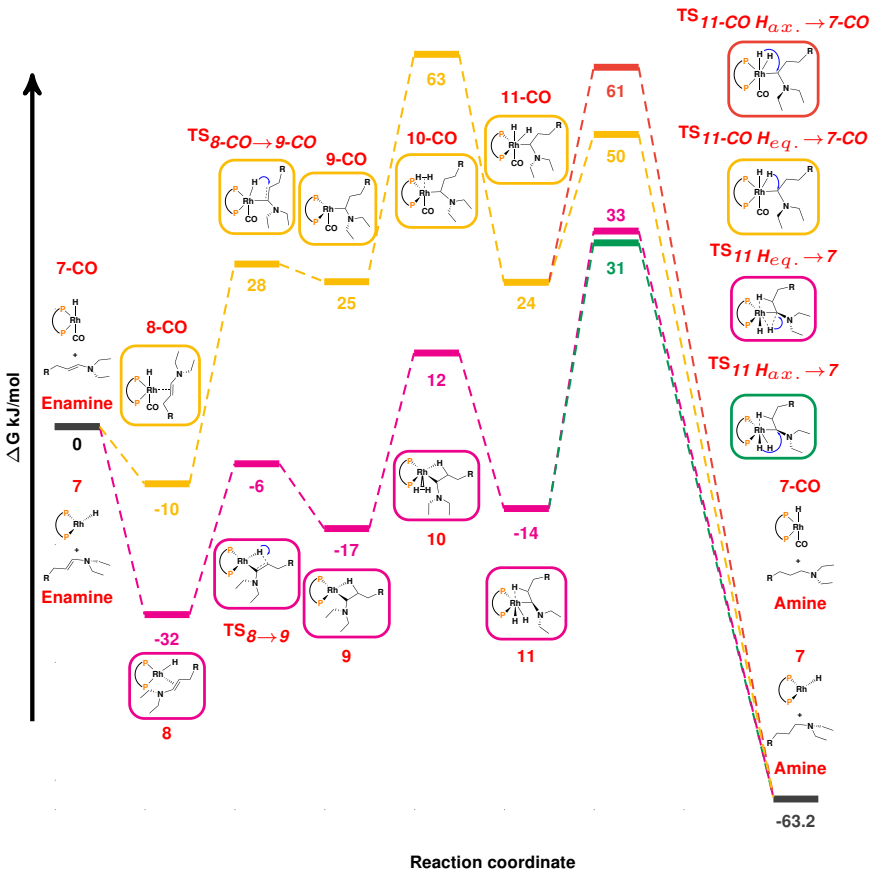

Fig. 6.9.: The effect of change in gas composition (hydrogen: (SulfoXantPhos)RhH, **7** and syngas : (SulfoXantPhos)RhH-CO, **7-CO**) on rhodium-catalyzed hydrogenation of (E)-N,N-diethylundec-1-en-1-amine (enamine) in methanol:dodecane 50:50 solution. The thermodynamic corrections were calculated at 373.15 K and 30 bar.

Upon enamine coordination to **7**, the electron density shifts from central rhodium to both phosphorus atoms. Similarly, when enamine coordinates to **7-CO**, the partial charge on rhodium reduces from -0.24 to -0.16 but the charge on phosphorous atoms remains almost constant in complex **8-CO**. However, the partial charge on the carbon atom of the carbonyl group increase from 0.47 to 0.5. Due to the presence of CO at the active catalyst, the distance between the rhodium to the center of the C=C bond of the enamine elongates by 0.15 Å when hydrogenation is performed in the presence of syngas. As a result, the Gibbs free energy of enamine coordination to complex **7-CO** is 22 kJ/mol lower than the enamine coordination to complex **7**.

For migratory hydride insertion, a rearrangement of enamine C=C double bond is necessary. At first, the double bond rotates to bring the enamine C=C double bond into the Rh-H phosphine plane, followed by the hydride insertion and finally the Rh-alkylamine complexes **9** and **9-CO** are obtained (See Figure 6.11).

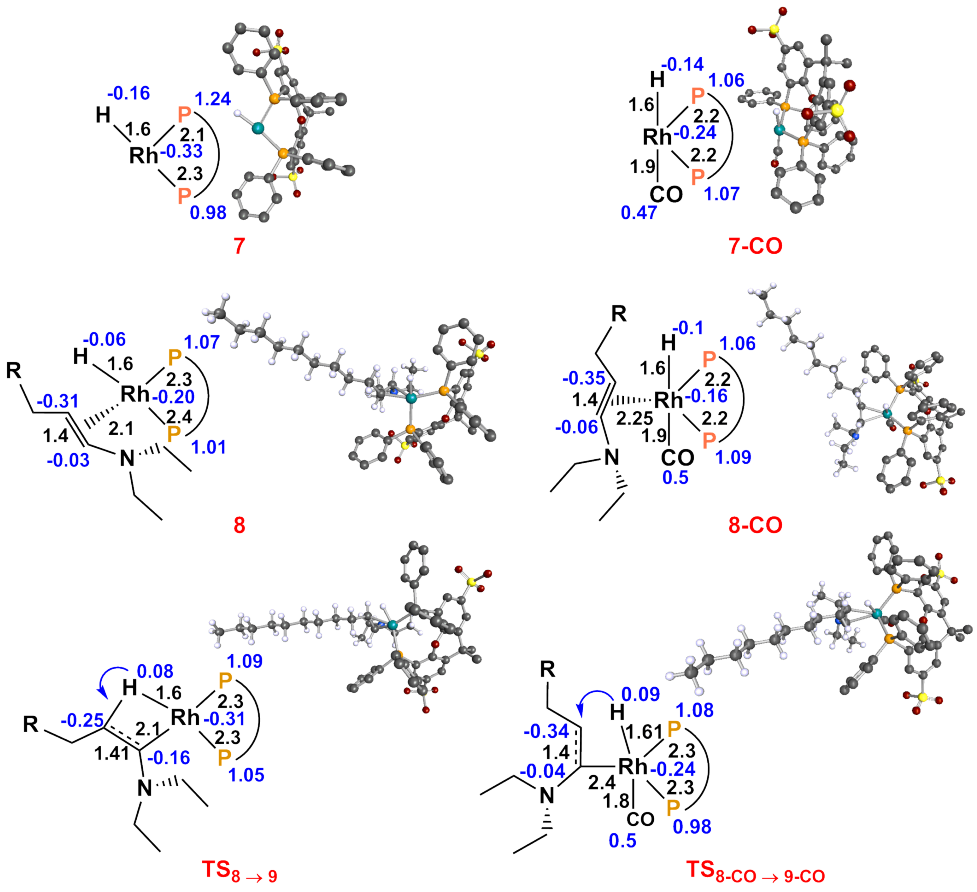

Fig. 6.10.: Structural and charge distribution details of the active catalyst for hydrogenation in the presence of pure hydrogen **7** and syngas **7-CO**, the corresponding enamine coordination complexes (**8 and 8-CO**) to the catalyst and transition state of Rh-H bond insertion into C=C double bond ($\mathbf{TS}_{7\rightarrow 8}$ and $\mathbf{TS}_{7-CO\rightarrow 8-CO}$. Hydrogen atoms from ligand are omitted for clarity. Bond distances (black) are given in Angstroms; NPA charges are given in blue.

The carbonyl group attached to central rhodium atom may hinder the C=C bond rotation. To overcome this steric hindrance during the hydride insertion into C=C double bond ($\mathbf{TS}_{7-CO\rightarrow 8-CO}$), the distance between the central rhodium and C_α further elongates by 0.15 Å. However, for ($\mathbf{TS}_{7\rightarrow 8}$), the rhodium-$C_\alpha$ distance remains unchanged. This increase of Rh-C_α bond distance results in an increase of 12 kJ/mol in the activation energy of hydride insertion ($\Delta G^{\ddagger}_{TS_{7-CO\rightarrow 8-CO}}$ = 38 kJ/mol) when hydrogenation is performed in syngas compared to the pure hydrogen ($\Delta G^{\ddagger}_{TS_{7\rightarrow 8}}$ = 26 kJ/mol) in methanol:dodecane 50:50 solution.

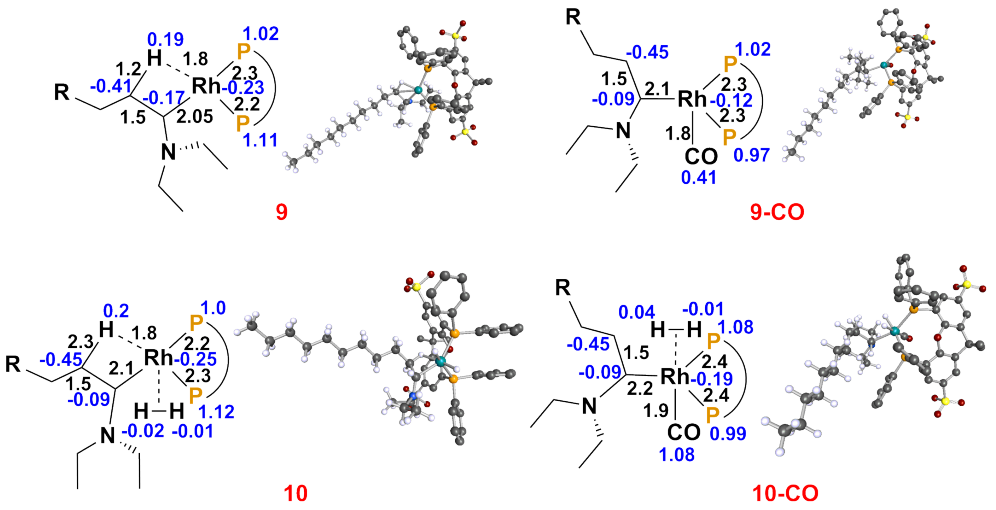

Fig. 6.11.: Structural and charge distribution details of the alkylamine formed after the hydride migration to C_β (**9** and **9-CO**) and η^2-H_2 coordination to the alkylamine complex **10** and **10-CO** in the presence of pure hydrogen and syngas. Hydrogen atoms from ligand are omitted for clarity. Bond distances (black) are given in Angstroms; NPA charges are given in blue.

The alkylamine intermediates (**9** and **9-CO**) formed after the hydride insertion lie at -17 and 25 kJ/mol with respect to initial complex **7** and **7-CO**, leading to an endergonic step with $\Delta G_{8\rightarrow 9}$ and $\Delta G_{8-CO\rightarrow 9-CO}$ of 15 and 35 kJ/mol, respectively. Complex **9** adopts an almost square planer geometry, whereas **9-CO** adopts square pyramidal structure where CO is present at the axial position. The Gibbs free energy of H_2 coordination ($\Delta G_{9-CO\ \rightarrow\ 10-CO}$) also increases by 9 kJ/mol in methanol:dodecane solution if hydrogenation is carried out in the presence of syngas rather than pure hydrogen (See Figure 6.11).

H_2 oxidative addition is almost independent of the reactant gas composition, since the Gibbs free energy associated with the formation of both **11** and **11-CO** complexes relative to intermediates **10** and **10-CO** is very small i.e. $\Delta G_{10\ \rightarrow\ 11}$ = +3 and $\Delta G_{10-CO\ \rightarrow\ 11-CO}$ = -1 kJ/mol, respectively. The activation energies for the final hydride insertion into Rh-C bond relative to complex **11-CO** in the presence of syngas leading to the final product via axial and equatorial hydride migration is 37 and 26 kJ/mol in methanol:dodecane 50:50 solution, respectively. Compared to activation energies in pure hydrogen ($\Delta G^{\ddagger}_{11\ H_{eq.}\ \rightarrow 7}$ = 47 kJ/mol and $\Delta G^{\ddagger}_{11\ H_{ax.}\ \rightarrow 7}$ = 45 kJ/mol), the activation energies for the final hydride insertion into Rh-C bond in the presence of syngas are reduced by 21 and 8 kJ/mol ($\Delta G^{\ddagger}_{11\ H_{eq.}\ \rightarrow 7}$ = 26 kJ/mol and $\Delta G^{\ddagger}_{11\ H_{ax.}\ \rightarrow 7}$ = 37 kJ/mol), when an equatorial and an axial hydride migrates to C_α, respectively (See Figure 6.9).

Several structural and electronic difference can be observed between the intermediates prior (**11** and **11-CO**) and the subsequent transition states (See Figure 6.12).

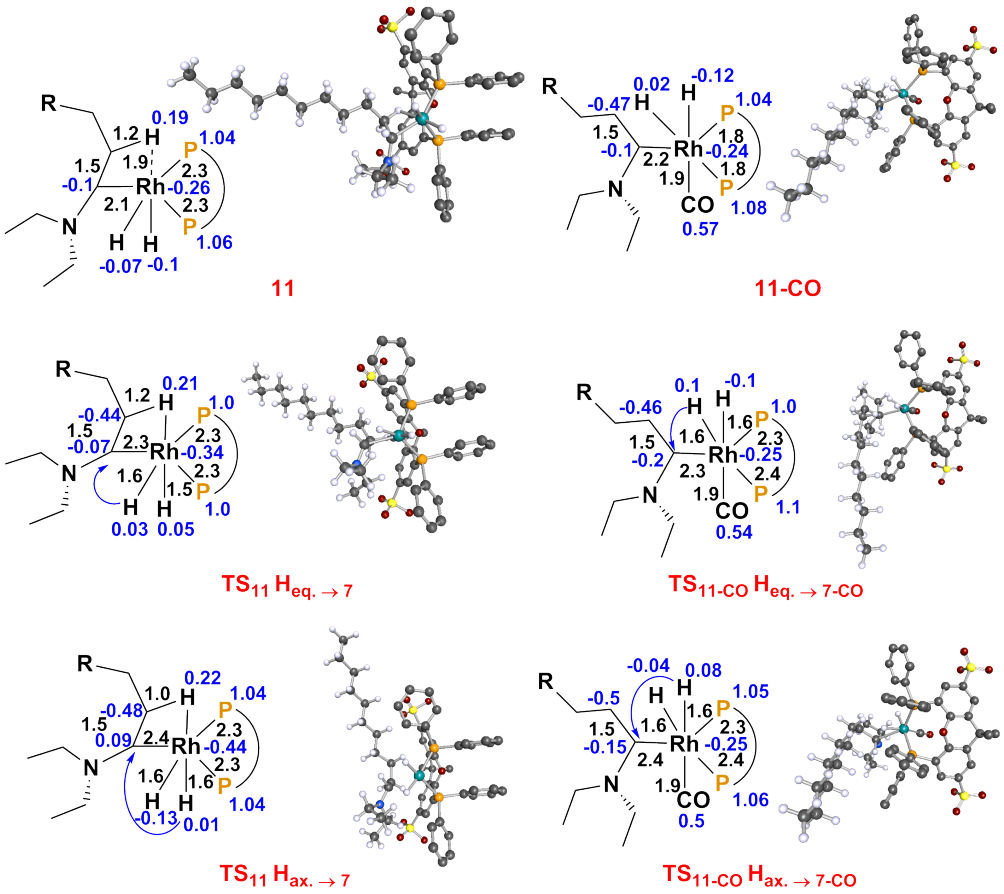

Fig. 6.12.: Structural and charge distribution details of (SX)RhHH-alkylamine **11** and (SX)RhHH-CO-alkylamine **11-CO** formed after H_2 oxidative addition and subsequent transition states for final amine product formation via equatorial and axial hydride migration to C_α in the presence of pure hydrogen and syngas. Hydrogen atoms from ligand are omitted for clarity. Bond distances (black) are given in Angstroms; NPA charges are given in blue.

In the optimized transition states for final hydride insertion in the presence of hydrogen only ($TS_{11\ H_{eq}\ \rightarrow\ 7}$ and $TS_{11\ H_{ax}\ \rightarrow\ 7}$), the Rh-$C_\alpha$ bond length increases by 0.2 Å and 0.3 Å for equatorial and axial H transfer, respectively. In addition, the electron density from the hydride and C_α shifts towards the metal center thus enhancing the charge difference between the alkylamine moiety and the attacking hydride. Similar bond elongations can also be seen for the transition states in the presence of syngas ($TS_{11-COH_{eq}\ \rightarrow\ 7-CO}$ and $TS_{11-COH_{ax}\ \rightarrow\ 7-CO}$).

In the presence of syngas, the electron density on the central rhodium in the transition states and the intermediate prior remains almost the same. However, it shifts from the inserting hydride and C_α towards the coordinated CO and results in larger charge differences between the C_α and hydride compared to the transition states when enamine reduction is performed in the presence hydrogen only and thereby, significantly reduces the activation energies for the corresponding final hydride migration (See Figure 6.9).

From Figure 6.9 it becomes apparent that hydrogenation of enamine in the presence pure hydrogenation proceeds via a low energy pathway. However, in the presence of syngas, the reaction follows a different energetic route. The presence of coordinated CO hinders the C=C bond rotation prior to the first hydride insertion thus resulting in an increase in the activation energy for the hydride migratory insertion and becomes the slowest elementary step within the hydrogenation cycle. However, the rate of hydrogenation is still controlled by final hydride migration to C_α since it is the highest energy point on the potential energy surface. The activation energy relative to the active catalyst for hydrogenation increases by over 20-30 kJ/mol if the hydrogenation of enamine take place in syngas when compared to pure hydrogen as reactant gas in methanol:dodecane solvent mixture. The activation energy for hydrogenation of enamine relative to the active catalyst (50 - 61 kJ/mol) in the presence of syngas is in agreement with the activation energy of 78 kJ/mol reported by Crozet et al. for the hydroaminomethylation of styrene and piperidine in THF solvent [219]. Similarly, Rätze et al. have also reported an activation energy of 81 kJ/mol for hydrogenation of enamine in the presence of syngas for the same catalyst system [210].

In summary, the composition of the synthesis gas has a significant effect on HAM, especially on the hydrogenation of enamine. The active catalyst species when hydrogenation of enamine is carried in the presence of pure H_2 gas differs from the active catalyst in the presence of syngas. Under the high pressure of CO, hydrogenation proceeds via a high-energy pathway in which the activation energy for the transition state and the free energy of H_2 coordination to the alkylamine species are relatively high. The (SX)RhH catalytic species drives the reaction via a low-energy pathway by reducing the overall activation energy by nearly 20-30 kJ/mol.

6.3 Conclusions for HAM in Solution

The homogeneous rhodium-catalyzed hydroaminomethylation (HAM) of 1-decene in methanol:dodecane TMS was investigated to resolve the uncertainties in the pre-existing kinetic models from Kortuz et al.[95, 101] and Rätze et al.[210] to provide more reliable initial guess for the activation energies of underlying hydroformylation (Hyfo) and reductive amination (RA) reaction steps. The effects of the catalytic ligand and the synthesis gas on the kinetics of tandem hydroaminomethylation were investigated using quantum chemical methods.

The comparison between the performance of an electron rich SX ligand and an electron-withdrawing BPP ligand showed that the choice of ligand has a significant effect on the rate of hydroformylation. In particular, the CO dissociation energy significantly increases when an electron donating SX ligand is used, so that large amounts of ligand and noble metal are required to obtain the same concentration of active catalyst in the reaction compared to the usage of an electron-withdrawing BPP ligand. In addition, the activation energy of the rate-determining step also increases, which slows down the catalytic Hyfo when BPP is exchanged with SX. The catalyst's selectivity towards the desired linear aldehydes do not depend on the electronic properties of the coordinating ligand; rather, it depends on the geometrical structure of the ligand.

Kinetic parameters strongly depend on the reaction conditions, in particular on syngas (CO/H_2) composition. The active catalyst for hydrogenation of enamine in the presence of syngas (CO/H_2) differs from that in pure hydrogen. The formation of these short-lived catalyst species cannot be observed by FTIR spectroscopy. During HAM, both hydroformylation and reductive amination are promoted by the same catalyst species. However, the initial guess in the HAM kinetic model proposed by Kortuz et al. [209] was taken from the kinetic model of reductive amination of aldehydes in pure hydrogen not in syngas. Quantum chemical calculations showed that the rhodium-catalyzed hydrogenation of enamine proceeds via different pathways when conducted using syngas or pure hydrogen. Therefore, a higher activation energy is required for the reduction using the (SX)RhH-(CO) catalyst for the hydrogenation. H_2 coordination to alkylamine **9-CO** species is an endothermic process thus, the thermodynamic equilibrium can be shifted towards the product side (**10-CO**) by ensuring excess hydrogen in the syngas mixture. However, when the (SX)RhH-CO is replaced by a (SX)RhH catalyst, the rate-limiting step for the hydrogenation changes from the initial hydride insertion into the enamine to the final hydride insertion into the Rh-alkylamine bond. The activation energy required for

hydrogenation is significantly lower when the (SX)RhH catalyst species is involved in the hydrogenation of enamine. A high content of methanol (polar solvent) in the reaction solution reduce the activation energy of the rate-limiting step of hydrogenation.

The complete reaction mechanism of HAM, is now available. Based on these results, the prediction quality of the kinetic model for HAM of 1-decene can be improved by using the activation energies calculated with quantum chemical calculations as an initial guess.

7 Conclusions

The choice of an optimal catalyst and solvent for multi-step transition metal-catalyzed reactions in solution is a complex optimization problem, often due to a lack of information on the reaction mechanism and solute-solvent interactions. Despite the significant effect of catalysts and solvents on reaction rate and selectivity, catalyst and solvent selection is generally based on empirical models or expert knowledge. Conducting screening experiments with various catalyst and solvent candidates is both costly and time-consuming. To reduce the experimental costs associated with investigating the effects of catalyst and solvent in multi-step metal-catalyzed reactions, quantum chemical modelling is a valuable tool.

In this study, the mechanisms and solvent effects of three complex, multi-step, transition metal-catalyzed reactions of renewable oleo-chemicals were investigated. These reactions include hydroformylation of 1-decene, reductive amination of 1-undecanal, and hydroaminomethylation of 1-decene. The kinetic information obtained from the mechanistic studies was then used for two purposes to support process development and optimization. Firstly, it assisted in computer-aided solvent selection. Second, it contributed to the development of kinetic models by providing estimated values for the activation energies of rate-limiting steps. This significantly reduced the experimental efforts required for solvent selection and development of the kinetic models.

An ideal catalyst must have high activity, selectivity, and stability. A mechanistic analysis of the hydroformylation of 1-decene derived from palm oil using the (BiPhePhos)RhH-CO catalyst in a dimethylformamide (DMF):decane solvent blend indicated that the insertion of hydride into the olefin is the decisive step for both the rate and selectivity. After addressing potential side reactions, including double bond isomerization and olefin hydrogenation, the BPP-based catalyst demonstrated remarkable selectivity ($S_{linear:branched}$ = 98:2) towards the desired linear aldehydes. Given the hazardous nature of DMF utilized in the hydroformylation experiment, an environmentally-friendly solvent alternative is necessary. The polarity of the solvent slightly impacts the hydroformylation rate, with polar solvents being more advantageous than non-polar ones. The catalyst's (BiPhePhos)RhH-(CO) solubility is significantly influenced by the solvent's nature. Eco-friendly solvents like methanol

or water can replace the toxic DMF when using a water-soluble SulfoXantPhos ligand instead of BiPhePhos, without compromising the catalytic selectivity. The study found that substrate impurities, specifically peroxide impurities generated by substrate exposure to air, affect catalyst stability. In the presence of these impurities, the catalyst may partially oxidize, leading to the formation of single-arm complexes. The reaction results in a reduction in catalytic selectivity, which can be partially restored by adding additional ligand to the reaction mixture. Alternatively, if the ligand undergoes complete oxidation, Rh-carbonyl clusters may form, causing the total loss of catalytic activity.

To minimize the time and costs associated with experimental solvent screening, a multi-step solvent selection workflow was developed and applied to the reductive amination of 1-undecanal from fennel oil and diethylamine (DEA) to rapidly and reliably predict promising solvents for achieving high reaction rates. The rate-determining step for reductive amination using hydrogen as the reducing agent is the insertion of hydride into the Rh-alkylamine bond. A number of solvent candidates were tested using an implicit solvent model to investigate the effect of solvent on the reaction rate. Consequently, the number of solvent candidates was significantly reduced. Afterward, the solvent candidates with similar dielectric constant (solvent polarity) were further investigated based on their explicit catalyst-solvent and substrate-solvent interactions to investigate the possibility of catalyst inhibition. The study of catalyst-solvent interactions showed that an optimal solvent for rhodium-catalyzed reductive amination must not compete with the reaction substrates (enamine and H_2), thus maximizing the concentration of active catalyst in solution. Additionally, investigation of the ability of a solvent to form hydrogen bonds (proticity) with the substrate using the cluster/continuum solvent model showed that a hydrogen bond donating solvent acts as a catalyst during amination. These solvents serve as proton transfer agents during amination and reduce the activation energies of the transition states for nucelophilic addition and condensation. Batch experiments have confirmed these findings for specific solvents. Thus, this computer-assisted workflow allows for effective solvent pre-selection for a specific reaction that should be further investigated.

As kinetic models are unique to each catalyst system, a change in the molecular structure of a catalyst will alter the activation energy of the rate-determining step. In the hydroaminomethylation (HAM) of 1-decene, quantum chemical calculations showed that the change of the coordination ligand has a significant effect on the reaction rate. The active catalyst concentration in the catalytic mixture decreases significantly when the electron-withdrawing bipohosphite ligand BiPhePhos (BPP) is replaced by the electron-donating water-soluble SulfoXantPhos (SX) during HAM.

In addition, the activation energy for hydroformylation increases upon replacing the electron-withdrawing BPP with the electron-donating SX ligand, thereby decreasing the reaction rate. The selectivity of the catalyst remains unaffected by the electronic properties of the coordinating ligand, but its geometry can have a significant effect. In addition, a change in the reaction conditions for example, changing pure hydrogen to synthesis gas (CO/H_2) changes the reaction pathway for the reduction of enamine, thereby changing the activation energies of the transition states.

In conclusion, mechanism resolution using quantum chemical modeling allows reliable estimations of solvent and catalyst effects on the kinetics of complex multi-step chemical reactions. It provides the activation energies of all transition states formed during a multi-step reaction and assist in the generation of kinetic models and thereby reduce the experimental costs associated with catalyst and solvent selection.

7.1 Outlook

Catalyst and solvent selection for complex multi-step reactions in industry benefits from further research in the following directions: development of automated computer-aided catalyst screening and inclusion of the impacts on health, safety and environment factors in the catalyst and solvent selection.

Using quantum chemical tools, a large number of potential catalyst candidates can be screened using cheap semi-empirical methods such as GFN-xTB and promising candidates can be identified for further investigation using expensive methods such as DFT and DLPNO-CCSD(T). Several catalyst/ligand datasets such as Kraken [220] and OSCAR [221] for transition metal catalyzed reactions have recently been published that can be used not only for catalyst screening but also for the development of machine learning models for catalyst design.

For a transition metal-catalyzed multi-step reaction with a known mechanism, the first step towards an efficient catalyst selection/screening is the investigation of steric and electronic effects using a virtual or fixed ligand with different central transition metal atoms. Using a virtual ligand instead of bulky and structurally diverse ligands facilitates the assessment of the effect of the ligand coordination space around the transition metal, such as the bite angle (for bidendate ligands) and electronic properties on the transition states at reduced computational cost. Following identification of the steric and electronic properties of a possible catalyst candidate, a number of potential ligand candidates are retrieved from a database.

The ligand's effect on the activation energies of the rate and selectivity determining transition states is first estimated using a robust semi-empirical method, and then the activation energies are refined using either DFT or DLPNO-CCSD(T). Eventually, the most promising catalysts are further investigated in experiments. The same workflow can also be used for the reaction with unknown reaction mechanisms where at first the possible reaction mechanism should be estimated.

After the initial demonstration of applicability, the three-step solvent selection workflow presented offers further potential for optimizing the yield of the reactions studied in this work. The computer-aided solvent screening should be extended to solvent mixtures, since the activation energy barriers of the rate-determining transition states in the mixture may differ significantly from those in the pure solvents. Additional solvent selection criteria such as environmental safety must also be added to meet the guidelines of sustainable green chemistry.

Bibliography

[1] From energy to chemicals, IEA, Paris, **2018**, https://www.iea.org/commentaries/from-energy-to-chemicals (visited on Jan. 16, 2023).

[2] U. Nations, Transforming our world: The 2030 agenda for sustainable development, *New York: United Nations Department of Economic and Social Affairs* **2015**.

[3] Umweltbundesamt, Treibhausgas-Emissionen. Emissionsquellen, **2021**, https://www.umweltbundesamt.de/themen/klima-energie/treibhausgas-emissionen/emissionsquellen#energie-stationar (visited on Nov. 1, 2022).

[4] P. Anastas, J. Warner, *Green Chemistry: Theory and Practice*, Oxford University Press, Oxford, England, **1998**.

[5] U. Biermann, U. T. Bornscheuer, I. Feussner, M. A. R. Meier, J. O. Metzger, Fatty Acids and their Derivatives as Renewable Platform Molecules for the Chemical Industry, *Angew. Chem. Int. Ed.* **2021**, *60*, 20144–20165.

[6] G. T. Whiteker, C. J. Cobley, "Applications of Rhodium-Catalyzed Hydroformylation in the Pharmaceutical, Agrochemical, and Fragrance Industries" in *Organometallics as Catalysts in the Fine Chemical Industry*, (Eds.: M. Beller, H.-U. Blaser), Springer Berlin Heidelberg, **2012**, 35–46.

[7] A. Behr, *Angewandte homogene Katalyse*, *Vol. 342*, Wiley-VCH Weinheim, Germany, **2008**.

[8] W. Koch, M. C. Holthausen, *A chemist's guide to density functional theory*, Wiley-VCH, Weinheim, Germany, **2015**.

[9] J. A. Christiansen, The Elucidation of Reaction Mechanisms by the Method of Intermediates in Quasi-Stationary Concentrations, *Advances in Catalysis* **1953**, *5*, 311–353.

[10] G. Kiedorf, PhD thesis, Shaker Verlag Aachen, Germany, **2017**.

[11] A. Jörke, PhD thesis, Shaker Verlag Aachen, Germany, **2018**.

[12] F. Jameel, E. Kohls, M. Stein, Mechanism and control of the palladium-catalyzed alkoxycarbonylation of oleochemicals from sustainable sources, *ChemCatChem* **2019**, *11*, 4894–4906.

[13] S. Kirschtowski, F. Jameel, M. Stein, A. Seidel-Morgenstern, C. Hamel, Kinetics of the reductive amination of 1-undecanal in thermomorphic multicomponent system, *Chem. Eng. Sci.* **2021**, *230*, 116187.

[14] B. Cornils, W. A. Herrmann, Concepts in homogeneous catalysis: the industrial view, *J. Catal.* **2003**, *216*, 23–31.

[15] J. Chipperfield, *Non-aqueous Solvents*, Oxford University Press, Oxford, **1999**.

[16] A. Soyemi, T. Szilvási, Trends in computational molecular catalyst design, *Dalton Trans.* **2021**, *50*, 10325–10339.

[17] C. Poree, F. Schoenebeck, A Holy Grail in Chemistry: Computational Catalyst Design: Feasible or Fiction?, *Acc. Chem. Res.* **2017**, *50*, 605–608.

[18] W. Thiel, Computational Catalysis—Past, Present, and Future, *Angew. Chem. Int. Ed.* **2014**, *53*, 8605–8613.

[19] M. G. Quesne, F. Silveri, N. H. de Leeuw, C. R. A. Catlow, Advances in Sustainable Catalysis: A Computational Perspective, *Front. Chem.* **2019**, *7*, 182.

[20] J. A. Gillespie, E. Zuidema, P. W. N. M. van Leeuwen, P. C. J. Kamer, Phosphorus Ligand Effects in Homogeneous Catalysis and Rational Catalyst Design, *ChemInform.* **2012**, *44*.

[21] F. Studt, Grand Challenges in Computational Catalysis, *Front. Catal.* **2021**, *1*, 658965.

[22] J. K. Nørskov, J. Rossmeisl, A. Logadottir, L. Lindqvist, J. R. Kitchin, T. Bligaard, H. Jónsson, Origin of the Overpotential for Oxygen Reduction at a Fuel-Cell Cathode, *J. Phys. Chem. B* **2004**, *108*, 17886–17892.

[23] A. J. Medford, A. Vojvodic, J. S. Hummelshøj, J. Voss, F. Abild-Pedersen, F. Studt, T. Bligaard, A. Nilsson, J. K. Nørskov, From the Sabatier principle to a predictive theory of transition-metal heterogeneous catalysis, *J. Catal.* **2015**, *328*, 36–42.

[24] Z.-J. Zhao, S. Liu, S. Zha, D. Cheng, F. Studt, G. Henkelman, J. Gong, Theory-guided design of catalytic materials using scaling relationships and reactivity descriptors, *Nat. Rev. Mater.* **2019**, *4*, 792–804.

[25] J. N. Harvey, F. Himo, F. Maseras, L. Perrin, Scope and Challenge of Computational Methods for Studying Mechanism and Reactivity in Homogeneous Catalysis, *ACS Catal.* **2019**, *9*, 6803–6813.

[26] S. Schmidt, G. Abkai, T. Rosendahl, F. Rominger, P. Hofmann, Inter- and Intramolecular Interactions in Triptycene-Derived Bisphosphite Hydroformylation Catalysts: Structures, Energies, and Caveats for DFT-Assisted Ligand Design, *Organometallics* **2013**, *32*, 1044–1052.

[27] M. B. Hursthouse, D. S. Hughes, T. Gelbrich, T. L. Threlfall, Describing hydrogen-bonded structures; topology graphs, nodal symbols and connectivity tables, exemplified by five polymorphs of each of sulfathiazole and sulfapyridine, *Chem. Cent. J.* **2015**, *9*, 1.

[28] E. N. Bess, D. M. Guptill, H. M. L. Davies, M. S. Sigman, Using IR vibrations to quantitatively describe and predict site-selectivity in multivariate Rh-catalyzed C-H functionalization, *Chem. Sci.* **2015**, *6*, 3057–3062.

[29] M. Gerlach, F. Jameel, A. Seidel-Morgenstern, M. Stein, C. Hamel, Operando characterization of rhodium catalyst degradation in hydroformylation, *Catal. Sci. Technol.* **2023**, *13*, 1788–1801.

[30] G. G. Gerosa, M. O. Marcarino, R. A. Spanevello, A. G. Suárez, A. M. Sarotti, Re-Engineering Organocatalysts for Asymmetric Friedel-Crafts Alkylation of Indoles through Computational Studies, *J. Org. Chem.* **2020**, *85*, 9969–9978.

[31] M. Foscato, V. R. Jensen, Automated in Silico Design of Homogeneous Catalysts, *ACS Catal.* **2020**, *10*, 2354–2377.

[32] A. M. Krieger, P. Kuliaev, F. Q. Armstrong Hall, D. Sun, E. A. Pidko, Composition- and Condition-Dependent Kinetics of Homogeneous Ester Hydrogenation by a Mn-Based Catalyst, *J. Phys. Chem. C* **2020**, *124*, 26990–26998.

[33] Z. Sun, Q. Wang, Y. Xu, Z. Wang, A computationally designed titanium-mediated amination of allylic alcohols for the synthesis of secondary allylamines, *RSC Adv.* **2015**, *5*, 84284–84289.

[34] L. C. Burrows, L. T. Jesikiewicz, P. Liu, K. M. Brummond, Mechanism and Origins of Enantioselectivity in the Rh(I)-Catalyzed Pauson-Khand Reaction: Comparison of Bidentate and Monodentate Chiral Ligands, *ACS Catal.* **2021**, *11*, 323–336.

[35] T. Welton, C. Reichardt, *Solvents and solvent effects in organic chemistry*, Wiley-VCH, Weinheim, Germany, **2011**.

[36] O. Riechert, M. Husham, G. Sadowski, T. Zeiner, Solvent effects on esterification equilibria, *AIChE J.* **2015**, *61*, 3000–3011.

[37] G. Norjmaa, G. Ujaque, A. Lledós, Beyond Continuum Solvent Models in Computational Homogeneous Catalysis, *Top. Catal.* **2022**, *65*, 118–140.

[38] E. Siougkrou, A. Galindo, C. S. Adjiman, "Recent Advances in the Molecular Engineering of Solvents for Reactions" in *Handbook of Green Chemistry*, Wiley-VCH, Weinheim, Germany, **2019**, Chapter 2, 17–46.

[39] J. J. Varghese, S. H. Mushrif, Origins of complex solvent effects on chemical reactivity and computational tools to investigate them: a review, *React. Chem. Eng.* **2019**, *4*, 165–206.

[40] P. Deglmann, A. Schäfer, C. Lennartz, Application of quantum calculations in the chemical industry—An overview, *Int. J. Quantum Chem.* **2015**, *115*, 107–136.

[41] W. Clegg, G. R. Eastham, M. R. Elsegood, B. T. Heaton, J. A. Iggo, R. P. Tooze, R. Whyman, S. Zacchini, Synthesis and reactivity of palladium hydrido-solvento complexes, including a key intermediate in the catalytic methoxycarbonylation of ethene to methyl propanoate, *Journal of the Chemical Society Dalton Transactions* **2002**, 3300–3308.

[42] M. Gerlach, S. Kirschtowski, A. Seidel-Morgenstern, C. Hamel, Kinetic modeling of the palladium-catalyzed isomerizing methoxycarbonylation of 1-decene, *Chem. Ing. Tech.* **2018**, *90*, 673–678.

[43] D. Prat, J. Hayler, A. Wells, A survey of solvent selection guides, *Green Chem.* **2014**, *16*, 4546–4551.

[44] D. Prat, A. Wells, J. Hayler, H. Sneddon, C. R. McElroy, S. Abou-Shehada, P. J. Dunn, CHEM21 selection guide of classical- and less classical-solvents, *Green Chem.* **2016**, *18*, 288–296.

[45] M. P. Wilson, M. R. Schwarzman, Toward a New U.S. Chemicals Policy: Rebuilding the Foundation to Advance New Science, Green Chemistry, and Environmental Health, *Environ. Health Perspect.* **2009**, *117*, 1202–1209.

[46] V. H. Edwards, M. A. Ray, A. English, R. Ellis, J. Chosnek, E. Geaslin, S. L. Jones, Integrate health, safety, and environment into engineering projects, *Chem. Eng. Prog.* **2013**, *109*, 50–55.

[47] P. van Leeuwen, *Homogeneous Catalysis: Understanding the Art*, Springer Netherlands, **2006**.

[48] O Roelen, German patent DE 849,548, 1938/1952, **1943**, *2*, 66.

[49] A. Börner, R. Franke, *Hydroformylation*, Wiley-VCH, Weinheim, Germany, **2016**, 1–4.

[50] W. Thiel, Applied Homogeneous Catalysis. Von A. Behr, P. Neubert. *Chem. Ing. Tech.* **2012**, *84*, 275.

[51] R. Franke, D. Selent, A. Börner, Applied Hydroformylation, *Chem. Rev.* **2012**, *112*, 5675–5732.

[52] I. Wender, H. Sternberg, M Orchin, Evidence for cobalt hydrocarbonyl as the hydroformylation catalyst, *J. Am. Chem. Soc.* **1953**, *75*, 3041–3042.

[53] R. van Duren, J. I. van der Vlugt, H. Kooijman, A. L. Spek, D. Vogt, Platinum-catalyzed hydroformylation of terminal and internal octenes, *Dalton Trans.* **2007**, 1053–1059.

[54] L. Wu, I. Fleischer, R. Jackstell, I. Profir, R. Franke, M. Beller, Ruthenium-Catalyzed Hydroformylation/Reduction of Olefins to Alcohols: Extending the Scope to Internal Alkenes, *J. Am. Chem. Soc.* **2013**, *135*, 14306–14312.

[55] K. ichi Tominaga, Y. Sasaki, Ruthenium-catalyzed one-pot hydroformylation of alkenes using carbon dioxide as a reactant, *J. Mol. Catal. A: Chem.* **2004**, *220*, 159–165.

[56] I. Piras, R. Jennerjahn, R. Jackstell, A. Spannenberg, R. Franke, M. Beller, A General and Efficient Iridium-Catalyzed Hydroformylation of Olefins, *Angew. Chem. Int. Ed.* **2011**, *50*, 280–284.

[57] K.-D. Wiese, D. Obst, "Hydroformylation" in *Catalytic Carbonylation Reactions*, (Ed.: M. Beller), Springer, Berlin, Heidelberg, **2006**, 1–33.

[58] D. Evans, J. A. Osborn, G. Wilkinson, Hydroformylation of alkenes by use of rhodium complex catalysts, *J. Chem. Soc. A* **1968**, 3133–3142.

[59] M. Kranenburg, Y. E. M. van der Burgt, P. C. J. Kamer, P. W. N. M. van Leeuwen, K. Goubitz, J. Fraanje, New Diphosphine Ligands Based on Heterocyclic Aromatics Inducing Very High Regioselectivity in Rhodium-Catalyzed Hydroformylation: Effect of the Bite Angle, *Organometallics* **1995**, *14*, 3081–3089.

[60] P. C. J. Kamer, P. W. N. M. van Leeuwen, J. N. H. Reek, Wide Bite Angle Diphosphines:Xantphos Ligands in Transition Metal Complexes and Catalysis, *Acc. Chem. Res.* **2001**, *34*, 895–904.

[61] C. Kunze, D. Selent, I. Neda, M. Freytag, P. G. Jones, R. Schmutzler, W. Baumann, A. Börner, Calix[4]arene-based Bis-phosphonites, Bis-phosphites, and Bis-O-acyl-phosphites as Ligands in the Rhodium(I)-catalyzed Hydroformylation of 1-Octene, *Z. Anorg. Allg. Chem.* **2002**, *628*, 779–787.

[62] D. Selent, W. Baumann, R. Kempe, A. Spannenberg, D. Röttger, K.-D. Wiese, A. Börner, Reactions of a Hydroxy Phosphonite Ligand in the Coordination Sphere of Rhodium(I), *Organometallics* **2003**, *22*, 4265–4271.

[63] A. G. Abatjoglou, E. Billig, D. R. Bryant, Mechanism of rhodium-promoted triphenylphosphine reactions in hydroformylation processes, *Organometallics* **1984**, *3*, 923–926.

[64] B. Moasser, W. L. Gladfelter, D. C. Roe, Mechanistic Aspects of a Highly Regioselective Catalytic Alkene Hydroformylation using a Rhodium Chelating Bis(phosphite) Complex, *Organometallics* **1995**, *14*, 3832–3838.

[65] A. van Rooy, E. N. Orij, P. C. J. Kamer, P. W. N. M. van Leeuwen, Hydroformylation with a Rhodium/Bulky Phosphite Modified Catalyst. A Comparison of the Catalyst Behavior for Oct-1-ene, Cyclohexene, and Styrene, *Organometallics* **1995**, *14*, 34–43.

[66] P. W. N. M. van Leeuwen, P. C. J. Kamer, J. N. H. Reek, P. Dierkes, Ligand Bite Angle Effects in Metal-catalyzed C-C Bond Formation, *Chem. Rev.* **2000**, *100*, 2741–2770.

[67] P. W. N. M. Leeuwen, C. Claver, *Rhodium Catalyzed Hydroformylation*, Springer Dordrecht, Netherlands, **2002**.

[68] P. van Leeuwen, C. Roobeek, Hydroformylation of less reactive olefins with modified rhodium catalysts, *J. Organomet. Chem.* **1983**, *258*, 343–350.

[69] C. P. Casey, G. T. Whiteker, The Natural Bite Angle of Chelating Diphosphines, *Isr. J. Chem.* **1990**, *30*, 299–304.

[70] M. Ahmed, R. P. J. Bronger, R. Jackstell, P. C. J. Kamer, P. W. N. M. van Leeuwen, M. Beller, Highly Selective Hydroaminomethylation of Internal Alkenes To Give Linear Amines, *Chem. Eur. J.* **2006**, *12*, 8979–8988.

[71] Y. Jiao, M. S. Torne, J. Gracia, J. W. H. Niemantsverdriet, P. W. N. M. van Leeuwen, Ligand effects in rhodium-catalyzed hydroformylation with bisphosphines: steric or electronic?, *Catal. Sci. Technol.* **2017**, *7*, 1404–1414.

[72] C. A. Tolman, Electron donor-acceptor properties of phosphorus ligands. Substituent additivity, *J. Am. Chem. Soc.* **1970**, *92*, 2953–2956.

[73] "Introduction" in *Homogeneous Catalysis: Understanding the Art*, Springer Netherlands, Dordrecht, **2004**, 1–28.

[74] E. Billig, A. G. Abatjoglou, D. R. Bryant, Transition metal complex catalyzed processes, US patent: US4769498A, **1987**.

[75] T. Kégl, Computational aspects of hydroformylation, *RSC Adv.* **2015**, *5*, 4304–4327.

[76] J. J. Carbó, F. Maseras, C. Bo, P. W. N. M. van Leeuwen, Unraveling the Origin of Regioselectivity in Rhodium Diphosphine Catalyzed Hydroformylation. A DFT QM/MM Study, *J. Am. Chem. Soc.* **2001**, *123*, 7630–7637.

[77] X. Luo, D. Tang, M. Li, Revealing the mechanism of Rh(I)-catalyzed hydroformylation of 4-pyridylethene derivatives: DFT study, *Int. J. Quantum Chem.* **2006**, *106*, 1844–1852.

[78] T. Matsubara, N. Koga, Y. Ding, D. G. Musaev, K. Morokuma, Ab Initio MO Study of the Full Cycle of Olefin Hydroformylation Catalyzed by a Rhodium Complex, RhH(CO)2(PH3)2, *Organometallics* **1997**, *16*, 1065–1078.

[79] A. van Rooy, P. C. J. Kamer, P. W. N. M. van Leeuwen, K. Goubitz, J. Fraanje, N. Veldman, A. L. Spek, Bulky Diphosphite-Modified Rhodium Catalysts: Hydroformylation and Characterization, *Organometallics* **1996**, *15*, 835–847.

[80] A. Jörke, A. Seidel-Morgenstern, C. Hamel, Rhodium-BiPhePhos catalyzed hydroformylation studied by operando FTIR spectroscopy: Catalyst activation and rate determining step, *J. Mol. Catal. A: Chem.* **2017**, *426*, 10–14.

[81] U. Gellrich, W. Seiche, M. Keller, B. Breit, Mechanistic Insights into a Supramolecular Self-Assembling Catalyst System: Evidence for Hydrogen Bonding during Rhodium-Catalyzed Hydroformylation, *Angew. Chem. Int. Ed.* **2012**, *51*, 11033–11038.

[82] U. Gellrich, D. Himmel, M. Meuwly, B. Breit, Realistic Energy Surfaces for Real-World Systems: An IMOMO CCSD(T):DFT Scheme for Rhodium-Catalyzed Hydroformylation with the 6-DPPon Ligand, *Chem. Eur. J.* **2013**, *19*, 16272–16281.

[83] D. Gleich, J. Hutter, Computational Approaches to Activity in Rhodium-Catalysed Hydroformylation, *Chem. Eur. J.* **2004**, *10*, 2435–2444.

[84] C. R. Landis, J. Uddin, Quantum mechanical modelling of alkene hydroformylation as catalyzed by xantphos-Rh complexes, *J. Chem. Soc., Dalton Trans.* **2002**, 729–742.

[85] S. A. Lawrence, *Amines: synthesis, properties and applications*, Cambridge University Press, Cambridge, UK, **2004**.

[86] K. Eller, E. Henkes, R. Rossbacher, H. Höke, Amines, aliphatic, *Ullmann's Encyclopedia of Industrial Chemistry* **2000**.

[87] M. Ahmed, A. M. Seayad, R. Jackstell, M. Beller, Amines Made Easily: A Highly Selective Hydroaminomethylation of Olefins, *J. Am. Chem. Soc.* **2003**, *125*, 10311–10318.

[88] A. F. Abdel-Magid, K. G. Carson, B. D. Harris, C. A. Maryanoff, R. D. Shah, Reductive Amination of Aldehydes and Ketones with Sodium Triacetoxyborohydride. Studies on Direct and Indirect Reductive Amination Procedures1, *J. Org. Chem.* **1996**, *61*, 3849–3862.

[89] T. Irrgang, R. Kempe, Transition-Metal-Catalyzed Reductive Amination Employing Hydrogen, *Chem. Rev.* **2020**, *120*, 9583–9674.

[90] L. Markó, J. Bakos, Homogeneous reductive amination with cobalt and rhodium carbonyls as catalysts, *J. Organomet. Chem.* **1974**, *81*, 411–414.

[91] H.-U. Blaser, H.-P. Buser, H.-P. Jalett, B. Pugin, F. Spindler, Iridium Ferrocenyl Diphosphine Catalyzed Enantioselective Reductive Alkylation of a Hindered Aniline, *Syn. lett.* **1999**, 867–868.

[92] T. Gross, A. M. Seayad, M. Ahmad, M. Beller, Synthesis of Primary Amines: First Homogeneously Catalyzed Reductive Amination with Ammonia, *Org. Lett.* **2002**, *4*, 2055–2058.

[93] W. Reppe, H. Vetter, Carbonylierung VI. Synthesen mit Metallcarbonylwasserstoffen, *Justus Liebigs Ann. Chem.* **1953**, *582*, 133–161.

[94] T. A. Larson, Synthesis of amines, *US Patent 2497310* **1950**, *44*, 4489.

[95] W. Kortuz, S. Kirschtowski, A. Seidel-Morgenstern, C. Hamel, Kinetics of the Rhodium-Catalyzed Hydroaminomethylation of 1-Decene in a Thermomorphic Solvent System, *Chem. Ing. Tech.* **2022**, *94*, 760–765.

[96] C. Chen, X.-Q. Dong, X. Zhang, Recent progress in rhodium-catalyzed hydroaminomethylation, *Org. Chem. Front.* **2016**, *3*, 1359–1370.

[97] S. Gülak, L. Wu, Q. Liu, R. Franke, R. Jackstell, M. Beller, Phosphine- and Hydrogen-Free: Highly Regioselective Ruthenium-Catalyzed Hydroaminomethylation of Olefins, *Angew. Chem. Int. Ed.* **2014**, *53*, 7320–7323.

[98] J. Yang, F. G. Delolo, A. Spannenberg, R. Jackstell, M. Beller, A Selective and General Cobalt-Catalyzed Hydroaminomethylation of Olefins to Amines, *Angew. Chem. Int. Ed.* **2022**, *61*, e202112597.

[99] S. Hanna, J. C. Holder, J. F. Hartwig, A Multicatalytic Approach to the Hydroaminomethylation of α-Olefins, *Angew. Chem.* **2019**, *131*, 3406–3410.

[100] D. Crozet, M. Urrutigoïty, P. Kalck, Recent Advances in Amine Synthesis by Catalytic Hydroaminomethylation of Alkenes, *ChemCatChem* **2011**, *3*, 1102–1118.

[101] W. Kortuz, S. Kirschtowski, A. Seidel-Morgenstern, C. Hamel, Kinetics of the Rhodium-Catalyzed Hydroaminomethylation of 1-Decene in a Thermomorphic Solvent System, *Chem. Ing. Tech.* **2022**, *94*, 760–765.

[102] A. F. M. Iqbal, Catalytic Aminomethylation of Alkenoic Compounds: I. Reaction of monoolefins with secondary amines, carbon monoxide, and water in the presence of rhodium and iron catalysts, *Helv. Chim. Acta* **1971**, *54*, 1440–1445.

[103] H. M. de Bruijn, C. Fonseca Guerra, E. Bouwman, F. M. Bickelhaupt, The Hydrogenation Problem in Cobalt-based Catalytic Hydroaminomethylation, *ChemistrySelect* **2020**, *5*, 13981–13994.

[104] P. Kalck, M. Urrutigoïty, Tandem Hydroaminomethylation Reaction to Synthesize Amines from Alkenes, *Chem. Rev.* **2018**, *118*, 3833–3861.

[105] W. Thiel, Applied Homogeneous Catalysis. Von A. Behr, P. Neubert. *Chem. Ing. Tech.* **2012**, *84*, 80–90.

[106] B. Zimmermann, J. Herwig, M. Beller, The First Efficient Hydroaminomethylation with Ammonia: With Dual Metal Catalysts and Two-Phase Catalysis to Primary Amines, *Angew. Chem. Int. Ed.* **1999**, *38*, 2372–2375.

[107] J. R. Briggs, J. Klosin, G. T. Whiteker, Synthesis of Biologically Active Amines via Rhodium-Bisphosphite-Catalyzed Hydroaminomethylation, *Org. Lett.* **2005**, *7*, 4795–4798.

[108] K. C. Oliveira, S. N. Carvalho, M. F. Duarte, E. V. Gusevskaya, E. N. dos Santos, J. E. Karroumi, M. Gouygou, M. Urrutigoïty, Phospholes as efficient ancillaries for the rhodium-catalyzed hydroformylation and hydroaminomethylation of estragole, *Appl. Catal. A* **2015**, *497*, 10–16.

[109] J. A. Fuentes, P. Wawrzyniak, G. J. Roff, M. Bühl, M. L. Clarke, On the rate-determining step and the ligand electronic effects in rhodium catalysed hydrogenation of enamines and the hydroaminomethylation of alkenes, *Catal. Sci. Technol.* **2011**, *1*, 431–436.

[110] A. Seayad, M. Ahmed, H. Klein, R. Jackstell, T. Gross, M. Beller, Internal Olefins to Linear Amines, *Science* **2002**, *297*, 1676–1678.

[111] M. Ahmed, A. M. Seayad, R. Jackstell, M. Beller, Amines Made Easily: A Highly Selective Hydroaminomethylation of Olefins, *J. Am. Chem. Soc.* **2003**, *125*, 10311–10318.

[112] B. Hamers, P. S. Bäuerlein, C. Müller, D. Vogt, Hydroaminomethylation of n-Alkenes in a Biphasic Ionic Liquid System, *Adv. Synth. Catal.* **2008**, *350*, 332–342.

[113] T. Vanbésien, J. Le Nôtre, E. Monflier, F. Hapiot, Hydroaminomethylation of oleochemicals: A comprehensive overview, *Eur. J. Lipid Sci. Technol* **2018**, *120*, 1700190.

[114] G. C. Arena, Amines via Hydroaminomethylation: An Updated Overview, *Curr. Org. Chem.* **2021**, *25*, 1831–1852.

[115] T. Seidensticker, J. M. Vosberg, K. A. Ostrowski, A. J. Vorholt, Rhodium-Catalyzed Bis-Hydroaminomethylation of Linear Aliphatic Alkenes with Piperazine, *Adv. Synth. Catal.* **2016**, *358*, 610–621.

[116] A. J. Vorholt, S. Immohr, K. A. Ostrowski, S. Fuchs, A. Behr, Catalyst recycling in the hydroaminomethylation of methyl oleate: A route to novel polyamide monomers, *Eur. J. Lipid Sci. Technol* **2017**, *119*, 1600211.

[117] T. A. Faßbach, F. O. Sommer, A. J. Vorholt, Hydroaminomethylation in Aqueous Solvent Systems - An Efficient Pathway to Highly Functionalized Amines, *Adv. Synth. Catal.* **2018**, *360*, 1473–1482.

[118] K. U. Künnemann, D. Weber, C. Becquet, S. Tilloy, E. Monflier, T. Seidensticker, D. Vogt, Aqueous Biphasic Hydroaminomethylation Enabled by Methylated Cyclodextrins: Sensitivity Analysis for Transfer into a Continuous Process, *ACS Sustainable Chemistry & Engineering* **2021**, *9*, 273–283.

[119] J. Harvey, *Computational Chemistry*, Oxford University Press, Oxford, UK, **2018**.

[120] M. Born, R. Oppenheimer, Zur Quantentheorie der Molekeln, *Ann. Phys.* **1927**, *389*, 457–484.

[121] D. R. Hartree, The Wave Mechanics of an Atom with a Non-Coulomb Central Field. Part I. Theory and Methods, *Mathematical Proceedings of the Cambridge Philosophical Society* **1928**, *24*, 89–110.

[122] V. Fock, Näherungsmethode zur Lösung des quantenmechanischen Mehrkörperproblems, *Z. Phys.* **1930**, *61*, 126–148.

[123] D. R. Hartree, W. Hartree, Self-consistent field, with exchange, for beryllium, *Proceedings of the Royal Society of London. Series A - Mathematical and Physical Sciences* **1935**, *150*, 9–33.

[124] R. J. Bartlett, M. Musiał, Coupled-cluster theory in quantum chemistry, *Rev. Mod. Phys.* **2007**, *79*, 291–352.

[125] C. Bannwarth, S. Ehlert, S. Grimme, GFN2-xTB-An Accurate and Broadly Parametrized Self-Consistent Tight-Binding Quantum Chemical Method with Multipole Electrostatics and Density-Dependent Dispersion Contributions, *J. Chem. Theory Comput.* **2019**, *15*, 1652–1671.

[126] S. tai Guo, J. Liu, W. Qian, W. hua Zhu, C. yang Zhang, A review of quantum chemical methods for treating energetic molecules, *Energ. Mater. Front.* **2021**, *2*, 292–305.

[127] P. Hohenberg, W. Kohn, Inhomogeneous Electron Gas, *Phys. Rev.* **1964**, *136*, B864–B871.

[128] W. Kohn, L. J. Sham, Self-Consistent Equations Including Exchange and Correlation Effects, *Phys. Rev.* **1965**, *140*, A1133–A1138.

[129] G. L. Oliver, J. P. Perdew, Spin-density gradient expansion for the kinetic energy, *Phys. Rev. A* **1979**, *20*, 397–403.

[130] O. Gunnarsson, B. I. Lundqvist, Exchange and correlation in atoms, molecules, and solids by the spin-density-functional formalism, *Phys. Rev. B* **1976**, *13*, 4274–4298.

[131] J. Sun, M. Marsman, G. I. Csonka, A. Ruzsinszky, P. Hao, Y.-S. Kim, G. Kresse, J. P. Perdew, Self-consistent meta-generalized gradient approximation within the projector-augmented-wave method, *Phys. Rev. B* **2011**, *84*, 035117.

[132] A. D. Becke, Density-functional exchange-energy approximation with correct asymptotic behavior, *Phys. Rev. A* **1988**, *38*, 3098–3100.

[133] J. P. Perdew, Density-functional approximation for the correlation energy of the inhomogeneous electron gas, *Phys. Rev. B* **1986**, *33*, 8822–8824.

[134] C. Cramer, *Essentials of Computational Chemistry: Theories and Models*, Wiley-VCH, Weinheim Germany, **2004**.

[135] P. A. M. Dirac, R. H. Fowler, Quantum mechanics of many-electron systems, *Proc. R. Soc. London A.* **1929**, *123*, 714–733.

[136] J. C. Slater, A Simplification of the Hartree-Fock Method, *Phys. Rev.* **1951**, *81*, 385–390.

[137] S. H. Vosko, L. Wilk, M. Nusair, Accurate spin-dependent electron liquid correlation energies for local spin density calculations: a critical analysis, *Canad. J. Phys.* **1980**, *58*, 1200–1211.

[138] S. Grimme, Accurate description of van der Waals complexes by density functional theory including empirical corrections, *J. Comp. Chem.* **2004**, *25*, 1463–1473.

[139] M. Ernzerhof, G. E. Scuseria, Assessment of the Perdew-Burke-Ernzerhof exchange-correlation functional, *J. Chem. Phys.* **1999**, *110*, 5029–5036.

[140] J. P. Perdew, K. Burke, M. Ernzerhof, Generalized Gradient Approximation Made Simple, *Phys. Rev. Lett.* **1997**, *78*, 1396–1396.

[141] S. Dohm, A. Hansen, M. Steinmetz, S. Grimme, M. P. Checinski, Comprehensive Thermochemical Benchmark Set of Realistic Closed-Shell Metal Organic Reactions, *J. Chem. Theory Comput.* **2018**, *14*, 2596–2608.

[142] S. Grimme, Semiempirical hybrid density functional with perturbative second-order correlation, *J. Chem. Phys.* **2006**, *124*, 034108.

[143] L. A. Curtiss, K. Raghavachari, P. C. Redfern, J. A. Pople, Assessment of Gaussian-2 and density functional theories for the computation of enthalpies of formation, *J. Chem. Phys.* **1997**, *106*, 1063–1079.

[144] L. Goerigk, S. Grimme, Double-hybrid density functionals, *WIREs Comput. Mol. Sci.* **2014**, *4*, 576–600.

[145] S. Grimme, A. Hansen, J. G. Brandenburg, C. Bannwarth, Dispersion-Corrected Mean-Field Electronic Structure Methods, *Chem. Rev.* **2016**, *116*, 5105–5154.

[146] S. Grimme, Density functional theory with London dispersion corrections, *WIREs Comput. Mol. Sci.* **2011**, *1*, 211–228.

[147] S. Grimme, J. Antony, S. Ehrlich, H. Krieg, A consistent and accurate ab initio parametrization of density functional dispersion correction (DFT-D) for the 94 elements H-Pu, *J. Chem. Phys.* **2010**, *132*, 154104.

[148] S. Grimme, S. Ehrlich, L. Goerigk, Effect of the damping function in dispersion corrected density functional theory, *J. Comp. Chem.* **2011**, *32*, 1456–1465.

[149] S. Grimme, J. Antony, S. Ehrlich, H. Krieg, A consistent and accurate ab initio parametrization of density functional dispersion correction (DFT-D) for the 94 elements H-Pu, *J. Chem. Phys.* **2010**, *132*, 154104.

[150] W. Koch, M. C. Holthausen, "Electron Density and Hole Functions" in *A Chemist's Guide to Density Functional Theory*, Wiley-VCH, Weinheim, Germany, **2001**, 19–28.

[151] P. Debye, Näherungsformeln für die Zylinderfunktionen für große Werte des Arguments und unbeschränkt veränderliche Werte des Index, *Math. Ann.* **1909**, *67*, 535–558.

[152] M. Hestenes, E. Stiefel, Methods of conjugate gradients for solving linear systems, *J. Res. Natl. Bur. Stand.* **1952**, *49*, 409.

[153] T. Helgaker, Transition-state optimizations by trust-region image minimization, *Chem. Phys. Lett.* **1991**, *182*, 503–510.

[154] F. Jameel, F. Huxoll, M. Stein, G. Sadowski, "Solvent selection for reactions in liquid phases" in *Integrated Chemical Processes in Liquid Multiphase Systems: From Chemical Reaction to Process Design and Operation*, (Eds.: M. Kraume, S. Enders, A. Drews, R. Schomäcker, S. Engell, K. Sundmacher), De Gruyter, Berlin, Germany, **2022**, 509–574.

[155] M. Born, Volumen und Hydratationswärme der Ionen, *Zeitschrift für Physik* **1920**, *1*, 45–48.

[156] S. Miertuš, E. Scrocco, J. Tomasi, Electrostatic interaction of a solute with a continuum. A direct utilizaion of AB initio molecular potentials for the prevision of solvent effects, *J. Chem. Phys.* **1981**, *55*, 117–129.

[157] B. Lee, F. Richards, The interpretation of protein structures: Estimation of static accessibility, *J. Mol. Bio.* **1971**, *55*, 379–IN4.

[158] R. B. Hermann, Theory of hydrophobic bonding. II. Correlation of hydrocarbon solubility in water with solvent cavity surface area, *J. Phys. Chem.* **1972**, *76*, 2754–2759.

[159] C. J. Cramer, D. G. Truhlar, Implicit Solvation Models: Equilibria, Structure, Spectra, and Dynamics, *Chem. Rev.* **1999**, *99*, 2161–2200.

[160] A. Klamt, G. Schüürmann, COSMO: a new approach to dielectric screening in solvents with explicit expressions for the screening energy and its gradient, *J. Chem. Soc., Perkin Trans. 2* **1993**, 799–805.

[161] A. Klamt, V. Jonas, T. Bürger, J. C. W. Lohrenz, Refinement and Parametrization of COSMO-RS, *J. Phys. Chem. A* **1998**, *102*, 5074–5085.

[162] A. Klamt, The COSMO and COSMO-RS solvation models, *WIREs Comput. Mol. Sci.* **2018**, *8*, e1338.

[163] J. R. Pliego, J. M. Riveros, The Cluster-Continuum Model for the Calculation of the Solvation Free Energy of Ionic Species, *J. Phys. Chem. A* **2001**, *105*, 7241–7247.

[164] M. Bursch, J.-M. Mewes, A. Hansen, S. Grimme, Best-Practice DFT Protocols for Basic Molecular Computational Chemistry, *Angew. Chem. Int. Ed.* **2022**, *61*, e202205735.

[165] M. Orozco, F. J. Luque, Theoretical Methods for the Description of the Solvent Effect in Biomolecular Systems, *Chem. Rev.* **2000**, *100*, 4187–4226.

[166] K. Liu, M. G. Brown, C. Carter, R. J. Saykally, J. K. Gregory, D. C. Clary, Characterization of a cage form of the water hexamer, *Nat. Chem.* **1996**, *381*, 501–503.

[167] de Oliveira, Luís P., Hudebine, Damien, Guillaume, Denis, Verstraete, Jan J., A Review of Kinetic Modeling Methodologies for Complex Processes, *Oil Gas Sci. Technol. - Rev. IFP Energies nouvelles* **2016**, *71*, 45.

[168] H. Eyring, The Activated Complex and the Absolute Rate of Chemical Reactions. *Chem. Rev.* **1935**, *17*, 65–77.

[169] L. E. Rush, P. G. Pringle, J. N. Harvey, Computational Kinetics of Cobalt-Catalyzed Alkene Hydroformylation, *Angew. Chem. Int. Ed.* **2014**, *53*, 8672–8676.

[170] K. J. Laidler, J Keith, et al., *Chemical kinetics*, *Vol. 2*, McGraw-Hill New York, **1965**.

[171] J. N. Harvey, F. Himo, F. Maseras, L. Perrin, Scope and Challenge of Computational Methods for Studying Mechanism and Reactivity in Homogeneous Catalysis, *ACS Catal.* **2019**, *9*, 6803–6813.

[172] F. Jameel, M. Stein, Solvent effects in hydroformylation of long-chain olefins, *Mol. Catal.* **2021**, *503*, 111429.

[173] M. Gerlach, F. Jameel, A. Seidel-Morgenstern, M. Stein, C. Hamel, Operando characterization of rhodium catalyst degradation in hydroformylation, *Catal. Sci. Technol.* **2023**, *13*, 1788–1801.

[174] M. Gerlach, S. Kirschtowski, F. Huxoll, M. Stein, G. Sadowski, A. Seidel-Morgenstern, "Thermodynamics, Kinetics, and Mass Transfer" in *Integrated Chemical Processes in Liquid Multiphase Systems: From Chemical Reaction to Process Design and Operation*, (Eds.: M. Kraume, S. Enders, A. Drews, R. Schomäcker, S. Engell, K. Sundmacher), De Gruyter, Berlin, Germany, **2022**, 55–188.

[175] H. Hock, A. Neuwirth, Autoxydation von Kohlenwasserstoffen: Über Peroxyde aus offenkettigen Olefinen und von Olefinen eines technischen Spaltbenzins (III. Mitteil.) *Ber. Dtsch. Chem. Ges.* **1939**, *72*, 1562–1568.

[176] K. Schwetlick, W. D. Habicher, Organophosphorus antioxidants action mechanisms and new trends, *Angew. Makromolek. Chem.* **1995**, *232*, 239–246.

[177] H. Brandl, E. Täuscher, D. Weiß, Keine Angst vor Peroxiden, *Chemie in unserer Zeit* **2016**, *50*, 130–139.

[178] M. Gerlach, D. Abdul Wajid, L. Hilfert, F. T. Edelmann, A. Seidel-Morgenstern, C. Hamel, Impact of minor amounts of hydroperoxides on rhodium-catalyzed hydroformylation of long-chain olefins, *Catal. Sci. Technol.* **2017**, *7*, 1465–1469.

[179] A. Behr, C. Fängewisch, Rhodium-catalysed synthesis of branched fatty compounds in temperature-dependent solvent systems, *J. Mol. Catal. A: Chem.* **2003**, *197*, 115–126.

[180] K. McBride, T. Gaide, A. Vorholt, A. Behr, K. Sundmacher, Thermomorphic solvent selection for homogeneous catalyst recovery based on COSMO-RS, *Chem. Eng. Process. Process Intensif.* **2016**, *99*, 97–106.

[181] S. REACH, Candidate list of substances of very high concern for authorisation, *environment (Article 57 f)* **2014**, *17*, 12.

[182] F. Helfferich, "Tools for reduction of complexity" in *Kinetics of Multistep Reactions, 2nd Edition*, (Ed.: N. Green), Comprehensive Chemical Kinetics, Elsevier, Amsterdam, Netherlands, **2004**, 77–93.

[183] D. Evans, J. A. Osborn, G. Wilkinson, Hydroformylation of alkenes by use of rhodium complex catalysts, *J. Chem. Soc. A* **1968**, 3133–3142.

[184] G. Kiedorf, D. Hoang, A. Müller, A. Jörke, J. Markert, H. Arellano-Garcia, A. Seidel-Morgenstern, C. Hamel, Kinetics of 1-dodecene hydroformylation in a thermomorphic solvent system using a rhodium-biphephos catalyst, *Chem. Eng. Sci.* **2014**, *115*, 31–48.

[185] J. Markert, Y. Brunsch, T. Munkelt, G. Kiedorf, A. Behr, C. Hamel, A. Seidel-Morgenstern, Analysis of the reaction network for the Rh-catalyzed hydroformylation of 1-dodecene in a thermomorphic multicomponent solvent system, *Appl. Catal. A* **2013**, *462-463*, 287–295.

[186] L. A. van der Veen, P. H. Keeven, G. C. Schoemaker, J. N. H. Reek, P. C. J. Kamer, P. W. N. M. van Leeuwen, M. Lutz, A. L. Spek, Origin of the Bite Angle Effect on Rhodium Diphosphine Catalyzed Hydroformylation, *Organometallics* **2000**, *19*, 872–883.

[187] A. Jörke, T. Gaide, A. Behr, A. Vorholt, A. Seidel-Morgenstern, C. Hamel, Hydroformylation and tandem isomerization-hydroformylation of n-decenes using a rhodium-BiPhePhos catalyst: Kinetic modeling, reaction network analysis and optimal reaction control, *Chem. Eng. J.* **2017**, *313*, 382–397.

[188] J. M. Dreimann, E. Kohls, H. F. W. Warmeling, M. Stein, L. F. Guo, M. Garland, T. N. Dinh, A. J. Vorholt, In Situ Infrared Spectroscopy as a Tool for Monitoring Molecular Catalyst for Hydroformylation in Continuous Processes, *ACS Catal.* **2019**, *9*, 4308–4319.

[189] J. Bianga, K. U. Künnemann, T. Gaide, A. J. Vorholt, T. Seidensticker, J. M. Dreimann, D. Vogt, Thermomorphic Multiphase Systems: Switchable Solvent Mixtures for the Recovery of Homogeneous Catalysts in Batch and Flow Processes, *Chem. Eur. J.* **2019**, *25*, 11586–11608.

[190] E. Kohls, M. Stein, The thermochemistry of long chain olefin isomers during hydroformylation, *New J. Chem.* **2017**, *41*, 7347–7355.

[191] A. Jörke, E. Kohls, S. Triemer, A. Seidel-Morgenstern, C. Hamel, M. Stein, Resolution of structural isomers of complex reaction mixtures in homogeneous catalysis, *Chem. Eng. Process. Process Intensif.* **2016**, *102*, 229–237.

[192] E. Kohls, M. Stein, Vibrational scaling factors for Rh (I) carbonyl compounds in homogeneous catalysis, *Cont. Sec. Nat. Math. Biotech. Sci.* **2017**, *38*, 43–56.

[193] A. van Rooy, P. C. J. Kamer, P. W. N. M. van Leeuwen, K. Goubitz, J. Fraanje, N. Veldman, A. L. Spek, Bulky Diphosphite-Modified Rhodium Catalysts: Hydroformylation and Characterization, *Organometallics* **1996**, *15*, 835–847.

[194] A. Bara-Estaún, C. L. Lyall, J. P. Lowe, P. G. Pringle, P. C. J. Kamer, R. Franke, U. Hintermair, Mapping catalyst activation, turnover speciation and deactivation in Rh/PPh3-catalysed olefin hydroformylation, *Catal. Sci. Technol.* **2022**, *12*, 5501–5516.

[195] M. Lemberg, G. Sadowski, M. Gerlach, E. Kohls, M. Stein, C. Hamel, A. Seidel-Morgenstern, Predicting solvent effects on the 1-dodecene hydroformylation reaction equilibrium, *AIChE J.* **2017**, *63*, 4576–4585.

[196] R. Jana, J. A. Tunge, A Homogeneous, recyclable rhodium (I) catalyst for the hydroarylation of Michael acceptors, *Org. Lett.* **2009**, *11*, 971–974.

[197] T. Hamerla, A. Rost, Y. Kasaka, R. Schomäcker, Hydroformylation of 1-Dodecene with Water-Soluble Rhodium Catalysts with Bidentate Ligands in Multiphase Systems, *ChemCatChem* **2013**, *5*, 1854–1862.

[198] J. Bianga, N. Herrmann, L. Schurm, T. Gaide, J. M. Dreimann, D. Vogt, T. Seidensticker, Improvement of Productivity for Aqueous Biphasic Hydroformylation of Methyl 10-Undecenoate: A Detailed Phase Investigation, *Eur. J. Lip. Sci. Technol.* **2020**, *122*, 1900317.

[199] F. Jameel, M. Stein, The many roles of solvent in homogeneous catalysis - The reductive amination showcase, *J. Catal.* **2022**, *405*, 24–34.

[200] F. Huxoll, F. Jameel, J. Bianga, T. Seidensticker, M. Stein, G. Sadowski, D. Vogt, Solvent Selection in Homogeneous Catalysis—Optimization of Kinetics and Reaction Performance, *ACS Catal.* **2021**, *11*, 590–594.

[201] W. S. Emerson, "The Preparation of Amines by Reductive Alkylation" in *Organic Reactions*, Wiley-VCH, Weinheim, Germany, **2011**, Chapter 3, 174–255.

[202] E. Boz, N. Tüzün, M. Stein, Computational investigation of the control of the thermodynamics and microkinetics of the reductive amination reaction by solvent coordination and a co-catalyst, *RSC Adv.* **2018**, *8*, 36662–36674.

[203] T. Senthamarai, K. Murugesan, J. Schneidewind, N. Kalevaru, W. Baumann, H. Neumann, P. Kamer, M. Beller, R. Jagadeesh, *Nat. Commun.* **2018**, *9*, 1–12.

[204] J. Hine, F. A. Via, J. K. Gotkis, J. C. J. Craig, Kinetics of the formation of N-isobutylidenemethylamine from isobutyraldehyde and methylamine in aqueous solution, *J. Am. Chem. Soc.* **1970**, *92*, 5186–5193.

[205] S. Ding, N. Jiao, N,N-Dimethylformamide: A Multipurpose Building Block, *Angew. Chem. Int. Ed.* **2012**, *51*, 9226–9237.

[206] M. M. Heravi, M. Ghavidel, L. Mohammadkhani, Beyond a solvent: triple roles of dimethylformamide in organic chemistry, *RSC Adv.* **2018**, *8*, 27832–27862.

[207] M. Tobiszewski, S. Tsakovski, V. Simeonov, J. Namieśnik, F. Pena-Pereira, A solvent selection guide based on chemometrics and multicriteria decision analysis, *Green Chem.* **2015**, *17*, 4773–4785.

[208] J. Bianga, K. U. Künnemann, L. Goclik, L. Schurm, D. Vogt, T. Seidensticker, Tandem Catalytic Amine Synthesis from Alkenes in Continuous Flow Enabled by Integrated Catalyst Recycling, *ACS Catal.* **2020**, *10*, 6463–6472.

[209] W. Kortuz, S. Kirschtowski, A. Seidel-Morgenstern, C. Hamel, Mechanistic kinetic modeling of the rhodium-catalyzed tandem hydroaminomethylation of 1-decene in a thermomorphic solvent system, *Catal. Commun.* **2023**, *177*, 106633.

[210] K. H. Rätze, W. Kortuz, S. Kirschtowski, M. Jokiel, C. Hamel, K. Sundmacher, Optimal experimental design for the identification of a reaction kinetic model for the hydroaminomethylation of 1-decene in a thermomorphic multiphase system, *Chem. Eng. J.* **2023**, *469*, 143713.

[211] P. W. N. M. van Leewen, "Hydroformylation, Hydrocarbonylation, Hydrocyanation, and Hydroacylation of Carbon—Carbon Double Bonds" in *Science of Synthesis, 1: Stereoselective Synthesis 1*, (Ed.: de Vries), Georg Thieme Verlag, Leipzig, Germany, **2011**, 409–466.

[212] L. A. van der Veen, M. D. K. Boele, F. R. Bregman, P. C. J. Kamer, P. W. N. M. van Leeuwen, K. Goubitz, J. Fraanje, H. Schenk, C. Bo, Electronic Effect on Rhodium Diphosphine Catalyzed Hydroformylation: The Bite Angle Effect Reconsidered, *J. Am. Chem. Soc.* **1998**, *120*, 11616–11626.

[213] E. Zuidema, L. Escorihuela, T. Eichelsheim, J. J. Carbó, C. Bo, P. C. J. Kamer, P. W. N. M. van Leeuwen, The Rate-Determining Step in the Rhodium-Xantphos-Catalysed Hydroformylation of 1-Octene, *Chem. Eur. J.* **2008**, *14*, 1843–1853.

[214] H. Tricas, O. Diebolt, P. W. van Leeuwen, Bulky monophosphite ligands for ethene hydroformylation, *J. Catal.* **2013**, *298*, 198–205.

[215] J. Ternel, J.-L. Couturier, J.-L. Dubois, J.-F. Carpentier, Rhodium-Catalyzed Tandem Isomerization/Hydroformylation of the Bio-Sourced 10-Undecenenitrile: Selective and Productive Catalysts for Production of Polyamide-12 Precursor, *Adv. Synth. Catal.* **2013**, *355*, 3191–3204.

[216] T. Gaide, J. M. Dreimann, A. Behr, A. J. Vorholt, Overcoming Phase-Transfer Limitations in the Conversion of Lipophilic Oleo Compounds in Aqueous Media—A Thermomorphic Approach, *Angew. Chem. Int. Ed.* **2016**, *55*, 2924–2928.

[217] S. Schlüter, K. U. Künnemann, M. Freis, T. Roth, D. Vogt, J. M. Dreimann, M. Skiborowski, Continuous co-product separation by organic solvent nanofiltration for the hydroaminomethylation in a thermomorphic multiphase system, *Chem. Eng. J.* **2021**, *409*, 128219.

[218] T. A. Faßbach, T. Gaide, M. Terhorst, A. Behr, A. J. Vorholt, Renewable Surfactants through the Hydroaminomethylation of Terpenes, *ChemCatChem* **2017**, *9*, 1359–1362.

[219] D. Crozet, C. E. Kefalidis, M. Urrutigoïty, L. Maron, P. Kalck, Hydroaminomethylation of Styrene Catalyzed by Rhodium Complexes Containing Chiral Diphosphine Ligands and Mechanistic Studies: Why Is There a Lack of Asymmetric Induction?, *ACS Catal.* **2014**, *4*, 435–447.

[220] T. Gensch, G. dos Passos Gomes, P. Friederich, et al., A Comprehensive Discovery Platform for Organophosphorus Ligands for Catalysis, *J. Am. Chem. Soc.* **2022**, *144*, 1205–1217.

[221] S. Gallarati, P. van Gerwen, R. Laplaza, S. Vela, A. Fabrizio, C. Corminboeuf, OSCAR: an extensive repository of chemically and functionally diverse organocatalysts, *Chem. Sci.* **2022**, *13*, 13782–13794.

[222] TURBOMOLE V7.2 2017, a development of University of Karlsruhe and Forschungszentrum Karlsruhe GmbH, 1989-2007, TURBOMOLE GmbH, since 2007; available from http://www.turbomole.com, **2007**.

[223] F. Neese, The ORCA program system, *WIREs Comput. Mol. Sci.* **2012**, *2*, 73–78.

[224] F. Neese, Software update: the ORCA program system, version 4.0, *WIREs Comput. Mol. Sci.* **2018**, *8*, e1327.

[225] A. D. Becke, Density-functional exchange-energy approximation with correct asymptotic behavior, *Phys. Rev. A* **1988**, *38*, 3098–3100.

[226] J. P. Perdew, Density-functional approximation for the correlation energy of the inhomogeneous electron gas, *Phys. Rev. B* **1986**, *33*, 8822–8824.

[227] J. Tao, J. P. Perdew, V. N. Staroverov, G. E. Scuseria, Climbing the Density Functional Ladder: Nonempirical Meta–Generalized Gradient Approximation Designed for Molecules and Solids, *Phys. Rev. Lett.* **2003**, *91*, 146401.

[228] S. Grimme, Semiempirical hybrid density functional with perturbative second-order correlation, *J. Chem. Phys.* **2006**, *124*, 034108.

[229] C. Riplinger, B. Sandhoefer, A. Hansen, F. Neese, Natural triple excitations in local coupled cluster calculations with pair natural orbitals, *J. Chem. Phys.* **2013**, *139*, 134101.

[230] C. Riplinger, P. Pinski, U. Becker, E. F. Valeev, F. Neese, Sparse maps—A systematic infrastructure for reduced-scaling electronic structure methods. II. Linear scaling domain based pair natural orbital coupled cluster theory, *J. Chem. Phys.* **2016**, *144*, 024109.

[231] A. Schäfer, C. Huber, R. Ahlrichs, Fully optimized contracted Gaussian basis sets of triple zeta valence quality for atoms Li to Kr, *J. Chem. Phys.* **1994**, *100*, 5829–5835.

[232] K. Eichkorn, O. Treutler, H. Öhm, M. Häser, R. Ahlrichs, Auxiliary basis sets to approximate Coulomb potentials, *Chem. Phys. Lett.* **1995**, *240*, 283–290.

[233] K Eichkorn, O Treutler, HÖhm, M Häser, R Ahlrichs, Auxiliary basis sets to approximate Coulomb potentials, *Chem. Phys. Lett.* **1995**, *242*, 652–660.

[234] J. J. Stewart, L. P. Davis, L. W. Burggraf, Semi-empirical calculations of molecular trajectories: Method and applications to some simple molecular systems, *J. Comp. Chem.* **1987**, *8*, 1117–1123.

[235] A. Hellweg, F. Eckert, Brick by brick computation of the gibbs free energy of reaction in solution using quantum chemistry and COSMO-RS, *AIChE J.* **2017**, *63*, 3944–3954.

[236] A. E. Reed, R. B. Weinstock, F. Weinhold, Natural population analysis, *J. Chem. Phys.* **1985**, *83*, 735–746.

[237] L. Goerigk, A. Hansen, C. Bauer, S. Ehrlich, A. Najibi, S. Grimme, A look at the density functional theory zoo with the advanced GMTKN55 database for general main group thermochemistry, kinetics and noncovalent interactions, *Phys. Chem. Chem. Phys.* **2017**, *19*, 32184–32215.

[238] F. Furche, J. P. Perdew, The performance of semilocal and hybrid density functionals in 3 d transition-metal chemistry, *J. Chem. Phys.* **2006**, *124*, 044103.

[239] W. Jiang, M. L. Laury, M. Powell, A. K. Wilson, Comparative study of single and double hybrid density functionals for the prediction of 3d transition metal thermochemistry, *J. Chem. Theory Comput.* **2012**, *8*, 4102–4111.

[240] T. Weymuth, E. P. Couzijn, P. Chen, M. Reiher, New benchmark set of transition-metal coordination reactions for the assessment of density functionals, *J. Chem. Theory Comput.* **2014**, *10*, 3092–3103.

List of Figures

List of Tables

Appendix

Computational Details

A

DFT calculations were carried out using TURBOMOLE v 7.4 [222], expect for the calculations for PWPB95 double hybrid and DLPNO-CCSD(T), which were performed with ORCA version 4.0.1.[223, 224] PBE0 [138, 139], hybrid density functional with Grimmes' dispersion correction [147] and the Becke-Johnson damping [148], has been selected as the most appropriate functional after performing benchmark studies, (See Appendix B). Additional density functionals such as BP86[225, 226], TPSS[227] and RI-PWPB95[228] including D3 dispersion corrections, in addition, semi-empirical GFN2-xtb [125] were also explored, to compare the performance of each method against standard DLPNO-CCSD(T) [229, 230] reaction energies.

Ahlrichs' triple-ζ valance polarization [231] (def2-TZVP) basis set was used for all DFT calculations. Geometry optimizations were completed with symmetry constraints in gas phase with strict scf convergence (10^{-8}) criteria using a fine m^4 grid. The resolution of identity approximation [232, 233] was applied using auxiliary def2-TZVP basis set to approximate the Coulomb potentials. Each optimized structure, had a frequency analysis performed on it, with the same setting used for geometry optimizations. The frequency analysis allows the nature of the structure to be determined, either as a minima (with no negative frequencies) or a transition state having only one imaginary frequency.

Zero point vibrational energies were calculated from the corresponding harmonic vibrational frequencies with a scaling factor of 1.00. The scaling factor for the vibrational frequencies was derived from a training set of Rh(I)carbonyl complexes using BP86 and B3LYP functional [192]. Relative Gibbs free energies were calculated at the reaction conditions of 378 K and 20 bar for hydroformylation and 373 K and 30 bar for reductive amination, respectively. The thermodynamic correction for all species were evaluated with in the rigid-rotor harmonic-oscillator approximation.

The initial guess for transition state structures were made by through relaxed energy scans along the reaction coordinate. The single negative frequency correspond to the formation/breakage of the bond along the reaction coordinate. In addition, frequency calculations also allows the estimation of thermodynamic corrections, thus enabling the calculation of Gibbs free energies at any given temperature and pressure. Dynamic reaction coordinate scans[234] (DRC) were performed along the reaction coordinate by following the imaginary vibration mode in both directions to verify the connectivity of the transition state with the reactants and products, respectively.

Structures with numerical noise (small negative frequencies) were undergone addition calculations in an attempt to remove the negative frequency to reach true minima on the potential energy surface (PES). The first step taken for each structure

with small negative frequencies was to distort the structure along the vibrational mode of the negative frequency and optimizing it again. This was achieved either with the "Screwer" option available in TURBOMOLE or by manual displacement using the default molecular editor TmoleX.

Solvent effects were calculated using a cluster-continuum model where the solvent molecules in the first solvation shell are explicitly considered at the DFT level. The optimum number of explicit solvent molecules was estimated using the approach suggested by Pliego and Riveros[163], see section 3.2.3. The implicit COSMO (Conductor like Solvation MOdel) [160] and COSMO-RS (Conductor like Screening Model for Real Solvents) [161] V.19.0.4 (R 5514) at the BP86/TZVPD-FINE with BP_TZVPD_FINE_19 parameters were used to represent bulk solvent effects. Single point COSMO calculations were performed at the same level of theory (PBE0(D3)/def2-TZVP), at which the structures were optimized using the respective dielectric constant.

Gibbs free energies of solvation were calculated using the standard COSMO-RS procedure.[235] ΔG_{solv} is the change in Gibbs free energy from the pure compound gas phase to the solvated phase, with a reference state of 1 mol/L in both phases. Gibbs free energies of solvation were calculated at infinite dilution using different experimental solvent compositions of methanol:dodecane 50:50 and 99:01 (w/w) solution.

Atomic charges of the optimized structures were calculated using natural population analysis (NPA).[236]

B

Computational Method Selection

Among the methods discussed in chapter 3.1 for the calculations of electronic energy of large molecules density functional theory (DFT) is found to be the method of choice due to its reasonable computation costs and accuracy. However, there do exist a vast number of density functionals [237] based on different approximations employed for the estimation of exchange-correlation term (See section 3.1.2). DFT estimated Gibbs free energies are functional dependent therefore, for accurate reaction energies and activation energy barriers for transition states it is necessary to perform benchmark studies. There do exist a number of benchmark studies to find appropriate density functional however, they lack investigation of transition state elements for example, GMTK55 database [237] only consist of molecules formed by main group elements. Transition metal elements are considered in the benchmark studies of Furch and Perdew however they have mostly considered small sized pure inorganic reactions such as the dissociation of chromium dimer.[238] Jiang and co-workers have presented a benchmark set named as ccCATM/11, which consist of 225 first row transition metal small medium sized compounds (< 36 atoms) however, there methodology is not applicable on the large system.[239] Large organometallic compounds including late transition metals routinely used in homogeneous catalysis are for example included in the WCCR10 database by Weymuth and co-workers[240] and MOR41 by Dohm and co-workers.[141] The performance of large number of density functionals is evaluated in both of aforementioned studies.

For the benchmark calculations in this work, reactions σ donation, π acceptor, ligand exchange and dimerization reactions involving rhodium as central transition metal were considered in addition to H_2 oxidative addition for an electron donating phosphine XantPhos and an electron with-drawing phosphite BiPhePhos species (See Figure B.1).

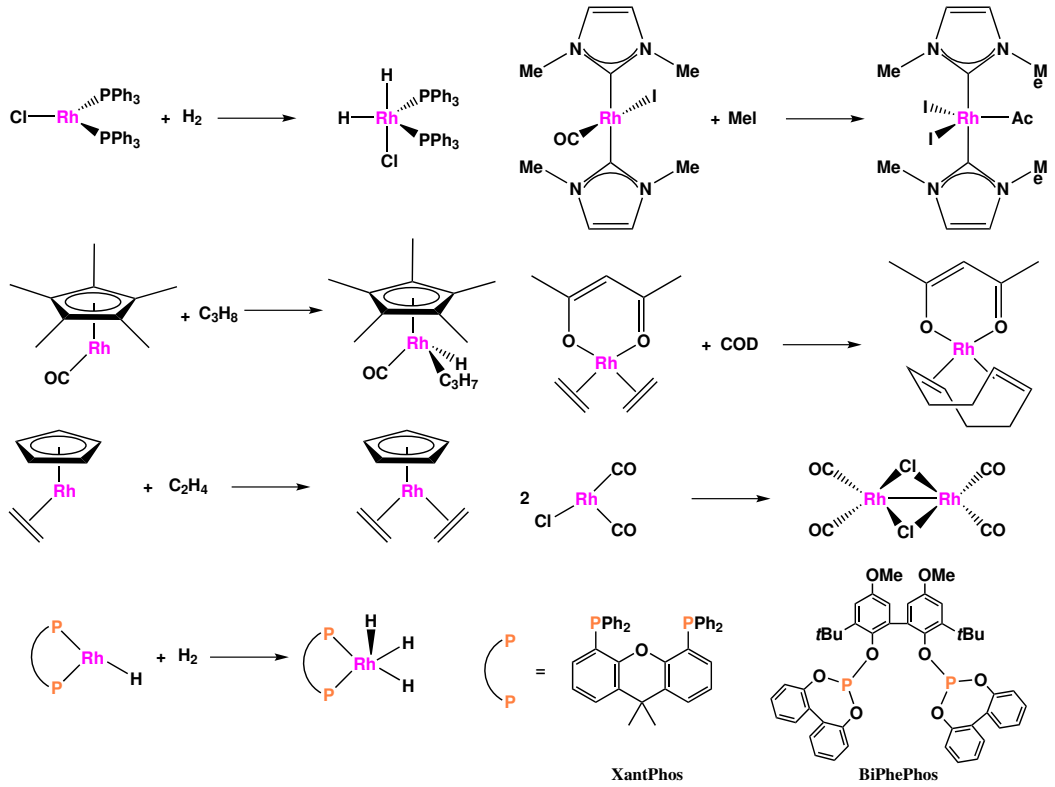

Fig. B.1.: Benchmark set for typical chemical reactions performed by rhodium(I) catalysts.

The performance of semi-empirical DFT method (GFN2-xtb) and best performing density functional at every level of theory from MOR41 benchmark set was estimated for above mentioned reactions. The mean absolute deviation in the reaction energies was compared to standard DLPNO-CCSD(T)/def2-QZVPP level of theory (see Figure B.2). The highest deviation of 83 kJ/mol from the standard CCSD(T) energies was observed for semi-empirical GFN2-xTB method. The mean absolute deviation significantly reduces from 83 to 16 kJ/mol when using dispersion corrected generalized GGA type BP86 functional. Meta-GGA type (TPSS) functional perform slightly better than BP86. Surprisingly double hybrid PWPB95 density function does not have a significant effect of the reaction energy for the reaction benchmark set with a MAD of 13 kJ/mol. However, among all test density function hybrid PBE0 functional with D3 dispersion correction give the lowest deviation from the DLPND-CCS(T) energies thus, it is most appropriate density function for the calculating reaction energies involving closed-shell rhodium complexes.

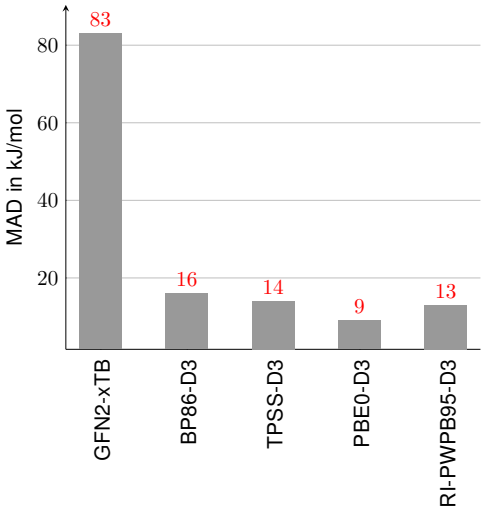

Fig. B.2.: The mean absolute deviation (MAD) in kJ/mol from DLPNO-CCSD(T) calculations for a variety of density functional and semi-empirical xTB method.

C

PES in Different Solvent Compositions

C.1 PES of Hyfo in Different solvent Compositions

C.2 PES of RA in Different solvent Compositions

Tab. C.1.: Gibbs free energy of all intermediates and transition states along n-hydroformylation pathway leading to 1-Undecanal in gas and DMF/dodecane solvent mixtures using (BPP)HRh-CO catalyst. All energies are in kJ/mol relative to catalyst resting state 1*. The free energy of solvation were calculated using implicit solvent model COSMO-RS.

Methanol/dodecane Composition	Gas phase	(100/0)	(70/30)	(50/50)	(30/70)	(0/100)
1*	0	0	0	0	0	0
1	84.22	83.66	83.69	84.13	84.78	85.28
2	38.65	51.03	52.08	51.72	51.32	51.00
TS 2→3n	83.86	93.84	95.57	95.49	95.55	95.68
3n	52.10	61.43	61.57	60.91	60.29	59.82
4n	10.37	15.68	15.69	14.78	13.79	12.99
TS 4n→5n	39.76	44.50	45.08	44.75	44.36	44.03
5n	3.31	8.16	9.62	9.38	9.08	8.85
6n	36.62	35.95	36.23	35.27	34.25	33.69
TS 6n→7n	37.95	37.82	38.00	36.99	35.91	35.27
7n	11.61	10.69	11.00	10.38	9.78	9.50
TS 7n→Undecanal	55.60	60.17	61.00	60.09	58.91	58.07
Undecanal	1.71	-16.63	-16.02	-15.40	-14.23	-13.06

Tab. C.2.: Gibbs free energy of all intermediates and transition states along branched+isomer. pathway leading to 2iso in gas and DMF/dodecane solvent mixtures using (BPP)HRh-CO catalyst. All energies are in kJ/mol relative to catalyst resting state 1*. The free energy of solvation were calculated using implicit solvent model COSMO-RS.

Methanol/dodecane Composition	Gas phase	(100/0)	(70/30)	(50/50)	(30/70)	(0/100)
1*	0	0	0	0	0	0
1	84.22	83.66	83.69	84.13	84.78	85.28
2	38.65	51.028	52.08	51.72	51.32	51.00
TS 2→3b	94.10	100.17	101.63	101.58	101.59	101.66
3b	62.57	70.97	72.11	71.95	71.79	71.65
3iso	74.97	83.42	84.67	84.50	84.32	84.16
TS 3iso→2iso	104.50	112.79	114.13	113.97	113.84	113.74
2iso	50.56	62.15	63.28	62.96	62.57	62.24

Tab. C.3.: Gibbs free energy of all intermediates and transition states along hydrogenation pathway leading to decane in gas and DMF/dodecane solvent mixtures using (BPP)HRh-CO catalyst. All energies are in kJ/mol relative to catalyst resting state 1*. The free energy of solvation were calculated using implicit solvent model COSMO-RS.

Methanol/dodecane Composition	Gas phase	(100/0)	(70/30)	(50/50)	(30/70)	(0/100)
1*	0	0	0	0	0	0
1	84.22	83.66	83.69	84.13	84.78	85.28
2	38.65	51.03	52.08	51.72	51.32	51.00
TS 2→3n	83.86	93.84	95.57	95.49	95.55	95.68
3n	52.10	61.43	61.57	60.91	60.29	59.82
4n-hg	89.28	93.84	93.27	92.08	90.86	90.06
5n-hg	76.80	78.96	78.72	78.012	77.41	77.04
TS 5n-hg→decane	115.51	119.36	119.13	118.31	117.55	117.08
decane	-19.84	-21.11	-22.41	-22.72	-22.97	-23.07

Tab. C.4.: Gibbs free energy of all intermediates and transition states along hydroformylation pathway leading to n-Undecanal with (SX)HRh-CO catalyst in gas and DMF/dodecane solvent mixtures. All energies are in kJ/mol relative to catalyst resting state 7-CO. The free energy of solvation were calculated using implicit solvent model COSMO-RS.

Methanol/dodecane Composition	Gas phase	(0/100)	(20/80)	(40/60)	(60/40)	(80/20)	(100/0)
1*	0.0	0.0	0.0	0.0	0.0	0.0	0.0
1	101.4	105.5	105.6	105.3	104.9	104.6	104.6
2	54.6	62.0	62.8	63.0	63.1	63.2	63.4
TS 2→3n	94.2	105.8	107.7	107.7	107.6	107.3	106.5
3n	74.4	82.2	84.0	84.1	84.2	84.2	83.9
4n	6.1	8.2	8.7	9.2	9.6	9.9	10.0
TS 4n→5n	48.3	50.8	51.7	51.6	51.4	50.8	48.9
5n	31.9	31.0	30.6	30.4	30.2	29.8	28.5
6n	31.9	31.0	30.6	30.4	30.2	29.8	28.5
7n	34.8	34.4	26.0	25.0	24.2	22.9	18.4
TS 7n→Undecanal	76.2	70.6	68.8	68.5	68.2	67.8	66.0
Undecanal	18.9	7.2	6.5	6.2	5.8	5.4	4.3

Tab. C.5.: Gibbs free energy of all intermediates and transition states along hydroformylation pathway leading to branched-aldehyde and 2-decene (isomer) with (SX)HRh-CO catalyst in gas and DMF/dodecane solvent mixtures. All energies are in kJ/mol relative to catalyst resting state 1*. The free energy of solvation were calculated using implicit solvent model COSMO-RS.

Methanol/dodecane Composition	Gas phase	(0/100)	(20/80)	(40/60)	(60/40)	(80/20)	(100/0)
1*	0.0	0.0	0.0	0.0	0.0	0.0	0.0
1	101.4	105.5	105.3	105.6	104.9	104.6	104.6
2	54.6	62.0	63.0	62.8	63.1	63.2	63.4
TS 2-3n	106.8	114.9	116.7	116.7	116.7	116.5	116.2
3b	78.6	85.8	87.0	87.2	86.8	86.3	85.3
3iso	97.9	109.0	110.5	110.7	110.2	109.5	107.8
TS 3iso-2iso	102.8	113.4	117.1	117.2	116.9	116.3	115.0
2iso	61.7	71.1	71.9	71.7	72.1	72.2	72.1
2-decene	90.7	94.2	93.9	94.3	93.6	93.2	93.2

Tab. C.6.: Gibbs free energy of all intermediates and transition states along hydrogenation pathway leading to decane with (SX)HRh-CO catalyst in gas and DMF/dodecane solvent mixtures. All energies are in kJ/mol relative to catalyst resting state 1*. The free energy of solvation were calculated using implicit solvent model COSMO-RS.

Methanol/dodecane Composition	Gas phase	(0/100)	(20/80)	(40/60)	(60/40)	(80/20)	(100/0)
1*	0.0	0.0	0.0	0.0	0.0	0.0	0.0
1	101.4	105.5	105.6	105.3	104.9	104.6	104.6
2	54.6	62.0	62.8	63.0	63.1	63.2	63.4
TS 2-3n	94.2	105.8	107.7	107.7	107.6	107.3	106.5
3n	74.4	82.2	84.0	84.1	84.2	84.2	83.9
5n-hg	60.3	61.2	61.2	61.5	61.8	62.1	62.3
TS 5n-hg-decane	108.0	109.4	110.5	110.8	111.2	111.5	111.7
decane	-2.7	-2.8	-2.2	-2.0	-1.7	-1.2	0.1

Tab. C.7.: Relative Gibbs free energy of all intermediates and transition states formed during reductive amination leading to N,N diethylundecylamine in gas and dodecane:methanol solvent mixtures. All energies are in kJ/mol relative to previous intermediates. The free energy of solvation were calculated using implicit solvent models COSMO and COSMO-RS.

		COSMO			COSMO-RS		
	No implicit solvent	Dod:meth (100:0)	Dod:meth (50:50)	Dod:meth (1:99)	Dod:meth (100:0)	Dod:meth (50:50)	Dod:meth (1:99)
$1_3 \rightarrow 2_3$	5.55	14.18	27.11	28.57	9.54	26.24	26.31
TS $2_3 \rightarrow 3_3$	16.41	18.52	22.27	22.76	16.95	19.23	19.73
$2_3 \rightarrow 3_3$	-12.61	-7.05	3.36	4.76	-12.24	-8.61	-4.59
$3_3 \rightarrow 3$âĂŹâĂŹ$_3$	13.81	9.64	2.67	1.81	13.47	11.54	9.05
TS 3âĂŹâĂŹ$_3 \rightarrow 4_3$	46.84	46.06	45.07	44.98	47.25	46.98	45.28
3âĂŹâĂŹ$_3 \rightarrow 4_3$	37.44	39.05	41.69	42.00	36.09	34.06	32.16
TS $4_3 \rightarrow 5_3$	14.94	14.97	15.44	15.55	17.79	20.11	23.03
$3_3 \rightarrow 3$âĂŹ$_3$	1.41	-1.14	-5.48	-6.02	2.04	-2.59	-5.36
TS 3âĂŹ$_3 \rightarrow 5_3$	77.34	72.73	64.65	63.63	76.10	75.0	72.37
$4_3 \rightarrow 5$	-73.13	-102.12	-148.00	-153.39	-30.28	-105.40	-111.94
$6 \rightarrow 7$	14.87	7.55	-5.06	-6.71	12.57	2.89	1.92
$5 \rightarrow 8$	-49.942	-40.37	-22.59	-20.16	-32.90	-31.87	-29.89
TS $8 \rightarrow 9$	23.77	22.97	22.06	21.99	25.60	25.58	25.67
$8 \rightarrow 9$	10.01	9.43	9.08	6.48	13.72	14.60	15.72
$9 \rightarrow 10$	33.87	35.28	37.35	37.60	28.16	29.73	30.14
$10 \rightarrow 11$	-19.71	-23.23	-33.12	-32.25	-23.10	-26.43	-27.07
TS 11→Amine Ax.	49.17	49.75	50.33	50.30	51.43	45.21	43.41
TS 11→Amine Eq.	39.54	41.83	47.98	49.05	44.93	47.12	46.07
11→Amine	-37.42	-43.06	-50.63	-51.40	-52.42	-54.84	-53.62
5→8-rot	-63.16	-56.10	-44.36	-42.93	-47.90	-46.40	-46.05
TS 8-rot→9-rot	17.363	18.38	21.97	22.64	17.34	17.75	19.09
8-rot→9-rot	10.06	11.07	14.74	15.61	10.73	10.76	11.69
9-rot→10-rot	28.32	29.20	30.38	30.34	23.43	24.69	26.32
10-rot→11-rot	-14.34	-17.56	-27.04	-28.67	-16.81	-19.10	-20.77
TS 11-rot→Amine Ax.	55.83	55.54	55.27	55.16	55.94	55.64	56.69
TS 11-rot→Amine Eq.	57.18	59.05	64.72	65.64	57.70	60.34	61.35
11-rot→Amine	-24.08	-28.56	-33.63	-34.08	-35.99	-38.75	-35.91
7âĂŹ→7	6.89	9.44	13.45	13.89	7.54	8.67	9.22

Tab. C.8.: Gibbs free energy of all intermediates and transition states along hydrogenation pathway leading to amine with (SX)HRh-CO catalyst in gas and DMF/dodecane solvent mixtures. All energies are in kJ/mol relative to catalyst resting state 7-CO. The free energy of solvation were calculated using implicit solvent model COSMO-RS.

Methanol/dodecane Composition	Gas phase	(0/100)	(20/80)	(40/60)	(60/40)	(80/20)	(100/0)
7-CO	0.0	0.0	0.0	0.0	0.0	0.0	0.0
8-CO	-26.8	-13.5	-11.7	-11.0	-10.4	-10.1	-10.7
TS8$\rightarrow 9_{\alpha}$	19.0	35.1	38.0	38.3	38.5	38.2	36.5
9_{α}-CO	-12.3	4.3	6.5	6.8	6.8	6.3	3.8
10_{α}-CO	56.0	64.3	65.8	66.8	67.7	68.3	67.4
11_{α}-CO	-6.5	6.7	7.6	8.7	9.6	10.3	9.5
TS 11_{α}-CO $H_{ax}\rightarrow$ 7-CO	70.1	84.3	87.0	87.9	88.7	89.2	87.9
TS 11_{α}-CO $H_{eq}\rightarrow$ 7-CO	31.1	46.1	47.8	48.8	49.8	50.6	50.0
TS8$\rightarrow 9_{\beta}$	15.0	27.1	30.1	30.4	30.4	29.8	27.6
9_{β}-CO	9.8	24.6	26.8	27.1	27.2	26.8	24.7
10_{β}-CO	51.4	58.1	60.7	61.7	62.7	63.4	63.2
11_{β}-CO	10.8	21.4	21.7	22.7	23.6	24.4	24.5
TS 11_{β}-CO $H_{eq}\rightarrow$ 7-CO	35.0	44.4	45.8	46.9	48.0	49.0	49.6
TS 11_{β}-CO $H_{ax}\rightarrow$ 7-CO	48.8	58.3	59.4	60.2	61.0	61.5	61.0
Product	-61.3	-64.7	-65.2	-65.1	-64.6	-63.8	-62.9

Publications

In this thesis

1. Gerlach M., **Jameel F.**, Stein M., Seidel-Morgensten A. and Hamel C., Operando Characterization of Rhodium Catalyst Degradation in Hydroformylation., *Cat. Sci. & Technol.*, **2023**, 13, 1788-1801.

2. **Jameel F.**, Stein M., The Many Roles of Solvent in Homogeneous Catalysis-The Reductive Amination Showcase., *J. Catal.*, **2022**, 405, 24-34.

3. Gerlach, M., Kirschtowski, S., **Jameel, F.**, Huxoll, F., Stein, M., Sadowski, G., Seidel-Morgenstern, A. & Hamel, C. Kinetic Modeling of Complex Catalytic Reactions in Multi-phase Systems. In Kraume, M., Enders, S., Drews, A., Schomäcker, R., Engell, S. & Sundmacher, K. (Ed.), Integrated Chemical Processes in Liquid Multiphase Systems. From Chemical Reaction to Process Design and Operation: De Gruyter. **2022**, 101-149.

4. **Jameel F.**; Huxoll, F.; Stein, M.; Sadowski, G., Solvent Selection for Reactions in Liquid Phases. In Kraume, M., Enders, S., Drews, A., Schomäcker, R., Engell, S. & Sundmacher, K. (Ed.), Integrated Chemical Processes in Liquid Multiphase Systems. From Chemical Reaction to Process Design and Operation: De Gruyter. **2022**, 523-535.

5. Kirschtowski S., **Jameel F.**, Stein M., Seidel-Morgenstern A., and Hamel C., Kinetics of the Reductive Amination of 1-undecanal in Thermomorphic Multi-component System., *Chem. Engg. Sci.*, **2021**, 230, 116187.

6. Huxoll, F., **Jameel, F.**, Bianga, J., Seidensticker, T., Stein, M., Sadowski, G., and Vogt, D., Solvent Selection in Homogeneous Catalysis-Optimization of Kinetics and Reaction Performance. *ACS Catal.* **2021**, 11, 590-594.

7. **Jameel F.**, Stein M., Solvent Effects in Hydroformylation of Long-chain Olefins., *Mol. Catal.*, **2021**, 503, 111429.

Additional Works

1. **Jameel F.**, Kirschtowski S., Hamel C., and Stein M., Ligand and Reactant Gas Control of Rhodium Catalyzed Tandem Hydroaminomethylation of Long Chain Olefins., **(In Preparation)**.

2. Raabe J. C., **Jameel F.**, Stein M., Albert J., and Poller M. J., Hetero Elements in Polyoxometalates: a Study on the Influence of Different Group 15 Elements on Polyoxometalate Formation., **(In Preparation)**.

3. Raabe J. C., Esser T., **Jameel F.**, Stein M., Albert J., and Poller M. J., Study on the Incorporation of Various Elements into the Keggin Lacunary-type Phosphomolybdate $[PMo_9O_{34}]^{-9}$ and Subsequent Purification of the Polyoxometalates by Nanofiltration., *Inorg. Chem. Front.*, **2023**, 10 4854-4868.

4. **Jameel F.**, Kohls E., and Stein M., Mechanism and Control of the Palladium-Catalyzed Alkoxycarbonylation of Oleochemicals from Sustainable Sources., *ChemCatChem*, **2019**, 11, 4894-4906.

5. **Jameel F.**, Boz E., and Stein M., Systematic Quantum Chemical Ligand-Receptor Pose Refinement - Towards Chemical Accuracy., **(In Preparation)**.

Supervised Master Thesis

- **TEEUWEN P.**, Zr-MOCs for electrochemical CO_2 reduction Zirconium metal-organic cages decorated with a $Re(bipy)(CO)_3Cl$ catalyst and the influence of the supramolecular framework on electrochemical CO_2 reduction using a combined experimental and theoretical approach. **2022**, University of Amsterdam.